UNIVERSITÀ
DEGLI STUDI
DI PADOVA

Head Office: Università degli Studi di Padova

Department of Chemical Sciences

Ph.D. COURSE IN MOLECULAR SCIENCES

CURRICULUM PHARMACEUTICAL SCIENCES

XXX SERIES

PHARMACEUTICAL DEVELOPMENT OF THE ISOL TECHNIQUE FOR THE PRODUCTION OF RADIONUCLIDES AND THEIR APPLICATIONS IN TARGETED RADIONUCLIDE THERAPY

Coordinator: Ch.mo Prof. Leonard Prins

Supervisor: Ch.mo Prof. Nicola Realdon

Co-Supervisor: Dr. Alberto Andrighetto

Ph.D. student: Francesca Borgna

To my family

Contents

Abstract

Radiopharmaceuticals are the fundamental tool for nuclear medicine procedures, enabling imaging and therapy of cancer after administration of a radioligand. Imaging or therapy are performed with radionuclides that are bound to a ligand, which selectively accumulates into cancer tissues. The discovery of new radionuclides on one side and the optimization of ligands on the other are fundamental parts of the research in the radiopharmaceutical field.

In the first part of this thesis work we aimed at the development of a new technique for the production of pure radionuclides. The study was born from the collaboration between the Department of Pharmaceutical and Pharmacological Sciences (DSF) of the University of Padua (UniPD) and the Legnaro National Laboratories (LNL) of the National Institute for Nuclear Physics (INFN), where the Selective Production of Exotic Species (SPES) project is under development. This project aims at the production of Radioactive Ion Beams (RIBs) by means of the Isotope Separation On-Line technique (ISOL), which can be exploited for radionuclides production. Thanks to mass separation, a feature of the ISOL technique, radionuclides can be produced at high purity because isotopic contaminants can be cleared away easily. Suitable secondary targets (chapter 2) were developed to allow ion beams collection, depending on the accelerated ions. To verify the suitability of the method for radionuclides production, tests with accelerated stable ion beams were carried out and are described in chapter 3. The SPES test bench was used for the elements ionization and acceleration. The beams were collected on the produced secondary targets and quantified. The tests were carried out for yttrium, iodine and copper, elements interesting for the production of ^{90}Y, $^{125/127/131}$I and $^{64/67}$Cu. The ISOL method guarantees the purification of the radionuclides from the isotopic contaminants, but isobaric and pseudo-isobaric contaminants can be present in the beam and thus in the final solution. For this reason, chemical purification methods have to be developed for radionuclides purification. In chapter 4 the synthesis of an inorganic material (sodium nonatitanate) and its use for strontium and yttrium purification is described.

The second part of this thesis, chapters 5 and 6, was developed in collaboration with the group of PD Dr. Cristina Müller at the Center for Radiopharmaceutical Sciences (CRS) of Paul Scherrer Institute (PSI).

Targeted radionuclide therapy (TRT) represents one of the most promising therapeutic strategies for cancer therapy ; it is based on the use of energetic particles (α, β^- or Auger electrons) selectively delivered in proximity of tumors thanks to specific biologic features. Small molecules are an attractive strategy for active targeted delivery because they are amenable for chemical synthesis and have some advantages if compared with high molecular weight vehicles, such as antibodies.

A potential challenge of small molecular radiotherapeutics is their fast elimination from the body preventing sufficient accumulation of radioactivity in the malignancies due to glomerular filtration and fast renal clearance; high accumulation of radioactivity in the kidneys increases at the same time the risk of nephrotoxicity. For this reason, new strategies to allow a higher translation from preclinical to clinical phase of small molecule-based radiopharmaceuticals should be developed.

In this thesis project two strategies to improve TRT with small molecules were developed. The first relies on the development of radioligands with a serum protein-binding domain. This strategy is based on the consideration that serum proteins have high molecular weight, and for this reason do not undergo glomerular filtration (filtration cut-off 30-50 kDa). In particular, three serum proteins-binding compounds were radiolabeled and characterized *in vitro* and *in vivo* (chapter 5).

Another strategy to improve TRT efficacy while decreasing side effects is the use of combined-modality regimens. This approach is very popular in cancer therapy since targeting the cancer cell on diverse molecular path mechanisms makes the cell less prone to developing resistance to the therapy. At the same time, the use of multimodality therapies allows to decrease the dosage of single therapies, thus reducing side-effects. In the last chapter of this thesis (chapter 6) a preliminary study combining radionuclide therapy (^{177}Lu-cm10) with two tyrosine kinases inhibitors is described, based on the assumptions of a possible synergistic effect of the two agents.

Riassunto

I radiofarmaci rappresentano uno strumento fondamentale per la medicina nucleare, rendendo possibile, grazie alla somministrazione di un radioligando, procedure diagnostiche e terapeutiche in ambito oncologico. I radiofarmaci sono costituiti da un radionuclide e da un ligando; quest'ultimo permette la localizzazione della radioattività solamente nei tessuti bersaglio. La ricerca in ambito radiofarmaceutico è dedicata sia alla scoperta di nuovi radionuclidi, sia all'ottimizzazione dei ligandi.

Scopo della prima parte di questo lavoro di tesi è stato lo studio e lo sviluppo di una tecnica innovativa per la produzione di radionuclidi ad alta purezza per la medicina nucleare. Lo studio è nato dalla collaborazione presente tra il Dipartimento di Scienze del Farmaco (DSF) dell'Università di Padova (UniPD) e i Laboratori Nazionali di Legnaro (LNL) dell'Istituto Nazionale di Fisica Nucleare (INFN). Presso questi ultimi, infatti, è in fase di costruzione il progetto *Selective Production of Exotic Species* (SPES), che prevede la produzione di fasci di ioni radioattivi (RIBs), prodotti tramite la tecnologia *Isotope Separation On Line* (ISOL). La separazione in massa prevista dalla tecnica ISOL, la rende un'ottima via di produzione di radionuclidi, perché permette di eliminare tutti i contaminanti isotopici del radionuclide d'interesse.

Per la deposizione dei fasci sono stati sviluppati e costruiti dei bersagli secondari; questi oggetti, posizionati alla fine della linea di fascio, sono utilizzati per depositare e recuperare gli ioni accelerati. La progettazione e realizzazione di tali bersagli è descritta nel capitolo 2. In seguito, con lo scopo di verificare la possibilità di utilizzare l'apparato sperimentale di SPES per la produzione di radionuclidi per la medicina nucleare, sono stati condotti dei test utilizzando fasci di ioni stabili degli elementi di interesse, in particolare sono stati studiati fasci di ittrio, iodio e rame, ai fini della produzione futura di ^{90}Y, $^{125/127/131}$I e $^{64/67}$Cu.

Il metodo ISOL consente grazie alla separazione in massa di purificare i radionuclidi dai contaminanti isotopici, ma contaminanti isobarici e pseudo-isobarici devono essere rimossi tramite altri metodi, in particolare tramite metodi chimici. Per questo motivo nel capitolo 4 vengono descritti la sintesi e l'uso di una resina inorganica a scambio ionico per la purificazione di ittrio e stronzio.

La seconda parte di questa tesi è stata sviluppata in collaborazione con il *Center forRadiopharmaceutcal Sciences* (CRS) presso il Paul Scherrer Institute (PSI), Villigen (CH), in particolare nel gruppo della Dott.ssa PD Cristina Müller.

La *targeted radionuclide therapy* (TRT) è un strategia terapeutica molto promettente in campo oncologico e si basa sull'uso radionuclidi che emottono particelle ad energia medio-alta (α, β^- o elettroni di Auger) che vengono selettivamente direzionati nel tessuto canceroso in seguito al riconoscimento di una particolare caratteristica della cellula tumorale. L'utilizzo di piccole molecole per il direzionamento dei radionuclidi rappresenta una strategia vantaggiosa rispetto all'uso di veicoli ad alto peso molecolare (come gli anticorpi monoclonali) ed inoltre possono essere prodotte tramite sintesi chimica. Tuttavia, nonostante il successo di alcune *small molecules* in clinica, molte volte questa tipologia di radiofarmaci va incontro ad una veloce eliminazione ematica a causa della loro filtrazione glomerulare. In questo modo l'acccumulo della radioattivià nel tumore è diminuito, mentre può esserci un accumulo indesiderato nei reni con aumentato rischio di nefrotossicità.

In questa tesi vengono descritte due strategie per il miglioramento della TRT basata sull'uso di piccole molecole. La prima prevede la modifica della struttura chimica dei ligandi con un dominio di legame alle proteine plasmatiche. Questa strategia permette, infatti, di evitare la filtrazione glomerulare del radioligando. Questo, se dopo la somministrazione si lega in modo reversibile ad una proteina plasmatica, viene ad assumere un peso molecolare >30 kDa, valore del *cut-off* della filtrazione nel glomerulo ed aumenta per questo motivo la sua emivita plasmatica. Nel capitolo 5 vengono descritte la radiomarcatura e la caratterizzazione *in vitro* ed *in vivo* di tre radioligandi con affinità per le proteine plasmatiche.

La seconda strategia è quella dello sviluppo di terapie combinate con altri agenti chemioterapeutici. Questo approccio è molto popolare in quanto permette da una parte di ridurre le dosi dei singoli agenti e ridurre così gli effetti collaterali, dall'altra di ridurre la resistenza alla terapia. Nel capitolo 6 della tesi, è descritto lo studio preliminare dell'associazione di un radioligando per la terapia (^{177}Lu-cm10) con due inibitori tirosin chinasici.

Chapter 1

Production of radionuclides and challenges of targeted radionuclide therapy

1.1 Introduction

Nuclear medicine is a fundamental branch of medicine for tumor diagnosis and therapy. Its development in the 20th century was due to and boosted by the discovery of radioactivity and the possibility of producing radionuclides suitable for human administration. Radiopharmaceuticals are the essential tool for nuclear medicine procedures, enabling imaging and therapy of disseminated diseases after administration of a radioligand. Imaging or diagnostic radionuclides are bound to a ligand, which selectively accumulates into a target tissue. The discovery of new radionuclides on one side and of new ligands on the other are pivotal parts of the research in the radiopharmaceutical field.

The ISOLPHARM project aims to study a new and unconventional technique for the production of pure radionuclides for nuclear medicine, exploiting the Radioactive Ion Beams (RIBs) produced in the framework of the SPES (Selective Production of Exotic Species) project at the Legnaro National Laboratories (LNL) of the National Institute for Nuclear Physics (INFN) [1.1,1.2].

At SPES, RIBs are produced by means of the Isotope Separation On-Line (ISOL) technique. Briefly, the ISOL method guarantees the ionization of radioisotopes, produced inside a primary target, that are afterwards accelerated and, thanks to mass separation, purified to produce an isobaric beam [1.3]. Isobaric beams which contain a radionuclide useful for nuclear medicine, can be exploited for the production of radiopharmaceutical precursors [1.4,1.5]. This should be regarded as particularly relevant because with mass separation all isotopic contaminants are easily and inexpensively cleared away from the final product and carrier-free radionuclides can be produced [1.6].

Radionuclides at a "carrier-free quality" are tremendously researched as radiopharmaceuticals precursors. This is due to the fact that during the last decades a big part of the research in radiopharmacy has been dedicated to the development of new receptor targeting radiometal labeled pharmaceuticals [1.7]. These radiopharmaceuticals are made of a biomolecule and a radiometal. The biomolecule can also be called vector, because, thanks to the molecular recognition with a protein that is overexpressed on the surface of cancer cells, it allows the accumulation of the radiation in the target tissue. Since the binding is easily saturable it is necessary that no cold compound dilute the radiopharmaceutical. If carrier-free radionuclides are used for the radiolabeling the accumulation to target organs is optimized [1.6,1.8].

The number of radionuclides produced with the ISOL technique at LNL that can be considered as promising radiopharmaceutical precursors is huge. Depending on the primary target and, consequently on the induced nuclear reaction, different radioactive species can be originated: radionuclides already used in the clinics as ^{89}Sr, $^{125/131}$I, ^{90}Y, and ^{177}Lu, but also innovative radionuclides, as ^{111}Ag, $^{43/44/47}$Sc, $^{64/67}$Cu and $^{152/155}$Tb.

The ISOLPHARM project is outlined as a multidisciplinary study where many competences are involved. Nuclear physics studies on the expected nuclear reactions, materials engineering development of the desired production targets and mechanical implementation of the accelerator for the RIBs production. Afterwards chemical and pharmaceutical development of the secondary target to collect the accelerated ions and their chemical purification from isobaric contaminants. Finally, pharmaceutical studies for the radiolabeling of biological vectors for the production of a radiopharmaceutical.

Together with the radionuclides production development, the optimization of the ligands characteristics to improve the diagnostic and therapeutic features is fundamental. Receptor-affinity, cell internalization, pharmacokinetic properties and minimization of side effects are part of the development of a radiopharmaceutical.

In this thesis the potential use of the ISOL facility under construction at LNL for the production of radionuclides was tested: the secondary targets for the ions deposition were developed (chapter 2), the RIBs of the desired element were produced in off-line modality, i.e. with stable isotopes (chapter 3), a new material for the chemical purification of Sr/Y was developed and tested (chapter 4). Moreover, a study for the optimization of the ligand properties was carried out at the Center for Radiopharmaceutical Sciences (CRS) of Paul Scherrer Institute (PSI). In particular,

three serum proteins-binding compounds were radiolabeled and characterized *in vitro* and *in vivo* (chapter 5). Finally, a preliminary study for the combination therapy of tyrosine kinases inhibitors with targeted radionuclide therapy in folate receptor positive cancer cell lines was carried out (chapter 6).

In this chapter the main conventional routes for radionuclides' production and the principles and challenges of targeted radionuclide therapy are described. Finally, the SPES project and the ISOL method for RIBs production are described into detail.

1.2 Conventional production routes for radionuclides [1.6]

The production of radioisotopes, which are the radioactive "core" of radiopharmaceuticals, is a very crucial step. In this paragraph the main production routes are described to allow a comparison with the new production method proposed within the ISOLPHARM project.

When considering the production of radionuclides for nuclear medicine, not only the producible amount should be considered. Two additional properties have to be kept in mind: the specific activity and the radionuclidic purity.

The specific activity of a radioisotope is the ratio between the activity of the radioisotope (MBq) and the mass of the element (mg). This is an important concept because often, due to the production methods, the radionuclide is diluted by mixtures of other "cold" isotopes of the same element, which do not exert any effect. Radioisotopes with high specific activities are required for radiolabeling of ligands that target tumor markers on cells (like receptors), which are easily saturable. Radioisotopes which are pure are called "carrier-free", differently from those diluted by cold mixtures of the same element, which are defined as "carrier-added".

The second feature that has to be considered is radioisotopic (defined also as radionuclidic) purity. This other property measures the presence of unwanted radioisotopes.

The main reactions used for radioisotopes production are neutron capture and proton induced reactions. Generators can be considered as a third way for radioisotopes production, particularly used and advantageous for short-lived isotopes.

1.2.1 Neutron capture [1.6]

Nuclear reactors are the main facilities used for this kind of reactions, which are normally used to produce β^--emitting radionuclides. Stable targets are irradiated with neutrons and neutron-rich isotopes, close to the stability valley, are produced.

The specific activity (S) of the produced radionuclides, if we consider a one-step transmutation reaction, is given by equation 1.1:

$$S = \frac{N_A}{A} \cdot \sigma \cdot \varphi \cdot \left(1 - \exp\left(-\frac{\ln(2) \cdot t_{irr}}{T_{1/2}}\right)\right) \quad (1.1),$$

where N_A is the Avogadro constant, A is the atomic mass, σ is the reaction cross-section, φ is the neutron flux density and t_{irr} is the irradiation time. Thus it is evident that to have high specific activities values, high neutron flux (φ) and high cross sections (σ) are essential. This way a high fraction of the stable target is converted into the desired radioisotope. Few radionuclides are produced with appreciable levels of specific activities with this reaction (^{60}Co, ^{153}Sm, ^{169}Yb, and ^{177}Lu). Although the target enrichment[1] can be a strategy to improve specific activity, this method is very expensive and complex, causing an increase in the production costs.

Carrier-free radionuclides can be produced by neutron capture reactions if the radioisotope produced with this reaction is the "mother" of the wanted radioisotope. This way the desired radioisotope is chemically different from the target material and can be more easily purified. If the "mother" isotope is short-lived, then a single purification step is performed because it quickly decays. If the intermediate isotope is longer-lived, then a generator is produced. Generators will be described in 1.2.3.

1.2.2 Accelerator-based

The most diffused accelerators used for nuclear medicine are cyclotrons, essential tools for nuclear medicine isotopes production, in particular imaging ones (PET and SPECT). The most common reactions are proton-induced and depend on the projectile energy. ~5-15 MeV cyclotrons are used to induce (p,n) and (p,α) for most common PET-radionuclides production; higher protons energies are required for (p,2n) and (p,4n), 30 and 70 MeV, respectively. Very high protons energies (GeV) can induce spallation,

[1] Increasing the amount of the isotope necessary for the nuclear reaction

inducing this way the production of radioisotopes far from the elements of the target material.

1.2.3 Generator-based

Generators are efficient solutions to match the need of short-living radioisotopes for imaging with the logistic. They are loaded with a long-lived radionuclide, called "mother", that decays to the daughter radionuclide, which is eluted just before the use. A successful example is the $^{99}Mo/^{99m}Tc$ generator, which enabled the use of ^{99m}Tc, probably the most successful SPECT radioisotope.

The only disadvantage of generators is that the mother nuclide is often a more exotic radionuclide, whose production could require more efforts.

1.3 Targeted radionuclide therapy (TRT)

According to the World Health Organization, cancer is the second leading cause of death worldwide, with 8.2 million cases every year and an estimated incidence of 14.1 million new cases every year. The development of improved diagnostic and therapeutic strategies for the management of cancer is, therefore, urgently needed. Targeted radionuclide therapy (TRT) represents one of the most promising therapeutic strategies [1.9]; it is based on the use of energetic particles (α, β^- or Auger electrons) selectively delivered in proximity of tumors thanks to specific biologic features. Ideally TRT delivers a high amount of radioacitivty to cancer cells, sparing healthy tissues (see Figure 1.1).

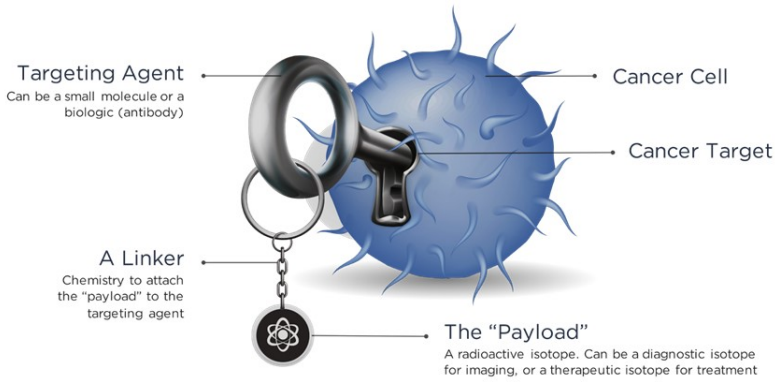

Figure 1.1. Scheme of Targeted Radionuclides Therapy. The molecule is made of a targeting agent that recognizes a molecular target overexpressed on cancer cells, a linker and a radionuclide with suitable decay properties. Picture taken from: http://www.telixpharma.com/theranostics/ , last access 26th Otboter 2017, 11.45.

Moreover, TRT can be used when external radiation can not be used, like in systemic malignancies, and the treatments are usually shorter than chemotherapy [1.9]. The first example of TRT dates back to 75 years ago, when radioiodine was used for thyroid disorders including cancer. After that many other examples of successful terapies followed, such as the treatment of painful bone metasteses with the β^--emitting ^{89}Sr and ^{153}Sm, and more recently with the α-emitter ^{223}Ra. ^{90}Y found application when conjugated with anti-CD20 monoclonal antibodies for relapsed or refractory low-grade, follicular, or transformed B-cell *non-Hodgkin* lymphoma [1.10]. New approaches are nowadays used in the clinics and in preclinical reasearch thanks to the new challenges introduced with radiotheranostics, that couples imaging of tumor lesions with therapy. In this regard one of the biggest issues is the development of chemically similar or identical radioligands for imaging first and therapy second. Successful examples in this regard are the analogues of somatostatin (e.g. DOTATATE) labeled with either diagnostic radionuclides such as ^{68}Ga (for PET) and ^{111}In (for SPECT) or therapeutic radionuclides including ^{90}Y or ^{177}Lu allowing the management of patients suffering from neuroendocrine tumors [1.11,1.12]. More recently the prostate-specific membrane antigen (PSMA)-targeting ligands (e.g. ^{68}Ga-PSMA-11 and ^{177}Lu-PSMA-617), have been used for clinical studies resulting in clear visualization of prostate cancer lesions via PET and remission in treated patients with metastatic prostate cancer [1.13–1.15].

1.4 Challenges of targeted radionuclide therapy

In targeted radionuclide therapy a radiopharmaceutical is made of two main entities: a targeting ligand, which binds specifically to tumor-associated marker (e.g. receptor) and a payload, which is a therapeutic radiometal [1.16]. In this paragraph we will describe the main challenges related to TRT, talking first about the choice of the radiometal and, second, about the challenges related to the development of an ideal small molecule-based targeting ligand.

14.1. The choice and availability of suitable radionuclides

In TRT the choice of the proper radionuclide plays an important role. Several physical properties should be considered to select suitable radionuclides for therapy. First of all, the nuclear decay properties [1.6]: α- and β^--emitting radionuclides are used in therapy

because high-energy particles are able to induce cell death. Alpha particles are positively charged and have energies ranging from 5 to 9 MeV. Their range of penetration is of ~5 mammalian-cell diameters and their linear energy transfer (LET) is in a very high range: 80-100 keV/μm [1.17]. The recent successful introduction in the clinics of $^{223}RaCl_2$ for the treatment of bone metastases, renewed the interest for α-emitting radionuclides [1.18]. β^- radionuclides emit negatively charged particles that lose their energy while traversing matter following a contorted path. The LET of these radionuclides is ~0.2 keV/μm, which is very low compared to α particles. On the contrary their penetration range in tissues is higher (up to 12 mm), thus also allowing the bombardment of the cells not directly targeted by the radiopharmaceutical, due to the cross-fire effect. Thanks to this phenomenon not all the cells within the tumor require to be targeted. On the other hand, due to the low LET, a high concentration of radionuclides has to be produced in proximity of the tumor [1.17]. ^{90}Y and ^{177}Lu are two successful examples of β^--emitting radionuclides applied in the clinics. The first with β^- particles emission at higher energies and the second with a lower energy and accompanied by γ radiation useful for dosimetry [1.19]. Lately Auger-emitting radionuclides attracted the attention, due to their high therapeutic potential. Auger electrons (namely X ray photons, Coster-Kronig or super Coster-Kronig monoenergetic electrons) are emitted due to the vacancies produced in the shell of atoms (usually in the K shell) after electron capture and/or internal conversion. Vacancies are filled thanks to the transition of electrons from outer to inner shells, resulting in the emission of Auger electrons. Usually ~5-30 Auger electrons are emitted per decaying atom with an energetic range from few eV to 1 keV [1.20]. Auger electrons travel in contorted path with a very short range in water (from few nanometers to ~0.5 μm) and with multiple ionizations in the proximity of the decay site with LET ~4-26 keV/μm [1.21]. Due to their short range, Auger-emitters need to reach the very proximity of cell DNA to induce cell death. ^{161}Tb has very similar characteristics to ^{177}Lu considering the physical half-life and the β^- energy, but coemits a high number of Auger electrons. Its therapeutic effect has been compared to that of ^{177}Lu in two independent preclinical studies and ^{161}Tb proved to be more effective [1.22–1.24].

One more fundamental property for radioisotopes selection is their physical half-life [1.6]. Suitable radionuclides for therapy should range from 6 h to 7 d [1.25]. The half-

life of radionuclides should match clinical indications and logistics [1.19]. Very short living radionuclides, indeed, limits the flexibility of use, due to the impossibility of delivering the radiometal to the nuclear medicine centers. On the other hand, too long-living radionuclides impact in a negative way on the radiation dose to the patients, exposing the surrounding people for a longer period. The half-life should also match the biological half-life of the tracer [1.9].

Furthermore, one should also consider the chemical characteristics of the radiometal. It is necessary, indeed, that the radiometal could be stably bound to the bioconjugate. Radiometals are normally conjugated thanks to a chelator that guarantees thermodynamic and kinetic stability. The aforementioned chelator is most likely a bifunctional chelator (BFC), able to complex the radiometal and possessing a functional group for covalent attachment of the biomolecule [1.7]. The requirements that a BFC has to address are several. First of all, it has to guarantee thermodynamic and kinetic inertness in a pH range of 5-7.5, in order to avoid undesired release of the radiometal after administration, which can accumulate into not targeted tissues. The BFC has to compete with natural chelators present in the blood circulation, like transferrin and albumin for example. To face these requirements acyclic and macrocyclic chelators have been developed. Acyclic chelators are more advantageous for radiolabeling of thermosensitive molecules, such as monoclonal antibodies, because they do not require harsh radiolabeling conditions. On the other hand, their kinetic inertness is lower. Macrocyclic chelators, instead, are usually more stable; if not it means that they do not have the proper denticity for the specific radiometal. In case of this latter kind of chelators high temperatures are required to guarantee high radiolabeling yields. The BFC also has to be radiostable, to avoid the radiolytic effect [1.7].

Last but not least, is the possibility to produce the radionuclides in a large scale and to develop a method that is safe and affordable in order to guarantee supply of the radionuclides for clinical use [1.6,1.19]. Several of the therapeutic radionuclides (^{90}Y, ^{131}I, ^{153}Sm, ^{166}Ho, ^{177}Lu and ^{188}Re) are produced by nuclear reactors, whose role have yet to be completely replaced [1.26,1.27]. Replacement projects should be encouraged in order to be able to provide radionuclides for therapy with alternative routes. The research in the field of radionuclidic production should be developed also in order to produce new radionuclides whose production is not feasible with nuclear reactors or conventional cyclotrons. One example is ^{67}Cu, a very promising radionuclide from the

point of view of its physical characteristics (low energy β^-, coemitted γ ray for SPECT, $t_{1/2}$ 61.9 h) and for the possibility of having a theranostic match with ^{64}Cu [1.28]. Carrier-free ^{67}Cu cannot be produced in sufficient amounts up to now.

1.4.2 Small molecules-based radioligands for TRT

In this subparagraph we describe the challenges related to the use of small molecules as targeting ligands in TRT. Small molecules are an attractive strategy for active targeted delivery because they are amenable for chemical synthesis and have some advantages if compared with high molecular weight vehicles, such as antibodies. Antibodies are limited in their efficacy, mostly due to their inability to reach cells within the tumor mass [1.29]. This is due to the fact that tumor cells are not identical and they can undergo loss of antigen expression [1.30] and to the "antigen barrier" effect, an hypothesis which predicates that the few antibodies molecules able to extravasate and reach the abluminal side of blood vessels are trapped by the antigens located on perivascular tumor cells [1.29]. Furthermore, antibodies can be immunogenic, even if humanized or fully human, leading to hypersensitivity in patients and neutralization of the therapeutic effect [1.31]. In contrast to antibodies, low-molecular-weight compounds can easily diffuse out of blood vessels and afterwards penetrate deeply into tissues. For these reasons, the use of disease-homing small molecules, coupled to cytotoxic payloads, such as radiotherapeutic nuclides, is a good strategy for active targeting of tumors overcoming antibodies problems. Beside their ability of penetrating into tissues, they are also not immunogenic and they are amenable for chemical synthesis. These compounds, after binding to their molecular targets on the cells, e.g. receptors, rapidly undergo mediated endocytosis, resulting in the folding of the ligand-receptor complex into a vesicle, that afterwards fuses with the early endosome, see figure 1.2, carrying the radioactive payload into the cancer cell [1.29].

Successful examples of the use of this strategy in clinics is the use of radiolabeled small peptides, like the somatostatin analog DOTATATE, coupled with ^{68}Ga or ^{111}In for diagnosis (PET and SPECT, respectively) and ^{177}Lu or ^{90}Y for therapy for the management of patients suffering from neuroendocrine tumor [1.11,1.32]. Recently, the use of analogues of the natural substrate of prostate-specific membrane antigen (PSMA), namely ^{68}Ga-PSMA-11 and ^{177}Lu-PSMA-617, have been used for clinical

studies resulting in clear visualization of prostate cancer lesions via PET and remission in treated patients with metastatic prostate cancer [1.14,1.15,1.33].

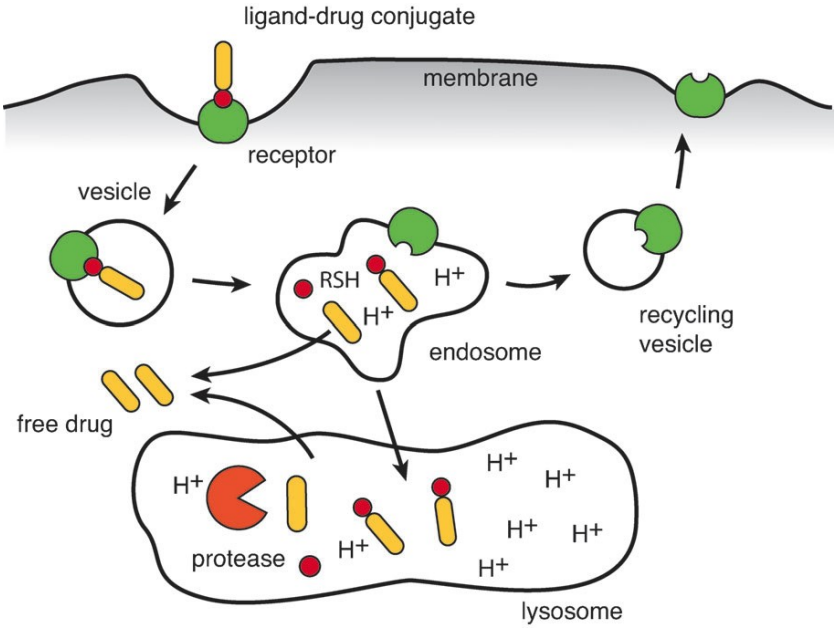

Figure 1.2. Mechanism of radioconjugate internalization after receptor binding [1.29].

The folate receptor (FR) is expressed on a variety of tumor types (e.g. ovarian, endometrial, lung cancer etc.) [1.34], but restricted to only a few sites in normal tissues, the most problematic being the kidneys [1.35]. The vitamin folic acid has been used as a tumor targeting ligand due to the possibility for derivatization and its high affinity to the FR even after conjugation to a diagnostic/therapeutic probe [1.36]. Over the last ten years, a large number of folate radioconjugates has been developed for nuclear imaging and therapy of FR-positive tumors. These compounds were extensively studied preclinically in preclinical in *in vitro* and *in vivo* experiments [1.37].

A potential challenge of small molecular radiotherapeutics is their fast elimination from the body preventing sufficient accumulation of radioactivity in the malignancies due to glomerular filtration and fast renal clearance; high accumulation of radioactivity in the kidneys increases at the same time the risk of nephrotoxicity [1.38,1.39]. This drawback makes the therapy more expensive and riskier for the patients because repeated administration and larger doses are required. For this reason, new strategies to allow a higher translation from preclinical to clinical phase of small molecule-based radiopharmaceuticals should be developed.

1.5 The SPES project and the RIBs production with the ISOL method

The aim of the SPES project [1.40] is to provide high intensity and high-quality beams of neutron-reach nuclei to perform forefront research in nuclear structure, reaction dynamics and interdisciplinary fields like medical, biological and material sciences. It can be considered as composed of four phases (see figure 1.3):

- SPES-α: at the heart of SPES: the cyclotron and ISOL target.

  This phase, now almost completed, foresaw the acquisition, installation and commissioning of a high performance cyclotron with high output current (0.7 mA) and high energy (up to 70 MeV), together with the related infrastructure for the accelerator and experimental stations. The cyclotron is provided with two exit ports, a configuration well suited for the double mission of the laboratory: basic research and technological applications. One of the two beams will be dedicated to the nuclear physics facility (producing mainly neutron-rich ions by collisions of protons onto a UC_x target); the second will be dedicated to applied physics;
- SPES-β: the acceleration of neutron-rich unstable nuclei.

  Neutron-rich species will be accelerated against suitable targets. In the collisions, new, extremely neutron-rich nuclei will be produced, which are similar to those generated in advanced stellar stages and are not present on Earth due to their short lifetime. The investigation on such systems is a new frontier of physics, for extending our knowledge of nuclei at extreme conditions and for providing basic information in the study of stellar evolution;
- SPES-γ: production of radionuclides for applications.

  It concerns the production of radionuclides of medical interest by using the SPES-α cyclotron. The goal is the production of innovative radiopharmaceutical both for ISOLPHARM and LARAMED (LAboratory for the production of RAdioisotopes of MEDical interest) as well as the production of conventional radionuclides with new accelerator-based approaches;
- SPES-δ: multidisciplinary neutron sources.

  It foresees the development of an intense neutron source, from the cyclotron and/or from a high intensity linear accelerator based on radio-frequency quadri

pole (RFQ) technology. Applications of the neutron source range from nuclear astrophysics to test of electronics in space, characterization of nuclear waste or experimental tumor treatments.

Figure 1.3. SPES project logo.

SPES-β, in particular, aims at producing radioactive ion beams of high purity neutron rich nuclei, with mass ranging between 80 and 160 amu [1.1]. The main aim of SPES is to become a user facility for physics researchers who will make use of the produced radioactive ion beams to perform nuclear physics, materials science and astrophysics studies and experiments. The facility layout is outlined in figure 1.4.

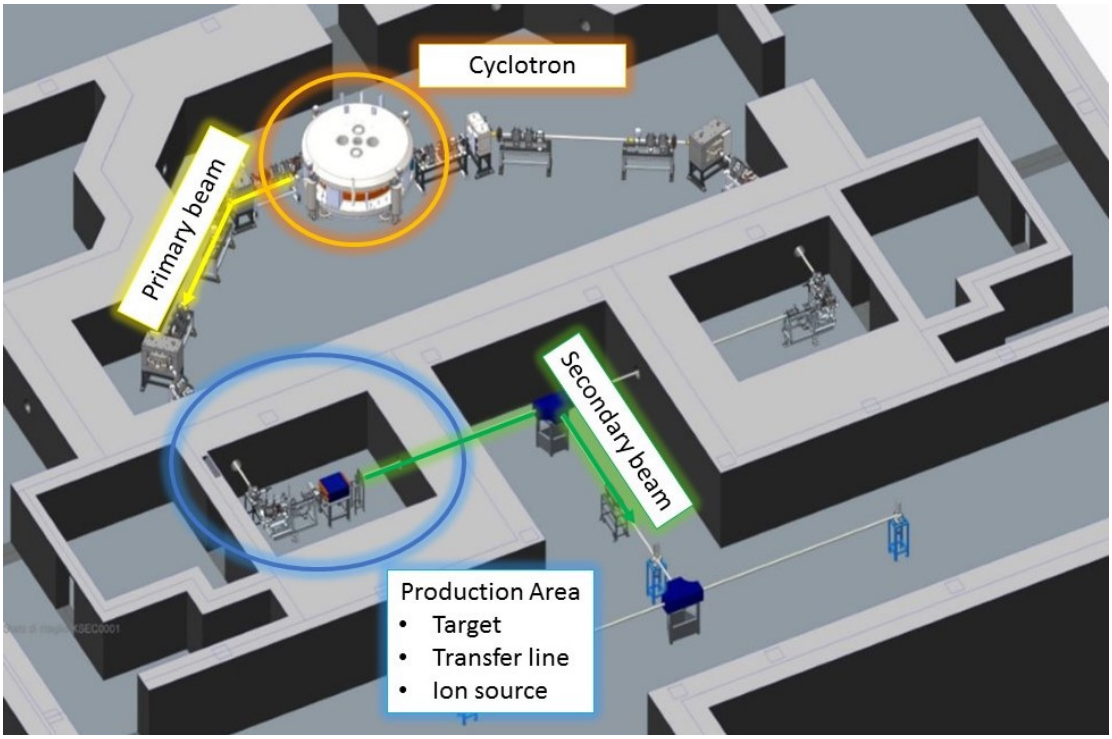

Figure 1.4. SPES facility layout.

Today, the ISOL technique is established as one of the main techniques for the on-line production of high intensity and high quality radioactive ion beams [1.41].

The production of the radioactive isotopes is obtained by nuclear reactions induced by 40 MeV protons, accelerated by a cyclotron, that will collide on a target composed of 7 discs of carbon dispersed uranium carbide (UC_x) [1.3], properly spaced in order to dissipate the heat (8 kW) generated by the reaction. The uranium contained in the target material will be ^{238}U, this ensures that the produced radioactive isotopes will belong to a group of elements having atomic numbers between 28 and 57 (elements placed between nickel and lanthanum in the periodic table). In particular, most of the produced nuclides will be neutron-rich, so we can expect an excess of neutrons with respect to the element stable nuclear configuration. Among the radionuclides produced with UC_x fission, relevant radionuclides already used in nuclear medicine are produced: ^{89}Sr, a radionuclide used for treatment of painful bone metastases secondary to prostate cancer [1.42], ^{90}Y, successfully used in radioimmunotherapy [1.9], and $^{125/131}I$, the first used in brachytherapy in several cancer types, e.g. the localized prostatic cancer, [1.43,1.44], the second used for thyroid diseases [1.45] and in Non-Hodgkin lymphomas [1.9].

Other innovative, not fissile, target materials are under development at LNL for the ISOLPHARM project. Firstly, titanium carbide (TiC), a material which is very promising for the production of scandium isotopes. In figure 1.5 the produced radionuclides foreseen are presented.

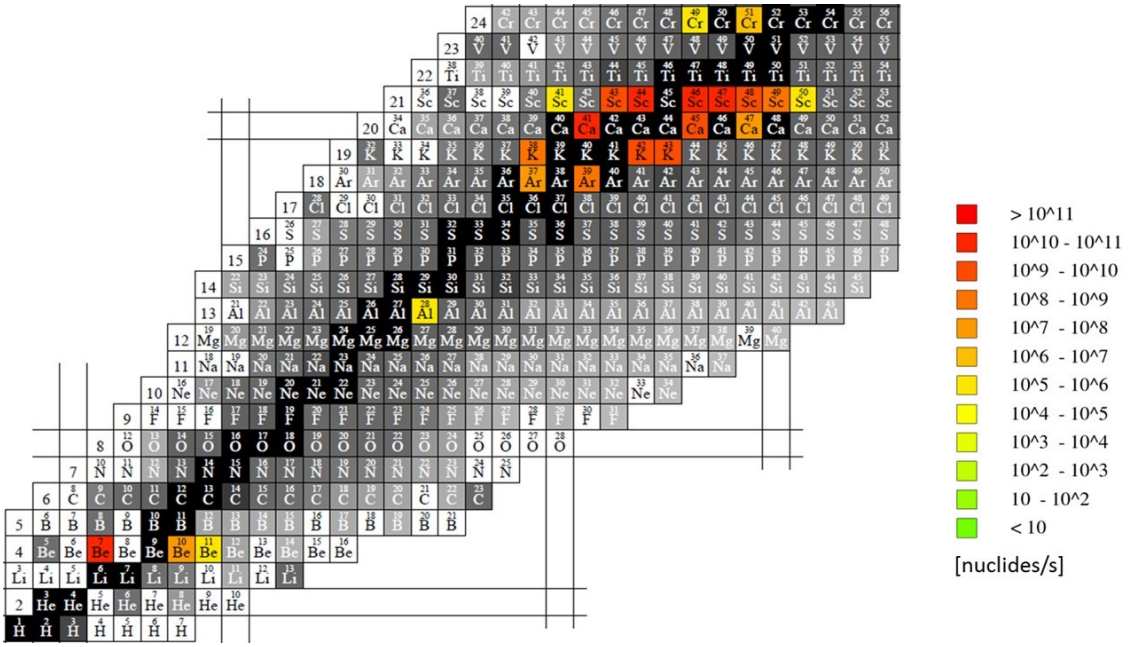

Figure 1.5. Isotopes production from TiC target provided by the FLUKA simulation. Primary proton beam energy= 40 MeV, current= 200 μA, working temperature=2200 °C (Unpublished data).

$^{43/44/47}$Sc can be produced with good yields, and as carrier-free, without the need of target enrichment. The medical potential of these radionuclides was demonstrated [1.46] and for this reason it is worth investigating their production with the ISOL method. Moreover, scandium is an ideal element for radiotheranostics, because $^{43/44}$Sc are PET radionuclides, while ^{47}Sc is a β^- emitter with suitable decay characteristics for therapy [1.19].

Another target material under investigation is zirconium germanide. This target can produce the radioisotopes reported in figure 1.6. Among these, the two radionuclides of mass 64 and 67 of copper are relevant for diagnostic and therapeutic purposes, respectively. They also are a perfect matched pair for radiotheranostics, and ^{67}Cu production is nowadays very limited [1.19].

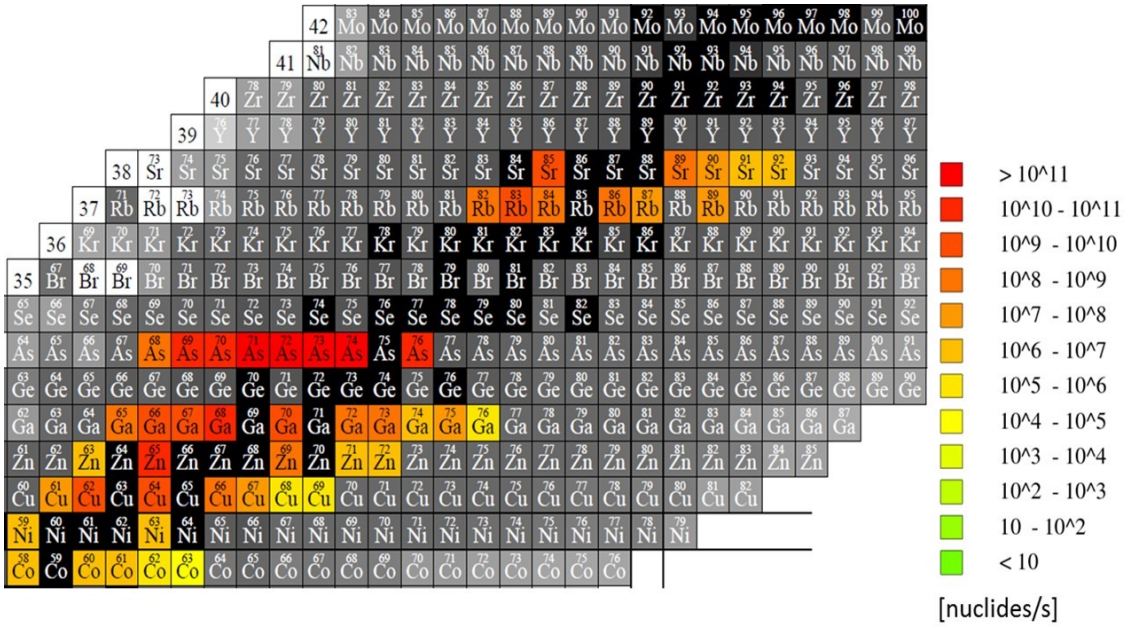

Figure 1.6. Isotopes production from ZrGe target provided by the FLUKA simulation. Primary protonbeam energy= 40 MeV, current= 200 μA, working temperature=2200 °C (Unpublished data).

Independently on the target and on the reaction, the reaction products will be extracted from the target by evaporation at high temperature (about 2000 °C), and then forced to pass through a transfer tube towards an ionization cavity, where they will be ionized to the 1^+ state [1.47–1.50]. Once ionized, these isotopes will be accelerated through an electrode at high potential (up to 40 kV). The formed beam will be subsequently directed and focalized using different electromagnetic systems, and then finally purified (mass separated) in order to have a pure isobaric beam without any isotopic

contaminants. It will therefore be possible to collect the radionuclides of interest using a proper substrate placed at the end of the experimental line, see figure 1.7.

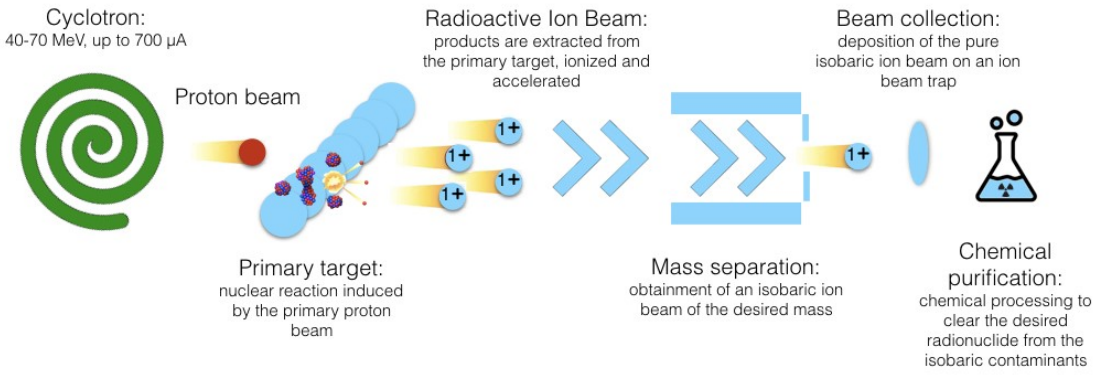

Figure 1.7. ISOLPHARM scheme.

Thanks to mass separation it is therefore possible to produce in a simple and straightforward manner carrier-free radionuclides, ideal for radiolabeling. With the ISOLPHARM project we want, to suggest the ISOL technique as new and unconventional method for radionuclides production with very high purity, to match the necessity of radionuclides, often not available with traditional techniques.

1.6 New strategies in TRT

The use of small molecule-based radioconjugates for therapy is hindered by the very rapid blood clearance of these compounds. Due to their low molecular weight they rapidly undergo glomerular filtration, thus making their biological half-life very short. This scenario prevents a high accumulation of the radioconjugate in the tumor and makes the repeated administration of high quantities of radioactivity necessary. This is not an ideal situation, because side-effects to healthy tissues are increased together with the radionuclides costs. Moreover, the high degree of renal clearance can increase the risk of nephrotoxicity [1.34,1.39]. In this thesis project two strategies to improve TRT with small molecules were developed. The first relies on the development of radioligands with a serum protein-binding domain (chapter 5). This strategy is based on the consideration that serum proteins have high molecular weight, and for this reason do not undergo glomerular filtration (filtration cut-off 30-50 kDa [1.51]). The radioconjugate half-life is in this way increased and its tumor accumulation facilitated.

The development of a folic acid radioconjugate functionalized with an albumin-binding domain enabled the first preclinical therapy study with radiofolate in mice [1.52]. This strategy was also recently used for PSMA inhibitors, to improve the biodistribution and therapeutic efficacy in prostate tumor-bearing mice [1.33].

In both these studies an albumin binder was used to decorate the radioconjugate. The albumin binder was previously developed by Dumelin *et al.*, and is based on a p-iodophenyl group [1.53]. Recently another serum protein, transthyretin, was proposed as a possible transporter to increase biological half-life of peptides. In this study, Penchala *et al.* developed a binding motif for L-thyroxine binding pocket on transthyretin [1.54].

Another strategy to improve TRT efficacy while decreasing side effects [1.55] is the use of combined-modality regimens. This approach is very popular in cancer therapy due to the necessity to overcome the emergence of resistance to therapy [1.56]. Targeting the cancer cell on diverse molecular path mechanisms makes the cell less prone to developing resistance to the therapy. At the same time, the use of multimodality therapies allows to decrease the dosage of single therapies, thus reducing side-effects. In the last chapter of this thesis (chapter 6) a preliminary study combining radionuclide therapy (^{177}Lu-cm10, [1.52]) with tyrosine kinases inhibitors is described, based on the assumptions of a possible synergistic effect of the two agents [1.55,1.57–1.59].

1.7 Conclusions

Considering the potential of TRT, in this thesis project a new method for the production of carrier-free radionuclides was studied in order to make the production of radionuclides for medical use possible at the ISOL facility under construction at LNL-INFN. As suggested in the NuPECC report [1.6], the use of nuclear physics facilities for the production of radionuclides for medicine is very important.

On the second part of this thesis, two different strategies to improve TRT were studied: firstly, a set of serum protein binders were radiolabeled and characterized *in vitro* and *in vivo*, secondly a preliminary study for the combination therapy of TKIs with TRT was carried out.

References

[1.1] A. Monetti, A. Andrighetto, C. Petrovich, M. Manzolaro, S. Corradetti, D. Scarpa, F. Rossetto, F. Martinez Dominguez, J. Vasquez, M. Rossignoli, M. Calderolla, R. Silingardi, A. Mozzi, F. Borgna, G. Vivian, E. Boratto, M. Ballan, G. Prete, G. Meneghetti, The RIB production target for the SPES project, Eur. Phys. J. A. 51 (2015). doi:10.1140/epja/i2015-15128-6.

[1.2] F. Borgna, M. Ballan, S. Corradetti, E. Vettorato, A. Monetti, M. Rossignoli, M. Manzolaro, D. Scarpa, U. Mazzi, N. Realdon, A. Andrighetto, A preliminary study for the production of high specific activity radionuclides for nuclear medicine obtained with the isotope separation on line technique, Appl. Radiat. Isot. 127 (2017) 214–226. doi:10.1016/j.apradiso.2017.06.022.

[1.3] S. Corradetti, L. Biasetto, M. Manzolaro, D. Scarpa, S. Carturan, A. Andrighetto, G. Prete, J. Vasquez, P. Zanonato, P. Colombo, C.U. Jost, D.W. Stracener, Neutron-rich isotope production using a uranium carbide - carbon Nanotubes SPES target prototype, Eur. Phys. J. A. 49 (2013) 56. doi:10.1140/epja/i2013-13056-1.

[1.4] C. Müller, K. Zhernosekov, U. Koster, K. Johnston, H. Dorrer, A. Hohn, N.T. van der Walt, A. Turler, R. Schibli, A Unique Matched Quadruplet of Terbium Radioisotopes for PET and SPECT and for - and --Radionuclide Therapy: An *In Vivo* Proof-of-Concept Study with a New Receptor-Targeted Folate Derivative, J. Nucl. Med. 53 (2012) 1951–1959. doi:10.2967/jnumed.112.107540.

[1.5] C. Müller, E. Fischer, M. Behe, U. Köster, H. Dorrer, J. Reber, S. Haller, S. Cohrs, A. Blanc, J. Grünberg, M. Bunka, K. Zhernosekov, N. van der Meulen, K. Johnston, A. Türler, R. Schibli, Future prospects for SPECT imaging using the radiolanthanide terbium-155 - production and preclinical evaluation in tumor-bearing mice, Nucl. Med. Biol. 41 (2014) 58–65. doi:10.1016/j.nucmedbio.2013.11.002.

[1.6] M.J. Garcia Borge, Nuclear Physics for Medicine, 2014. doi:10.1080/10619127.2014.912054.

[1.7] A. Vértes, S. Nagy, Z. Klencsar, R.G. Lovas, F. Rosch, Handbook of Nuclear Chemistry, Second, Springer US, Boston, MA, 2011. doi:10.1007/978-1-4419-0720-2.

[1.8] M.J. Welch, C.S. Redvanly, eds., Handbook of Radiopharmaceuticals, John Wiley & Sons, Ltd, Chichester, UK, 2002. doi:10.1002/0470846380.

[1.9] C.-H. Yeong, M. Cheng, K.-H. Ng, Therapeutic radionuclides in nuclear medicine: current and future prospects., J. Zhejiang Univ. Sci. B. 15 (2014) 845–63. doi:10.1631/jzus.B1400131.

[1.10] H. Jadvar, Targeted Radionuclide Therapy: An Evolution Toward Precision Cancer Treatment, Am. J. Roentgenol. 209 (2017) 277–288. doi:10.1002/oby.21042.Prevalence.

[1.11] D. Wild, J.B. Bomanji, P. Benkert, H. Maecke, P.J. Ell, J.C. Reubi, M.E. Caplin, Comparison of ^{68}Ga-DOTANOC and ^{68}Ga-DOTATATE PET/CT within patients with gastroenteropancreatic neuroendocrine tumors., J. Nucl. Med. 54 (2013) 364–72. doi:10.2967/jnumed.112.111724.

[1.12] M. de Jong, W.A. Breeman, D.J. Kwekkeboom, R. Valkema, E.P. Krenning, Tumor imaging and therapy using radiolabeled somatostatin analogues, Acc. Chem. Res. 42 (2009) 873–880. doi:10.1021/ar800188e.

[1.13] C. Sachpekidis, M. Eder, K. Kopka, W. Mier, B.A. Hadaschik, U. Haberkorn, A. Dimitrakopoulou-Strauss, ^{68}Ga-PSMA-11 dynamic PET/CT imaging in biochemical relapse of prostate cancer, Eur. J. Nucl. Med. Mol. Imaging. 43 (2016) 1288–1299. doi:10.1007/s00259-015-3302-4.

[1.14] A. Afshar-Oromieh, H. Hetzheim, W. Kübler, C. Kratochwil, F.L. Giesel, T.A. Hope, M. Eder, M. Eisenhut, K. Kopka, U. Haberkorn, Radiation dosimetry of ^{68}Ga-PSMA-11 (HBED-CC) and preliminary evaluation of optimal imaging timing, Eur. J. Nucl. Med. Mol. Imaging. 43 (2016) 1611–1620. doi:10.1007/s00259-016-3419-0.

[1.15] C. Kratochwil, F.L. Giesel, M. Eder, A. Afshar-Oromieh, M. Benešová, W. Mier, K. Kopka, U. Haberkorn, [177Lu]Lutetium-labelled PSMA ligand-induced remission in a patient with metastatic prostate cancer, Eur. J. Nucl. Med. Mol. Imaging. 42 (2015) 987–988. doi:10.1007/s00259-014-2978-1.

[1.16] R.P. Baum, H.R. Kulkarni, Theranostics: From molecular imaging using Ga-68 labeled tracers and PET/CT to personalized radionuclide therapy - the bad berka experience, Theranostics. 2 (2012) 437–447. doi:10.7150/thno.3645.

[1.17] A.I. Kassis, Therapeutic Radionuclides: Biophysical and Radiobiologic Principles, Semin. Nucl. Med. 38 (2008) 358–366.

doi:10.1053/j.semnuclmed.2008.05.002.

[1.18] M.D. Wissing, F.W.B. Van Leeuwen, G. Van Der Pluijm, H. Gelderblom, Radium-223 chloride: Extending life in prostate cancer patients by treating bone metastases, Clin. Cancer Res. 19 (2013) 5822–5827. doi:10.1158/1078-0432.CCR-13-1896.

[1.19] C. Müller, N.P. van der Meulen, M. Benešová, R. Schibli, Therapeutic Radiometals Beyond ^{177}Lu and ^{90}Y: Production and Application of Promising α-Particle, β^--Particle, and Auger Electron Emitters, J. Nucl. Med. 58 (2017) 91S–96S. doi:10.2967/jnumed.116.186825.

[1.20] A.I. Kassis, The Amazing World of Auger Electrons, Int. J. Radiat. Biol. 80 (2004) 789–803. doi:10.1080/09553000400017663.

[1.21] A. Cole, Absorption of 20-eV to 50,000-eV Electron Beams in Air and Plastic, Radiat. Res. 38 (1969) 7. doi:10.2307/3572707.

[1.22] C. Müller, J. Reber, S. Haller, H. Dorrer, P. Bernhardt, K. Zhernosekov, A. Türler, R. Schibli, Direct *in vitro* and *in vivo* comparison of ^{161}Tb and ^{177}Lu using a tumour-targeting folate conjugate, Eur. J. Nucl. Med. Mol. Imaging. 41 (2014) 476–485. doi:10.1007/s00259-013-2563-z.

[1.23] S. Haller, G. Pellegrini, C. Vermeulen, N.P. van der Meulen, U. Köster, P. Bernhardt, R. Schibli, C. Müller, Contribution of Auger/conversion electrons to renal side effects after radionuclide therapy: preclinical comparison of ^{161}Tb-folate and ^{177}Lu-folate, EJNMMI Res. (2016) 1–11. doi:10.1186/s13550-016-0171-1.

[1.24] J. Grünberg, D. Lindenblatt, H. Dorrer, S. Cohrs, K. Zhernosekov, U. Köster, A. Türler, E. Fischer, R. Schibli, Anti-L1CAM radioimmunotherapy is more effective with the radiolanthanide terbium-161 compared to lutetium-177 in an ovarian cancer model, Eur. J. Nucl. Med. Mol. Imaging. 41 (2014) 1907–1915. doi:10.1007/s00259-014-2798-3.

[1.25] S.M. Qaim, Therapeutic radionuclides and nuclear data, Radiochim. Acta. 89 (2001) 297–302. doi:10.1524/ract.2001.89.4-5.297.

[1.26] S.M. Qaim, R. Capote, F. Tarkanyi, Nuclear Data for the Production of Therapeutic Radionuclides, Trs 473. (2011) 395.

[1.27] G.C. Krijger, B. Ponsard, M. Harfensteller, H.T. Wolterbeek, J.W.F. Nijsen, The necessity of nuclear reactors for targeted radionuclide therapies, Trends

Biotechnol. 31 (2013) 390–396. doi:10.1016/j.tibtech.2013.04.007.

[1.28] N. Drude, L. Tienken, F.M. Mottaghy, Theranostic and nanotheranostic probes in nuclear medicine, Methods. (2017). doi:10.1016/j.ymeth.2017.07.004.

[1.29] N. Krall, J. Scheuermann, D. Neri, Small targeted cytotoxics: Current state and promises from DNA-encoded chemical libraries, Angew. Chemie - Int. Ed. 52 (2013) 1384–1402. doi:10.1002/anie.201204631.

[1.30] D. Hanahan, R.A. Weinberg, Review Hallmarks of Cancer : The Next Generation, Cell. 144 (2011) 646–674. doi:10.1016/j.cell.2011.02.013.

[1.31] P.A. Van Schouwenburg, G.M. Bartelds, M.H. Hart, L. Aarden, G. Jan, D. Wouters, A novel method for the detection of antibodies to adalimumab in the presence of drug reveals " hidden " immunogenicity in rheumatoid arthritis patients, J. Immunol. Methods. 362 (2010) 82–88. doi:10.1016/j.jim.2010.09.005.

[1.32] M. Fani, G.P. Nicolas, D. Wild, Somatostatin Receptor Antagonists for Imaging and Therapy, J. Nucl. Med. 58 (2017) 61S–66S. doi:10.2967/jnumed.116.186783.

[1.33] C.J. Choy, X. Ling, J.J. Geruntho, S.K. Beyer, J.D. Latoche, B. Langton-Webster, C.J. Anderson, C.E. Berkman, ^{177}Lu-labeled phosphoramidate-based PSMA inhibitors: The effect of an albumin binder on biodistribution and therapeutic efficacy in prostate tumor-bearing mice, Theranostics. 7 (2017) 1928–1939. doi:10.7150/thno.18719.

[1.34] P. Low, S. Kularatne, Folate-targeted therapeutic and imaging agents for cancer, Curr. Opin. Chem. Biol. 13 (2009) 252–262. doi:10.1016/j.cbpa.2009.03.022.

[1.35] N. Parker, M.J. Turk, E. Westrick, J.D. Lewis, P.S. Low, C.P. Leamon, Folate receptor expression in carcinomas and normal tissues determined by a quantitative radioligand binding assay, Anal. Biochem. 338 (2005) 284–293. doi:10.1016/j.ab.2004.12.026.

[1.36] P.S. Low, W.A. Henne, D.D. Doorneweerd, Discovery and Development of Folic-Acid-Based Receptor Targeting for Imaging and Therapy of Cancer and Inflammatory Diseases, Acc. Chem. Res. 41 (2008) 120–129. doi:10.1021/ar7000815.

[1.37] C. Müller, Folate based radiopharmaceuticals for imaging and therapy of cancer and inflammation., Curr. Pharm. Des. 18 (2012) 1058–83.

http://www.ncbi.nlm.nih.gov/pubmed/22272825.

[1.38] E.J. Rolleman, M. Melis, R. Valkema, O.C. Boerman, E.P. Krenning, M. De Jong, Kidney protection during peptide receptor radionuclide therapy with somatostatin analogues, Eur. J. Nucl. Med. Mol. Imaging. 37 (2010) 1018–1031. doi:10.1007/s00259-009-1282-y.

[1.39] B. Erbas, M. Tuncel, Renal Function Assessment During Peptide Receptor Radionuclide Therapy, Semin. Nucl. Med. 46 (2016) 462–478. doi:10.1053/j.semnuclmed.2016.04.006.

[1.40] D. Bisello, J. Esposito, P. Mastinu, G. Prete, L. Silvestrin, J. Wyss, The QMN Beam Line of the Neutron-induced Single Event Effects Facility at the 70 MeV Cyclotron of LNL-INFN, Phys. Procedia. 60 (2014) 271–277. doi:10.1016/j.phpro.2014.11.037.

[1.41] T. Nilsson, European RIB facilities - Status and future, Nucl. Instruments Methods Phys. Res. Sect. B Beam Interact. with Mater. Atoms. 317 (2013) 194–200. doi:10.1016/j.nimb.2013.06.037.

[1.42] I. Kuroda, Effective use of strontium-89 in osseous metastases, Ann. Nucl. Med. 26 (2012) 197–206. doi:10.1007/s12149-011-0560-5.

[1.43] F. Shi, X. Zhang, K. Wu, F. Gao, Y. Ding, R. Maharjan, R. Zhang, F. Zhang, C. Li, Metastatic malignant melanoma: computed tomography-guided ^{125}I seed implantation treatment., Melanoma Res. 24 (2014) 137–43. doi:10.1097/CMR.0000000000000028.

[1.44] G. Rodrigues, X. Yao, A.D. Loblaw, M. Brundage, J.L. Chin, Low-dose rate brachytherapy for patients with low- or intermediate-risk prostate cancer: a systematic review, Can. Urol. Assoc. J. 7 (2013) 463. doi:10.5489/cuaj.1482.

[1.45] A. Wyszomirska, Iodine-131 for therapy of thyroid diseases. Physical and biological basis., Nucl. Med. Rev. Cent. East. Eur. 15 (2012) 120–3. http://www.ncbi.nlm.nih.gov/pubmed/22936505.

[1.46] C. Müller, M. Bunka, S. Haller, U. Koster, V. Groehn, P. Bernhardt, N. van der Meulen, A. Turler, R. Schibli, Promising Prospects for ^{44}Sc-/^{47}Sc-Based Theragnostics: Application of 47Sc for Radionuclide Tumor Therapy in Mice, J. Nucl. Med. 55 (2014) 1658–1664. doi:10.2967/jnumed.114.141614.

[1.47] M. Manzolaro, G. Meneghetti, A. Andrighetto, Thermal-electric numerical simulation of a surface ion source for the production of radioactive ion beams,

Nucl. Instruments Methods Phys. Res. Sect. A Accel. Spectrometers, Detect. Assoc. Equip. 623 (2010) 1061–1069. doi:10.1016/j.nima.2010.08.087.

[1.48] M. Manzolaro, A. Andrighetto, G. Meneghetti, A. Monetti, D. Scarpa, M. Rossignoli, J. Vasquez, S. Corradetti, M. Calderolla, G. Prete, Ongoing characterization of the forced electron beam induced arc discharge ion source for the selective production of exotic species facility, Rev. Sci. Instrum. 85 (2014) 2–4. doi:10.1063/1.4857175.

[1.49] M. Manzolaro, A. Andrighetto, G. Meneghetti, M. Rossignoli, S. Corradetti, L. Biasetto, D. Scarpa, A. Monetti, S. Carturan, G. Maggioni, Ionization efficiency estimations for the SPES surface ion source, Nucl. Instruments Methods Phys. Res. Sect. B Beam Interact. with Mater. Atoms. 317 (2013) 446–449. doi:10.1016/j.nimb.2013.07.045.

[1.50] M. Manzolaro, G. Meneghetti, A. Andrighetto, G. Vivian, F. D'Agostini, Thermal-electric coupled-field finite element modeling and experimental testing of high-temperature ion sources for the production of radioactive ion beams, Rev. Sci. Instrum. 87 (2016) 2–5. doi:10.1063/1.4933081.

[1.51] A. Ruggiero, C.H. Villa, E. Bander, D.A. Rey, M. Bergkvist, C.A. Batt, K. Manova-Todorova, W.M. Deen, D.A. Scheinberg, M.R. McDevitt, Paradoxical glomerular filtration of carbon nanotubes., Proc. Natl. Acad. Sci. U. S. A. 107 (2010) 12369–74. doi:10.1073/pnas.0913667107.

[1.52] C. Müller, H. Struthers, C. Winiger, K. Zhernosekov, R. Schibli, DOTA conjugate with an albumin-binding entity enables the first folic acid-targeted ^{177}Lu-radionuclide tumor therapy in mice., J. Nucl. Med. 54 (2013) 124–131. doi:10.2967/jnumed.112.107235.

[1.53] C.E. Dumelin, S. Trüssel, F. Buller, E. Trachsel, F. Bootz, Y. Zhang, L. Mannocci, S.C. Beck, M. Drumea-Mirancea, M.W. Seeliger, C. Baltes, T. Müggler, F. Kranz, M. Rudin, S. Melkko, J. Scheuermann, D. Neri, A portable albumin binder from a DNA-encoded chemical library, Angew. Chemie - Int. Ed. 47 (2008) 3196–3201. doi:10.1002/anie.200704936.

[1.54] S.C. Penchala, M.R. Miller, A. Pal, J. Dong, N.R. Madadi, J. Xie, H. Joo, J. Tsai, P. Batoon, V. Samoshin, A. Franz, T. Cox, J. Miles, W.K. Chan, M.S. Park, M.M. Alhamadsheh, A biomimetic approach for enhancing the *in vivo* half-life of peptides, Nat. Chem. Biol. 11 (2015) 793–798. doi:10.1038/nchembio.1907.

[1.55] M.R. Gill, N. Falzone, Y. Du, K.A. Vallis, Targeted radionuclide therapy in combined-modality regimens, Lancet Oncol. 18 (2017) e414–e423. doi:10.1016/S1470-2045(17)30379-0.

[1.56] J.S. Lopez, U. Banerji, Combine and conquer: challenges for targeted therapy combinations in early phase trials, Nat. Rev. Clin. Oncol. 14 (2016) 57–66. doi:10.1038/nrclinonc.2016.96.

[1.57] M. Nyati, M. Morgan, F. Feng, T. Lawrence, Integration of EGFR inhibitors with radiochemotherapy, Nat. Rev. Cancer. 6 (2006) 876–85. doi:10.1038/nrc1953.

[1.58] M.P. Kelly, S.T. Lee, F.T. Lee, F.E. Smyth, I.D. Davis, M.W. Brechbiel, A.M. Scott, Therapeutic efficacy of ^{177}Lu-CHX-A″-DTPA-hu3SI93 radioimmunotherapy in prostate cancer Is enhanced by EGFR inhibition or docetaxel chemotherapy, Prostate. 69 (2009) 92–104. doi:10.1002/pros.20856.

[1.59] J. Karar, A. Maity, Modulating the tumor microenvironment to increase radiation responsiveness, Cancer Biol Ther. 8 (2009) 1994–2001. doi:10.1086/498510.Parasitic.

Chapter 2

Secondary targets production and characterization

2.1 Introduction

The first part of this work was devoted to the design, production and characterization of solid secondary targets suitable for the implantation and recovery of the accelerated ions, each one having peculiar characteristics. The main requirements to be addressed for the choice of the target material were: the mechanical stability, the easiness in recovering the ions from the target and the lack of chemical incompatibilities and of isotopic contaminants.

For the deposition of metals with a high boiling point, such as Sr^{2+}, Y^{3+} and Cu^{2+}, sodium chloride was used as a target [2.1]; for the deposition of iodine, an element that is at the gaseous state in high vacuum [2.2], activated carbon mixed with a binder was chosen.

Sodium chloride (NaCl) is an inorganic salt, commonly used in the parenteral formulation of drugs [2.3]. It is biocompatible and used to guarantee the proper osmolarity to the solutions. The use of a defined amount of NaCl for the preparation of a fixed number of radiopharmaceutical doses by direct dissolution of the target material after irradiation allows the obtainment of the drug by a direct and straightforward method. This is useful for the obtainment of $^{89}SrCl_2$ for the treatment of bone metastases [2.4]. On the other hand, if the implanted radionuclides are intended for the radiolabeling of biomolecules, the NaCl should be considered a suitable material because Na^+ ions are usually present in the radiolabeling solutions, so they are not competitors of the radionuclide for the chelator, e.g. DOTA. It should be noted anyway that in most cases the ISOL method will lead to the presence of isobaric contaminants on the secondary target, requiring a purification step (see chapter 4). The capacity of NaCl to form compact substrates was tested without the use of any binder and the properties of the obtained pellets were studied.

Activated Carbon (AC) is an organic material in the form of a very thin powder (nanoscale) and high flowability. It was considered as a suitable material for the development of the secondary target for iodine, since iodide (I^-) is a contaminant of NaCl. Moreover, AC is not toxic and it is an adsorbent material for iodine, commonly used at the industrial level for the recovery of radioactive iodine [2.5]. The aim of this second part of the chapter was the development of a suitable method for the compression of AC by means of a biocompatible binder. For the use of AC as food supplement, it is commonly mixed with several binders: sorbitol, polyvinylpyrrolidone, arabic gum, starch and cellulose derivatives. In this work an effort was made to reduce the number of ligands to only one binder in order to minimize the number of possible chemical incompatibilities with iodine. Among all of them polyvinylalcol (PVA) was chosen. PVA is a water-soluble synthetic polymer in the crystalline form, described by the general formula $[CH_2CH(OH)]_n$. It is a hot binder used in the industrial and in the pharmaceutical field. In the latter in particular it is useful in the 3D printing processes, in the formulation of tablets coating and in the production of medical device. PVA was studied for the production of AC monoliths by Lozano-Castelló *et al.* [2.6]. The possible formation of the complex I_2-PVA was reported by Moulay, [2.7]; this possibility was verified in our working conditions.

2.2 Materials and Methods

2.2.1 Materials

Sodium Chloride, Metal Free (Sigma Aldrich), Stearic Acid (Vegetable) (A.C.E.F.); Caolino USP, Argilla Bianca USP (A.C.E.F.); Activated Carbon, Carbo Activatus USP (A.C.E.F.); Mycrocellulose Crystalline, T1 Ph.Eur. (A.C.E.F.); Veegum Pure (Eico Novachem); Magnesium stearate (Farmalabor); Liquid paraffin BFR070 FU (A.C.E.F.); Poly(vinyl alcohol), PVA, AMw 31000-50000, 98-99% hydrolyzed (Sigma-Aldrich); Aerosil 200 (A.C.E.F.); Sorbitolum PLV. FU-Ph.Eur. (A.C.E.F.); Talco Pharma USP-Ph.Eur.(A.C.E.F.).

2.2.2 Sodium Chloride preparation and compression

For the preparation of the NaCl secondary targets, sodium chloride (Fluka Analytical, TraceSelect) or Sodium Chloride (Sigma Aldrich) were used for the deposition of copper and yttrium beams, respectively. In both cases, NaCl was previously ground in a ceramic mortar for 5 minutes and subsequently sieved. The fraction with a particle size > 63 μm and < 300 μm was used for the preparation of the targets. The powders were then compressed into thin discs using cylindrical molds of 13 mm and 40 mm diameter. For the smaller diameter mold NaCl amounts ranging from ~0.05 to ~1.00 g were pressed applying a strength of 10 tons for 10 minutes in a manual hydraulic press. For the bigger mold, from ~1.50 up to ~3.50 g of NaCl were pressed in an industrial hydraulic press with a strength of 30 tons for 10 minutes.

2.2.3 Sodium Chloride discs characterization

The discs obtained with the previously described method were characterized in terms of mechanical resistance, behavior in vacuum conditions and solubility properties.

To test the mechanical resistance a Texture Analyzer (TA-HDi - Stable Micro System) was used. The measurements were carried out by setting the lowering of the probe to 40% of the disc thickness. Three independent discs were tested for every NaCl weight, a $p < 0.05$ was considered statistically significant.

To verify the behavior of the discs under high vacuum, that is one of the conditions which the secondary targets have to survive to, three discs were placed inside a high vacuum chamber (10^{-6} mbar) at room temperature (RT) overnight. The discs were weighed before and after the treatment and the weight loss [%] was calculated.

To verify the capacity of the discs to disaggregate in a short period of time, the ~1.00 g 13 mm discs and the ~3.60 g 40 mm discs were placed inside a glass vessel filled with 40 and 400 mL deionized water at RT, respectively. The solutions were continuously mixed with a rotating palette (rotating speed = 100 rpm) and the disaggregation of the discs was considered completed when no more residual was visible.

The total porosity (P) of the discs was calculated with the equation 2.1:

$$P = \left(1 + \frac{\rho_c}{\rho_{th}}\right) \cdot 100 \qquad (2.1),$$

where ρ_c is the bulk density calculated experimentally by the mass over volume ratio and ρ_{th} is the theoretical density, a tabulated ideal density that the material would have if

it was completely dense, without any porosity. The ρ_{th} for NaCl is 2.16 g/cm^3. Images of the discs surface were taken with an optical microscope.

2.2.4 Activated Carbon discs preparation

Activated carbon powder was mixed with different ligands in order to evaluate the best ligand to produce a solid AC matrix. AC, indeed, could not be transformed into a compact form by direct compression of the powder. Four different ligands were taken into consideration: microcrystalline cellulose (MC), sorbitol, stearic acid and PVA [2.3,2.6].

AC was mixed with MC in two different ratios: AC 85% : MC 15% and AC 70% : MC 30%. After mixing ~0.80 g of the blend were transferred to a 40 mm diameter mold and pressed applying a strength of 30 tons for 30 min.

AC/sorbitol blends were prepared with a granulation process. Sorbitol was dissolved in deionized water at the concentration of 10 and 30% (g/100 mL). The solution was added dropwise to a known amount of AC powder (~1 g) under continuous mixing in a ceramic mortar until the following AC/sorbitol ratios (w/w) were obtained: ~ 80%/20%; ~ 60%/40%; ~ 50%/50%; ~ 30%/70%. The granules were then dried overnight at 50°C. ~0.8 g of the granules were pressed as previously described for the AC/MC blends.

The lipophilic ligand stearic acid was used at the maximum concentration of 3% (w/w). It was first reduced to smaller pieces manually in a mortar and then mixed with the AC powder. Also in this case ~0.80 g of the mixture were pressed as previously described in the 40 mm mold.

The last tested ligand was polyvinylalcol (PVA). PVA (M_w 31,000-50,000, 98-99% hydrolyzed, T_g 85 °C, T_m 230 °C) was dissolved in distilled boiling water (5%, g/100 mL) and added to the AC powder until an over wetting of the powder was reached. The wet mixture was then dried overnight at 50 °C. The wetting with the PVA solution and the drying was repeated more than once to reach an AC/PVA ratio of 50:50 (w/w). The obtained granules were then grounded and sieved. ~1.30 g (particle size > 300 μm) of the granules were transferred to a preheated mold (~ 170 °C) and pressed for 10 minutes with a strength of 2 tons.

2.2.5 Activated Carbon/PVA discs characterization

The discs that were resistant enough to be handled where characterized in terms of mechanical resistance, loss of weight under high vacuum, superficial structure analysis, total porosity and specific surface area. The discs that were characterized were those with PVA as a binder.

One disc was stored in a Petri dish at RT in normal atmosphere for 24 hours, another disc was stored inside a closed bag filled with argon. The two discs were then transferred into a high vacuum chamber (~10^{-6} mbar) overnight and the weight loss was measured. The same discs, plus one more that was stored in argon atmosphere after pressing, were then measured for the mechanical resistance with a Texture Analyzer as previously described.

Some fragments of one of the discs tested for the mechanical resistance were analyzed by Scanning Electron Microscopy (SEM) analysis using a Vega3 Tescan microscope. Images of the surface and of the internal section of the discs were taken at magnitude of 100 and 1000 x, high voltage 15.0 kV and working distance ~15.00 mm. SEM pictures of the AC and of the granules before compression were also taken at 100 x of magnitude with the same instrumental setup.

The total porosity was calculated with the formula 2.1, previously described. The theoretical density (ρ_{th}) of the mixture was extrapolated with the formula 2.2:

$$\rho_{th} = \rho_{th,AC} \cdot \nu_{AC} + \rho_{th,PVA} \cdot \nu_{PVA} \quad (2.2),$$

where $\rho_{th,AC}$ = 2.00 g/cm^3, $\rho_{th,\ PVA}$ = 1.27 g/cm^3 and ν_{AC} and ν_{PVA} are the volumetric fractions of the two phases in the mixture, easily calculated being their masses and densities known.

The samples were characterized also in terms of specific surface area. The AC raw powder, the granules before compression and a compressed disc underwent physisorption analysis, with ASAP^{TM}2020 Micrometrics. ~0.03 g of AC, ~0.22 g of granules and a fragment of a disc of ~0.49 g were independently analyzed. All the samples underwent a degassing preparatory phase at 100 °C, 60 °C and 100 °C, respectively, for 720 min. The temperature was lower for the granules to avoid a change in the structure during the degassing ($T_{g,\ PVA}$ = 85 °C). The discs had already been kept at higher temperatures during compression (~170 °C) so a temperature of 100 °C was not considered a problem. After the degassing, the samples were weighed and analyzed.

The analysis gas was N_2, the specific surface area was calculated with the BET method and the pore size distribution in the mesopore region (2nm < pore size < 50 nm) with the BJH method.

2.2.6 Interaction between I_2 and PVA

The formation of complexes between PVA and Iodine was reported in the literature [2.7]. To evaluate if this was the case also in our working conditions, ~0.65 g of PVA were soaked in a solution of NaOH (1 M, 2 mL) and I_2 (0.05 M, 2 mL). The mixture was shaken and centrifuged at 5000 rpm at RT for 5 minutes. The supernatant was analyzed at the UV-Vis spectrophotometry (baseline NaOH 1 M). As reported in literature, the PVA-I_2 complex is colored with λ_{max} in the visible range [2.7].

2.3 Results and discussion

2.3.1 Sodium chloride discs preparation

The direct compression of the sieved NaCl powder allowed to produce solid discs without the addition of any ligand both using the 13 and the 40 mm mold (picture in figure 2.1), with minimum amounts of 0.70 and 1.50 g of NaCl, respectively. The discs presented homogeneous surfaces and no visible crack were present (figure 2.1).

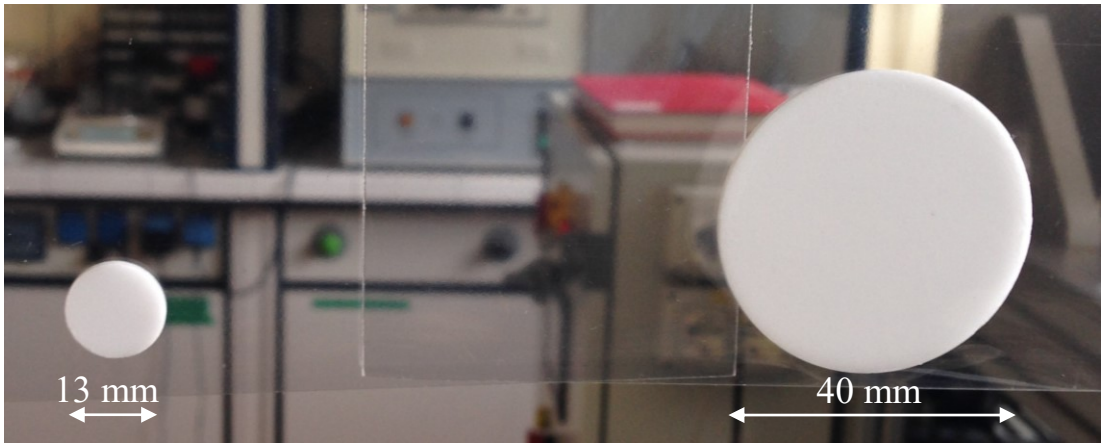

Figure 2.1. The Sodium Chloride disks (13 and 40 mm of diameter).

2.3.2 Sodium chloride discs characterization

The strength necessary to break the discs was measured with the texture analyzer. All the produced discs showed a good resistance. For the 13 mm discs those of mass >0.40

g a strength >50.0 N was necessary to break them. For those of masses ranging from 0.07 to 0.20 g no significant difference was measured (~15 N). The resistance increased with the mass to a maximum strength of ~150 N. The average strength with the SD are reported in figure 2.2 A and B. No weight loss was measured after the permanence in high vacuum.

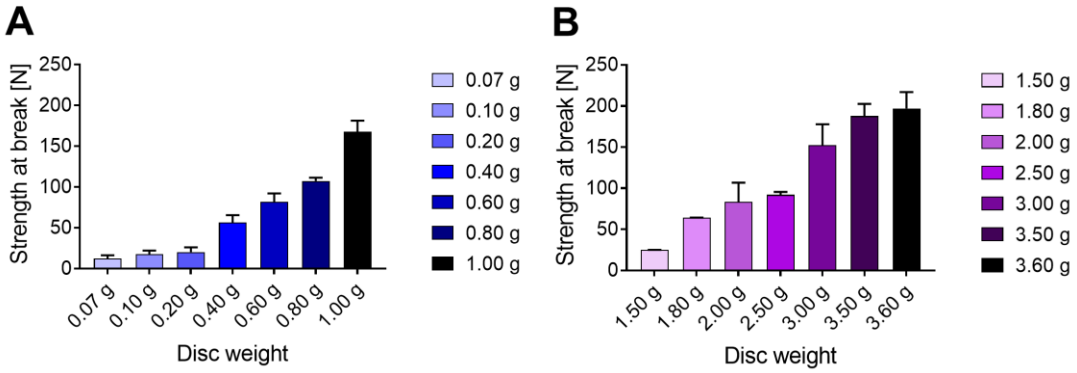

Figure 2.2. Results of the mechanical tests performed on the 13 mm discs (A) and on the 400 mm ones (B).

The calculation of the total porosity (P) applying formula 2.1 on the ~1.8 g discs highlighted a low degree of total porosity (6.86% ± 2.30), see table 2.1, meaning a high degree of fusion of the NaCl grains. This is also visible from the pictures taken with the optical microscope on the discs surface (Figure 2.3A and B) where the fusion of NaCl granules is clearly visible.

Table 2.1. Calculation of the total porosity (P) on three discs of 1.8 g, diameter 40 mm.

Disc	**Mass**	**Volume**	**Bulk density** (ρ_c)	**Total porosity (P)***
	[g]	[cm^3]	[g/cm^3]	[%]
1	1.80	0.89	2.02	6.40
2	1.82	0.93	1.96	9.34
3	1.81	0.88	2.06	4.85
			Average	**6.86**
			SD	**2.30**

*Calculated with formula 2.1 and a $\rho_{th,NaCl}$=2.16 g/cm^3

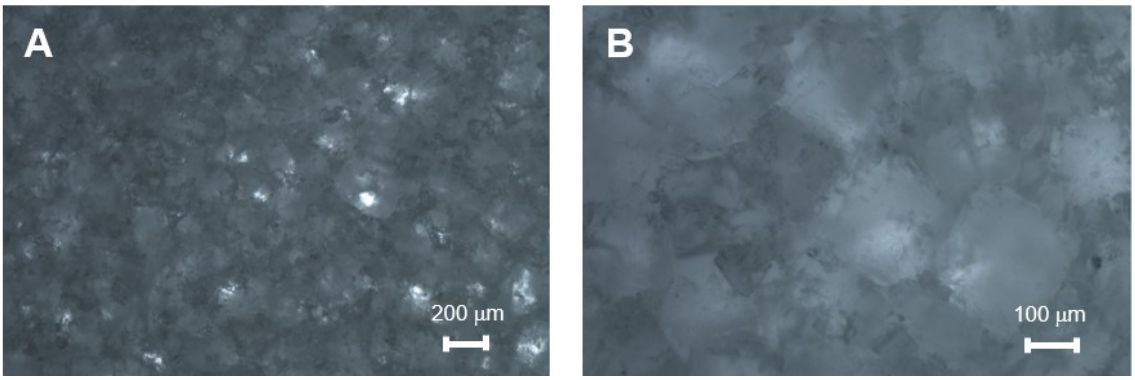

Figure 2.3. Pictures of the surface of NaCl discs.

2.3.3 Activated Carbon discs preparation

Using the AC/MC mixtures it was not possible to obtain solid discs: after the compression time, when the mold was opened the blend was still in the powder form. When sorbitol was used as a ligand a slight compression was reached when the sorbitol [%] was >70%. Nevertheless, a solid matrix could not be achieved. The AC/stearic acid powder gave the same result: no compression could be achieved. The compression of the AC/PVA blend, performed by hot pressing, instead lead to a good mechanical stability of the pressed discs, which were consequently characterized.

2.3.4 Activated Carbon/PVA discs characterization

The disc that was stored in normal atmosphere after compression, had a weight loss of ~4.13% after staying in high vacuum overnight, while the disc that was immediately transferred into a bag filled with argon had a much lower weight loss (~0.90%). These two discs tested at the texture analyzer had a breaking strength of 9.53 N and 95.04 N. A third disc, conserved in argon, was broken applying a strength of 104.15 N (see figure 2.4).

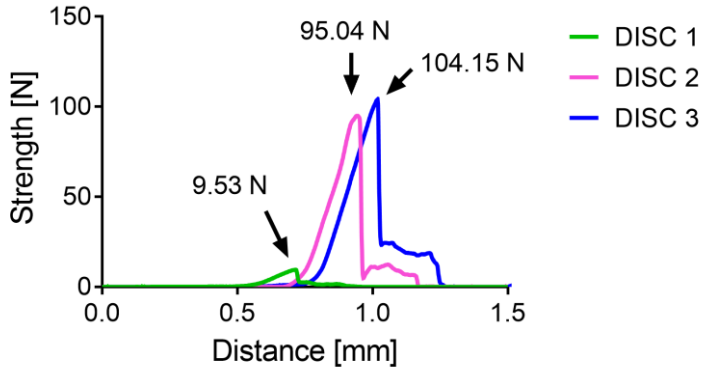

Figure 2.4. Graphs of the mechanical tests performed on the AC/PVA discs.

The specific surface area of the powder calculated with the BET method showed a significant decrease from the pure AC powders to the AC/PVA granules and AC/PVA discs. The firsts have, indeed, a specific surface area of 1602 m^2/g, while the seconds two had values of 169 and 188 m^2/g, respectively. The three isotherm curves could be classified according to the IUPAC classification (figure 2.5) [2.8].

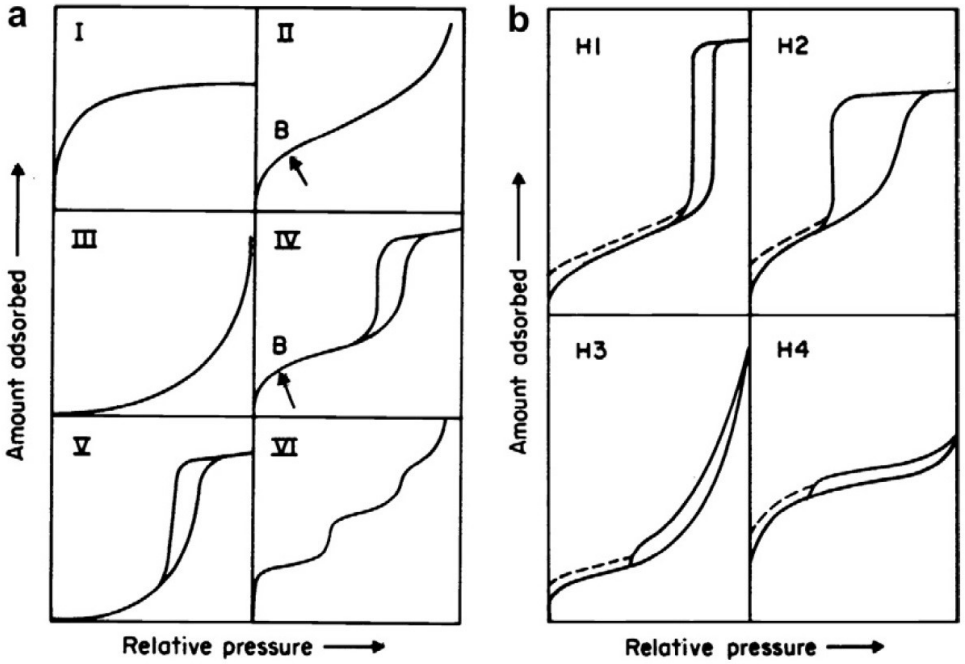

Fig.2.5. IUPAC classification of Isotherm curves.

The pure AC isotherm (fig. 2.6A) could be classified as type I for the first region. The sharp increase at low p/p^0 ratios was typical of the presence of micropores (<2 nm). The hysteresis was due to the presence of mesopores: moreover the mesopores shape could be predicted since the hysteresis was of the H4 type (Fig. 2.5b), suggesting the presence of narrow and long pores. The curve did not reach the saturation, probably due to the presence of macropores as well. AC/PVA granules and discs both had a H4 typehysteresis and lack the saturation step as well (fig 2.6 B and C).

The high degree of porosity of the AC/PVA discs is confirmed from the calculated total porosity (P) that was 44.57% ± 1.60. In table 2.2 the parameters used for the determination of the theoretical porosity of the AC/PVA blend is reported. Table 2.3 reports the calculated total porosity (P).

Table 2.2. Parameters used for the total porosity calculations for AC/PVA discs.

$\rho_{th,AC}$ [g/cm^3]	$\rho_{th,PVA}$ [g/cm^3]	Volume AC [cm^3]	Volume PVA [cm^3]	ν_{AC}	ν_{PVA}	Theorical Density $\rho_{thAC/PVA}$ [g/cm^3]
2.00	1.27	0.03	0.47	0.39	0.61	1.55

Table 2.3. Calculation of total porosity (P) for AC/PVA discs.

Disc	Mass [g]	Volume [cm^3]	Bulk density (ρ_c) [g/cm^3]	Total porosity (P)* [%]
1	1.269	1.487	0.85	45.05
2	1.256	1.421	0.88	43.08
3	1.251	1.508	0.83	46.58
4	1.256	1.512	0.83	46.51
5	1.259	1.421	0.89	42.95
6	1.259	1.458	0.86	44.40
7	1.256	1.458	0.86	44.53
8	1.255	1.396	0.90	42.11
9	1.204	1.433	0.84	45.90
			Average	**44.57**
			SD	**1.6**

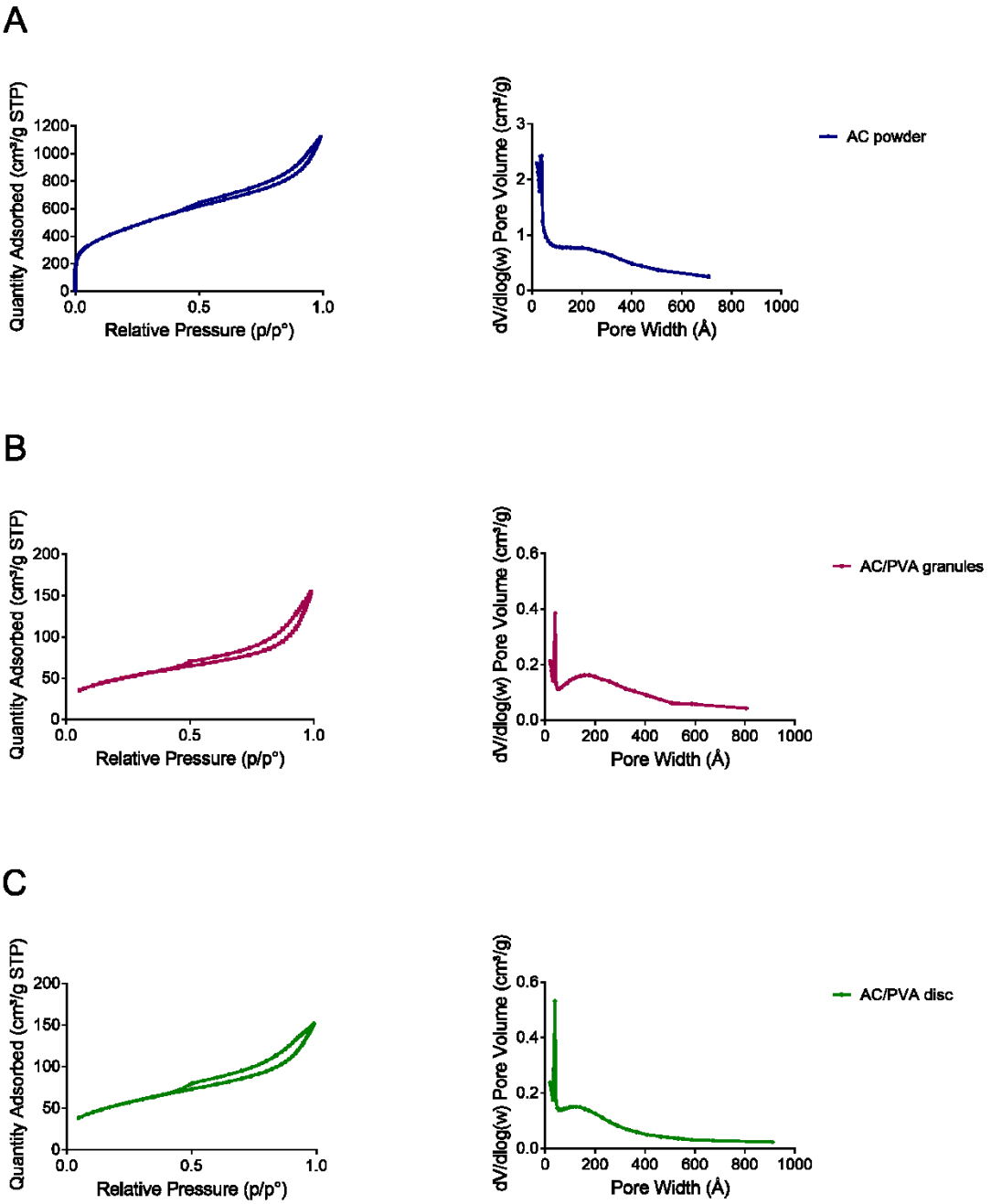

Figure 2.6. Isotherm curves (on the left) and pore distribution profiles (on the right) for pure AC powder (A), AC/PVA granules (B) and AC/PVA discs (C).

The pore distribution (Figure 2.6 A, B and C, right side) confirmed the presence of micro and mesopores in the AC powder, and mesopores only in the AC/PVA granules and disc.

With the SEM analysis we observed the distribution of PVA around the AC powder (figure 2.7A and B) and confirmed the good success of the compression process (figure 2.7 C-F). The surface showed a good homogeneity with the presence of bigger and

smaller granules kept together by PVA (figure 2.7C and 2.7D). The presence of macropores is confirmed from the SEM pictures.

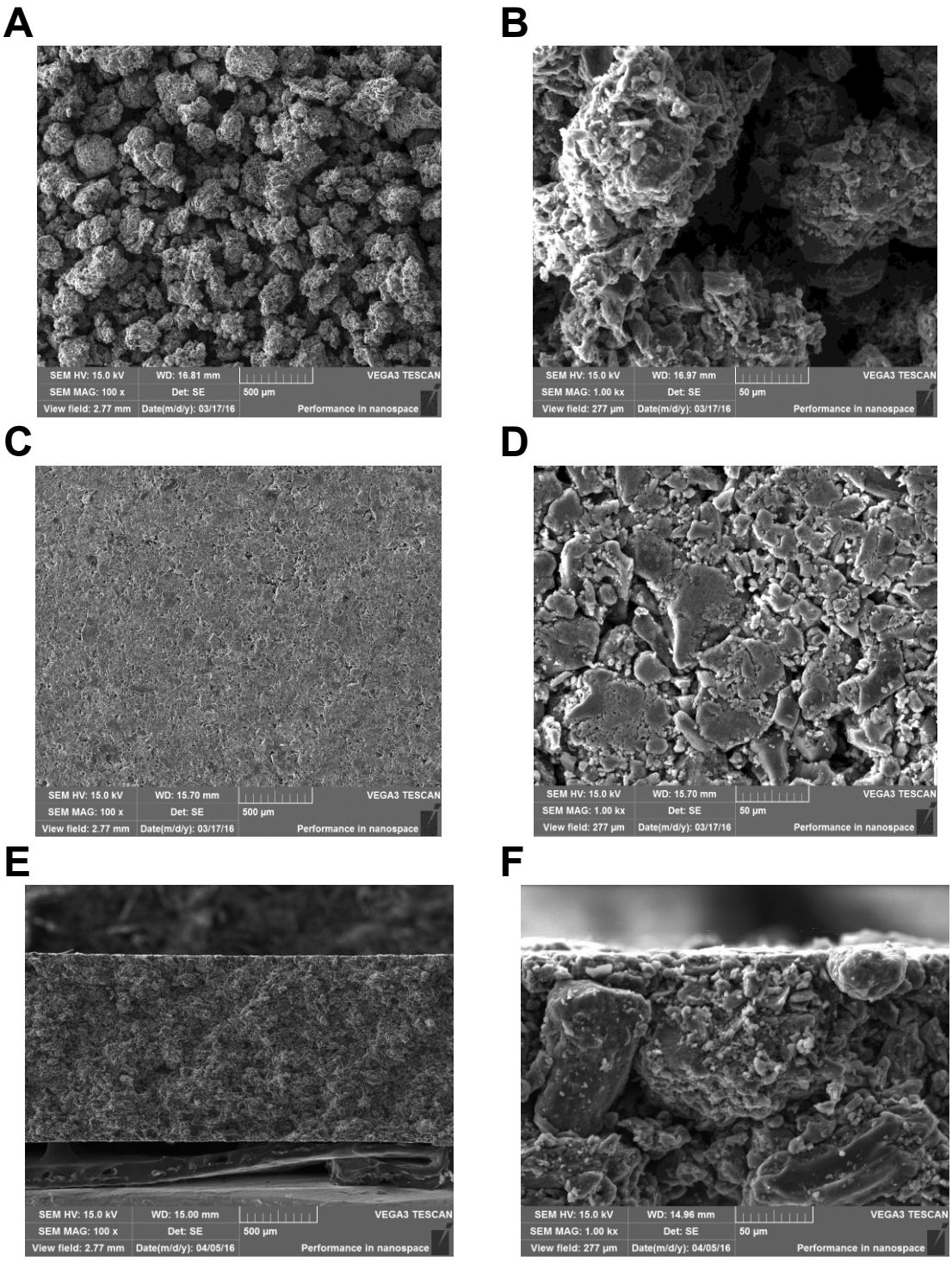

Figure 2.7. SEM images at 100 x (left) and 1.0 kx (right) of AC/PVA granules (A) and (B), AC/PVA discs surface (C) and (D) and AC/PVA discs section (E) and (F).

2.3.5 Interaction between I_2 and PVA

After the addition of PVA to the NaOH solution, the polymer started to swell due to water adsorption and accumulated at the bottom of the tube. The I_2 gave a reddish color to the solution that vanished fast due to iodine dismutation to I^- and IO_3^- in basic conditions. No colored I_2-PVA complex was visible and no typical UV spectrum could be observed.

2.4 Discussion

This study was fundamental for the design and development of solid substrates useful for the deposition of accelerated ion beams. These substrates were used for the experiments described in chapter 3.

Sodium chloride could be easily pressed in the form of a disc without the addition of any binder. Its ability to form compact matrixes is probably due to its hygroscopicity. Thanks to the absence of binders no compatibility issues had to be taken into account. Nevertheless, it was important to establish the smaller quantity necessary to have a substrate with acceptable mechanical characteristics (1.8 g for the 40 mm discs and 0.5 g for the 13 mm) because a too large amount of NaCl can be a problem for: (*i*) interference with the chemical analysis of the deposed elements; (*ii*) osmotic pressure of the solution prepared after the disc dissolution. The produced discs were, indeed, used for the deposition and quantification of stable elements, for this reason different analytical techniques were used depending on the element, as described in chapter 3. These techniques foresee the dissolution of the elements (for their quantification) and of sodium chloride simultaneously. Reducing its amount was necessary to have accurate and precise analyses.

The compression of activated carbon represented a bigger challenge because different ligands were taken into consideration. PVA was the only one that could be used efficiently to produce solid AC discs. High temperature pressing (160 °C) had to be used to allow the transition of the polymer to its glass phase, without melting it (T_g 85 °C, T_m 230 °C). A granulation process of the AC powder using a solution of the polymer was done before the compression, the final blend had AC and PVA in a ratio of 1:1. The produced discs had a good mechanical resistance if stored in argon atmosphere; the absorption of water was, indeed, cause of a decrease in the mechanical

resistance of the 1st disc (~9 N vs. >90 N for the disc kept under argon) and underwent a weight loss after vacuum treatment (~5% of the initial weight). The discs had a good total porosity (~45%) and high specific surface area (~170 m^2/g), meaning a high surface available for the I_2 adsorption. The chemical compatibility between the ligand PVA and I_2 was verified and no complex was formed.

2.5 Conclusions

With this study it was possible to produce the secondary targets for the ion beams deposition. These targets could be produced after compression of the materials with the addition of PVA as a binder in the case of activated carbon and without any binder in the case of sodium chloride. As described in chapter 3 these substrates could be used for the deposition of stable accelerated yttrium, copper and iodine.

The discs were characterized and proved to have good mechanical and superficial properties. The use of the discs as secondary targets and their installation in the beam line is described in chapter number 3.

References

[2.1] F. Borgna, M. Ballan, S. Corradetti, E. Vettorato, A. Monetti, M. Rossignoli, M. Manzolaro, D. Scarpa, U. Mazzi, N. Realdon, A. Andrighetto, A preliminary study for the production of high specific activity radionuclides for nuclear medicine obtained with the isotope separation on line technique, Appl. Radiat. Isot. 127 (2017) 214–226. doi:10.1016/j.apradiso.2017.06.022.

[2.2] Honig RE, Radio Corporation of America Vapor Pressure Data for the Solid and Liquid Elements, RCA Rev. 23 (1962) 567–586.

[2.3] R.C. Rowe, P.J. Sheskey, W.G. Cook, M.E. Fenton, Handbook of Pharmaceutical Excipients, 7th ed., 2012.

[2.4] I. Kuroda, Effective use of strontium-89 in osseous metastases, Ann. Nucl. Med. 26 (2012) 197–206. doi:10.1007/s12149-011-0560-5.

[2.5] D. Haefner, T. Tranter, Methods of gas phase capture of iodine from fuel reprocessing off-gas: A literature survey, Idaho Natl. Lab. (2007). doi:10.2172/911962.

[2.6] D. Lozano-Castelló, D. Cazorla-Amorós, A. Linares-Solano, D.. Quinn, Activated carbon monoliths for methane storage: influence of binder, Carbon N. Y. 40 (2002) 2817–2825. doi:10.1016/S0008-6223(02)00194-X.

[2.7] S. Moulay, Molecular iodine/polymer complexes, J. Polym. Eng. 33 (2013) 389–443. doi:10.1515/polyeng-2012-0122.

[2.8] K.S.W. Sing, Reporting physisorption data for gas/solid systems with special reference to the determination of surface area and porosity (Provisional), Pure Appl. Chem. 54 (1982). doi:10.1351/pac198254112201.

Chapter 3

Stable Ion Beams tests

The results regarding iodine and yttrium reported in this chapter were recently published in the journal Applied Radiation and Isotopes (DOI: 10.1016/j.apradiso.2017.06.022).

3.1 Introduction

To study the feasibility of the use of SPES, a Front-End (FE) was built in recent years and used in this work in off-line mode (not connected to the proton beam line) to ionize, accelerate and collect stable beams of elements of interest. More details on the FE architecture and operation will be given in 3.2.2.

Like already reported in Chapter 1, SPES is a second generation ISOL facility [3.1]; the ISOL method guarantees the production of high intensity Radioactive Ion Beams (RIBs) that can be purified On Line thanks to a mass separator [3.2]. The use of the ISOL method for the production of radionuclides for nuclear medicine relies on the possibility to perform mass separation, thus getting rid of all isotopic impurities eventually present after the desired nuclear reaction [3.3,3.4]. High purity coupled with high intensities guarantees the production of carrier-free radionuclides, ready for the radiolabeling of diagnostic or therapeutic agents. A step of chemical purification from isobaric contaminants has to be considered in case of long-lived radioisotopes of the same mass chain co-produced with the desired radionuclide (See Chapter 4).

In this study yttrium, copper and iodine were ionized and accelerated with the FE and collected on the secondary targets described in chapter 2. The elements collected on the substrates were analyzed and quantified. The process developed with stable ion beams will be the same that will be performed with the radioactive ones. Their chemical behavior, indeed, is the same. These tests thus represented a proof of principle of the validity of the separation and collection methodologies that will be used in ISOLPHARM.

Yttrium beams were produced because ^{90}Y is a radionuclide used in therapy [3.5], that can be produced with the ISOL method from ^{238}U fission (primary proton beam 40 MeV, 200 μA) in a uranium carbide target [3.6]. The UC_x target is the main target currently under development for the SPES project [3.7,3.8].

^{64}Cu and ^{67}Cu are ISOLPHARM radionuclides that will be produced from targets alternative to UC_x. Nickel based targets are currently under development for the production of ^{64}Cu, and germanium based targets (such as zirconium germanide) for the production of both ^{64}Cu and ^{67}Cu, as explained in chapter 1. The couple $^{64}Cu/^{67}Cu$ is a perfect matched pair because the two radionuclides can be used to perform diagnosis (^{64}Cu) and therapy (^{67}Cu) of a patient using the same element, having this way the same chemical behavior [3.9].

Iodine was studied since ^{131}I and ^{125}I are radionuclides already used in nuclear medicine [3.10–3.13] and are produced inside the SPES uranium carbide fission target . Moreover, other interesting iodine radionuclides are produced from this target, like ^{127}I.

3.2 Materials and Methods

3.2.1 Materials

Copper Standard for AAS TraceCERT (Fluka Analytical), Yttrium Standard for AAS TraceCERT (Fluka Analytical) and Yttrium Chloride hexahydrate 99.99% trace metal basis (Sigma Aldrich) were used for copper and yttrium beams production and sodium chloride (Sigma Aldrich) was used to develop substrates for yttrium deposition. Nitric acid 69.0% TraceSELECT (Fluka Analytical) was used for sample preparation in copper and yttrium analysis. Active charcoal Carbo Activatus USP (A.C.E.F.) and Poly(vinyl alcohol) AMw 31000-50000, 98-99% hydrolyzed (Sigma Aldrich) were used for the production of the substrate to collect iodine beams.

Formic acid 99-100% AnalaR Normapur Analytical reagent (Prolabo), Sulfuric Acid 95-97% for analysis or manufacturing use (J.T. Baker), Bromine reagent grade (Sigma Aldrich), Potassium iodate 99.5% for analysis (ACROS Organics), Potassium Iodide puriss p.a. reag. ISO, reag. Ph. Eur. 99.5% (Sigma Aldrich) and Sodium Thiosulphate solution 0.1mol/L (Scharlab S.L.) were used for Iodine analysis. Sodium Hydroxide

reagent grade 98%, pellets (anhydrous) (Sigma-Aldrich) was used for iodine extraction from the substrate prior to analysis.

3.2.2 Front End description

The experimental apparatus installed at LNL allowed the performance of some preliminary tests to verify the production of radionuclides of pharmaceutical grade with the ISOL technique. For this purpose, the SPES Front End off-line was used. This apparatus, schematically represented in figure 3.1, has been designed and developed for the SPES project and is aimed at the production of (1^+) ion beams. It is currently used in off-line mode, i.e. for the acceleration of stable ion beams; it is not connected to the proton beam line. Once the set up will be completed, it will be moved to a dedicated bunker in the final SPES building and coupled to the cyclotron line.

Figure 3.1. Scheme of the SPES FE.

To study the production of a radionuclide with the ISOL technique to obtain radiopharmaceutical products, stable isotopes of the same element can be a good alternative, since they have the same chemical behavior. For this reason, the FE was used to produce stable ion beams to carry out the feasibility tests here reported.

The FE has been extensively described in previous papers [3.14]. Briefly, it is made of five main functional subsystems: the ion source complex, the beam optics subsystem, the Wien filter, the diagnostic boxes 1 and 2. The ion source complex is placed inside a vacuum chamber that enables the use of the ion source at high temperatures with pressure levels between 10^{-5} and 10^{-6} mbar. In off-line mode, no fissile target is installed inside the chamber but different methodologies are used to introduce the stable isotopes to be ionized and accelerated depending on the physical state of the element. In the case of gases, they are introduced through a controlled gas flow and injected in the ion source by means of a calibrated leak; in case of solid materials, they are usually soluble

salts, dissolved in acidic media and quantitatively deposed and solvent evaporated on a tantalum foil, called mass marker (MM). The MM is then carefully folded [3.15] and inserted into a heated tantalum tube, called oven, that allows the element atomization and injection into the ion source. More details on this technique will be given in the next paragraph.

The ion sources developed for the SPES project are of two kinds, depending on the first ionization potential of the element [3.14,3.16]. For elements of the 1st and 2nd group, the Surface Ion Source (SIS) is adopted; for those with higher electronegativity, the Plasma Ion Source (PIS) is required.

The SPES SIS is a hot-cavity ion source and its components are mainly made of tantalum [3.15]. Geometric specifications of the SIS ion source used to perform the tests are reported by Manzolaro et al. [3.15]. Surface ionization occurs following the interaction of the atoms with a heated surface; the interaction causes the loss of an electron and the production of a positive singly charged ion. This mechanism [3.17] is good only for elements with a first ionization potential smaller than 7 eV and with a hot-cavity made of materials with high work function values (like tantalum) [3.18]. The operating temperature of the source is a crucial parameter to achieve an effective ionization.

The ion source used in these tests is the SPES PIS, which is a forced electron beam induced arc discharge ion source [3.14,3.16]. It is a non-selective device capable of ionizing a large spectrum of elements, mainly composed of two parts: the tantalum cathode and the molybdenum anode. The former is heated at 2200 °C by the Joule effect, generating an intense thermionic emission of electrons (free electrons) on the cathode surface facing the anode. The anode, at 150 V with respect to the rest of the ion source, attracts the ionizing electrons, in this way allowing the creation of a plasma inside its cylindrical cavity. PIS is also suitable for ionization of elements with high first ionization potential.

The ion source (SIS or PIS) is placed on a 25 kV platform with respect to the extraction electrode at ground potential. The high voltage can however be increased to 40 kV. The beam optics subsystem is made of a set of electrostatic deflectors and a quadrupole triplet which allow beam alignment and focusing, respectively. In diagnostic box 1 there is a Faraday Cup (FC) for beam intensity monitoring and a grid-based beam profile (BP) detector.

The beam mass selection is performed by a Wien Filter (WF) [3.19] a device which is able to select a specific ion due to mutually perpendicular electric and magnetic fields orthogonal to the ion velocity. The undeflected particles have speed equal to the ratio between electric and magnetic field. The deflected ions are then stopped by a slits subsystem. Since the various masses have approximately the same energy (25 keV), this device can be used in the FE as a mass selector. For this reason, the Wien Filter is composed by a vacuum chamber where two electrodes, maintained at a certain potential, provide the desired electric field and by a magnet excited by two coils, that supplies the magnetic field.

Following mass separation, a second diagnostic box is installed, constituted by a FC, a grid-based BP detector and an emittance meter device.

For the simulation of the radionuclide production for the development of radiopharmaceuticals precursors, a substrate of pharmaceutical grade is positioned at the end of the line, immediately after the emittance meter in order to collect the desired accelerated stable ions.

3.2.3 The Mass Marker technique

The Mass Marker capillary technique [3.20] is a useful method for the introduction of atoms into the front end. It is used to simulate the process of diffusion of radioactive isotopes towards the ionization source in the off line tests. It consists of a small tantalum foil (mass marker) on which a calibrated volume of the solution containing the element is placed. The solution is allowed to evaporate, leaving on the marker only the salt [3.21]; then it is accurately folded and introduced inside the oven. The diffusion process is regulated by the temperature and by the vapour pressure of the introduced molecule, that is why the oven is heated by means of Joule effect, a well-established method to heat components of that kind [3.22] and the temperature can be regulated so as to control the diffusion process [3.15].

Depending on the element, different calibrated amounts of standard solutions were loaded on the MM and are reported in the following paragraphs. The most important experimental parameters, used for the ionization and deposition of each element, are summarized in table 3.1.

Table 3.1. Experimental conditions used for copper, yttrium and iodine ionization and depositions.

	Copper	**Yttrium**	**Iodine**
Ionization source	Plasma Ion Source	Plasma Ion Source	Plasma Ion Source
Starting chemical form	Copper nitrate	Yttrium chloride	Potassium iodide
Mass marker placement	Oven	Transfer line	Oven
Solution loaded in the mass marker	Copper nitrate solution (1 g/L), 200 μL	Yttrium chloride (1 g/L), 900 μL	Potassium iodide (1 g/L), 150 μL
Secondary target	Sodium chloride 1.8 g	Sodium chloride 1.8 g	Activated carbon 50% (w/w) PVA 50% (w/w) 1.3 g
Analytical technique	GF-AAS (λ=327.4 nm)	ICP-OES (λ=371.03 nm)	Titration

The setup of the FE was optimized depending on the boiling temperature, mass and first ionization potential of the element under study. In the following, the experimental conditions for yttrium, copper and iodine are reported.

3.2.4 Yttrium Beams [3.1]

3.2.4.1 Yttrium beams production

For yttrium ionization two different salts were used for the preparation of the mass marker: Yttrium Nitrate (Yttrium Standard for AAS, Standard solution, 1000 mg/L) and Yttrium Chloride (Yttrium (III) chloride hexahydrate, Sigma Aldrich, 1000 mg/L dissolved in deionized water). Different volumes (40-900 μL) of the yttrium salts solutions, as per testing, were dropped onto a tantalum foil (10 mm x 15 mm, width 0.025 mm) and the solvent was allowed to evaporate by mild heating. The foil was later folded and connected to the ionization source. To successfully ionize yttrium, the MM was placed in two different positions of the ion source unit: (i) inside the oven or (ii)

directly into the transfer line. The oven is a thin tantalum tube, that is connected to the transfer line and that, thanks to the passage of electric current, is heated up and allows atoms evaporation and migration to the transfer line. The placement of the MM directly into the transfer line, instead, was regarded as unconventional and due to the high yttrium boiling point (~3337 °C), which lead to unsuccessful trials with the conventional method.

The transfer line was heated up with the help of current passage, until a maximum of 420 A which corresponds to about 2200 °C. The line heating allowed yttrium evaporation and atomization. The heating guaranteed also the generation of anode current, as described in paragraph 3.2.2. The extractor was placed at 50% of the distance and at -25 kV from the ionization source. The WF, to separate yttrium (A=89.9) from the other ionized species, was set as follow: electric field 1500 V and current inducing magnetic field 89.8 A. To focus yttrium beam onto the final NaCl target, triplets and deflectors were set to the value reported in table 3.2.

Table 3.2. Triplets and deflectors value for beam focusing.

Deflector 1- S1	1792 V
Deflector 2- S2	0 V
Deflector 3- S3	974 V
Deflector 4- S4	0 V
Triplet 1- Q1	1368 V
Triplet 2- Q2	703 V
Triplet 3- Q3	1276 V

EM allowed the definition of beam dimension and position. It gave as output couples of values x_{max}-x'_{max}, x_{min}-x'_{min} and y_{max}-y'_{max} and y_{min}-y'_{min}, every couple having a value of position (x) and divergence (x') of the beam.

The coordinates of the beam at the NaCl disk were calculated with the following formulas:

$$r_x^+ = x_{max} + x'_{max} \cdot s \quad (3.1),$$

$$r_x^- = x_{min} + x'_{min} \cdot s \quad (3.2),$$

$$r_y^+ = y_{max} + y'_{max} \cdot s \quad (3.3),$$

$$r_y^- = y_{min} + y'_{min} \cdot s \quad (3.4),$$

where *s* is the distance between EM collimator and the disk and had a fixed value of 336 mm.

To verify the composition of the beam (not only yttrium was ionized) several mass scans were carried out. The mass scans were performed thanks to the use of the WF: the electric field was kept constant and the magnetic field was increased in order to deviate the ions depending on their m/q values. A system of slits after the WF was used to allow only the selected mass to pass. Slits were at a distance of 2 or 4 mm depending on beam intensity. The mass scans were performed at each line current, from 350 A to 420 A.

3.2.4.2 Tests preliminary to yttrium beam deposition on NaCl disk

Before performing deposition, some tests were carried out using the same conditions of the deposition to monitor the trend of the beam and predict the number of yttrium atoms impinging the secondary target ad thus develop a suitable analytical method. The data points were then imported with the Software Origin (Version Pro 2015 9.2) and the values of current integrated in time to obtain the value of charge. With the assumption that the charge carried by one single atom is known, i.e. $1.60217662 \times 10^{-19}$ coulombs, the number of deposed atoms were calculated dividing the total charge for the value of charge of one single particle.

3.2.4.3 Yttrium quantification

The analysis method for yttrium was set on the ground of the foreseen yttrium atoms on the secondary substrate. It was assumed that after the deposition the disc was dissolved in 10 mL of HNO_3 0.1 M and analyzed with ICP-OES.

The analytical method was assessed so as to be linear in the concentration range, sensible, accurate and precise. Standards were prepared at 2, 7, 10 e 70 ng/mL using HNO_3 0.1 M + NaCl 18% to obtain the same matrix of the sample. For each

concentration three measures were taken and data fit to obtain calibration curves considering the three wavelengths λ = 371.030 nm, 360.073 nm and 377.433 nm.
In order to find out the best λ for the measurement in terms of precision, accuracy and limit of detection (LD), the following considerations were taken into account [3.23].
LD is the lowest Y^{3+} concentration value satisfying the following equation:

$$|\alpha| + |\sigma| \leq \frac{f\%}{100} \cdot \mu \quad (3.5),$$

where α and σ are accuracy and precision and $f\%$ is the percentage of indetermination admitted in the analysis of the true value concentration μ. Accuracy is calculated through the equation 3.6:

$$|\alpha| = |\bar{V} - \mu| \quad (3.6),$$

where $\bar{V}$ is the mean value of the concentration measurements. To evaluate the quantification method, the equations 3.7 and 3.8 were also considered:

$$DS\% = \frac{\sigma}{\bar{V}} \cdot 100 \quad (3.7),$$

$$W\% = \frac{\bar{V}}{\mu} \cdot 100 \quad (3.8),$$

where DS% is the standard deviation (%) and W% represents the percentage of observed value on the true one. By substitution of equations 3.6, 3.7 and 3.8 into equation 3.5, we obtain:

$$|W\% - 100| + \left|\frac{DS\% \times W\%}{100}\right| \leq f\% \quad (3.9),$$

which, assuming that *f%* = 7.5% [3.23], allows the determination of the LD values. The counts measured for the standards at 7, 10 and 70 ng/mL by the instrument at the three wavelength were used to determine $\bar{V}$, W%, DS% and *f%* and thus determine the best λ.

3.2.4.4 Yttrium deposition

900 μL of yttrium chloride (1000 mg/mL) were loaded onto the MM, evaporated by mild heating and introduced into the transfer line of the SPES PIS. The latter was heated up to ~2000 °C (420 A), the extractor placed at -25 kV, 50% of the distance, the deflectors and triplets set according to the values reported in table 3.2, the WF was switched on (EF 1500 V and current inducing magnetic field 89.8 A) and the slits were left open. A sodium chloride disk (1.8 g) was placed at the end of the line and the

ionized yttrium was collected on it, by leaving all the diagnostic devices out of the beam channel. The FC2 was periodically inserted into the channel to monitor the beam trend and calculate, as described above, the quantity of yttrium atoms impinging the NaCl substrate. The disc was removed after deposition and dissolved in 10 mL of HNO_3 0.1 M. The solution was finally analyzed via ICP-AES (see above).

3.2.5 Iodine Beams [3.1]

3.2.5.1 Iodine beams production and efficiency determination

For ionizing iodine, the FE was used in the same conditions as for yttrium, with the difference that the MM loaded with iodine was inserted in the conventional way, i.e. in the oven, connected to the transfer line of the ion source.

For the ionization efficiency determination 40 μL of KI (1.0 g/L in water) were dropped onto the MM and the solvent evaporated. The MM accurately folded was inserted into the oven and assembled in the ion source. The transfer line was heated to 400 A (~ 2000 °C) and the extraction set at 25 kV. The beam focalization devices were set as follow: S1, S2, S3 and S4 0 V and Q1, Q2 and Q3 1893, 891 and 2010 V, respectively. The Wien Filter was switched on to allow mass separation and isolate the mass 127. To allow iodine evaporation in a controlled manner, the oven was slowly switched on. When the oven was between 5 and 10 A, the iodine was evaporated and consequently ionized.

The secondary target used for Iodine was AC/PVA. Being this kind of target conductive, it was used itself as a faraday cup (called FC3). This allowed to monitor during the depositions tests the quantity of I^+ ions impinging the target. Since this "home-made" FC was not suppressed[2], one test was carried out to calculate the correction factor to apply to eliminate any alteration in the current reading. A comparison of the current was made with FC2 (suppressed), being the closest one to FC3. The integrated charge of FC2 and FC3 over 1000 seconds was compared, when the beam current was constant. Comparison of the two integrated charges allowed to determine the correction factor to apply to the detected current in FC3.

[2] The electron suppressor is a device fed at high voltage and coupled to the faraday cup which provides low error in the beam current measurement. It reduces losses due to the backscattering of incident ions and the emission of secondary electrons due to the beam impact.

3.2.5.2 Iodine beams deposition

Three deposition tests were carried out. Each time 150 μL of KI 1.0 g/L (~1 μmole) were loaded on the MM and introduced in the FE. The deflectors and triplets were set as follow: S1, S2, S3 and S4 = 175, 100, 20 and 30 V and Q1, Q2 and Q3 = 1775, 881 and 2493 V, respectively. The slits were left open. The ionization source, WF and the oven were switched on as described above. After the deposition the disc was removed and iodine extracted.

3.2.5.3 Iodine recovery

The extraction of iodine from the AC/PVA disks was carried out by means of a water solution at basic pH. The addition of NaOH induces iodine dismutation according to reactions:

$$I_2 + 2OH^- \rightarrow I^- + IO^- + H_2O \quad (3.10),$$

$$3IO^- \rightarrow 2I^- + IO_3^- \quad (3.11),$$

These iodine species are water-soluble and for this reason they pass to the water phase and are extracted.

The discs were minced, transferred to a glass tube and 5 mL of NaOH 0.5 M were added. The tube was centrifuged for 5 minutes at 5,000 rpm for 30 min, RT. The supernatant was removed and kept for analysis. The procedure was repeated twice more adding every time 5 mL of NaOH (0.5 M). The second and third part of the extract were added to the first one and analyzed all together. For the third deposition the sample was treated equally, but the procedure was carried out at 55 °C to improve the extraction efficiency.

3.2.5.4 Iodine analysis

The titration method was used. The extracted samples were taken to an acidic pH adding few drops of H_2SO_4 3M (final pH between 4.3 and 5.5). The pH had to be strictly monitored in order to avoid the dismutation of iodine at basic pH (reaction 3.10 and 3.11) and the acidic decomposition of $Na_2S_2O_3$ used for the titration according to the undesired reaction 3.12:

$$S_2O_3^{2-} + H^+ \leftrightarrow HS_2O_3^{2-} \rightarrow HSO_3^- + S\downarrow \quad (3.12).$$

After the H_2SO_4 addition, the sample was treated with bromine water (Br_2). The acidic environment was also necessary to avoid bromine dismutation, reaction 3.13:

$$Br_2 + 2OH^- \rightarrow Br^- + BrO^- + H_2O \quad (3.13),$$

that would consume the reagent necessary for the conversion of all iodine species to iodate (reactions 3.14 and 3.15):

$$I^- + 3Br_2 + 3H_2O \rightarrow IO_3^- + 6\,H^+ + 6Br^- \quad (3.14),$$

$$I_2 + 5Br_2 + 6H_2O \rightarrow 2IO_3^- + 12H^+ + 10Br^- \quad (3.15),$$

For these reactions 1 mL of Br_2 water was added and the solution was stirred for 15 minutes. The unreacted bromine was eliminated by addition of few drops of concentrated formic acid until the solution was completely decolored. To finally convert iodate to iodine for titration, 1 mL of KI (10%) was added to the solution:

$$IO_3^- + 5I^- + 6H^+ \rightarrow 3I_2 + 3H_2O \quad (3.16).$$

Iodine was then quickly titrated with $Na_2S_2O_3$ 10^{-4} M (reaction 3.17):

$$2S_2O_3^{2-} + I_2 \rightarrow S_4O_6^{2-} + 2I^- \quad (3.17).$$

For the determination of the equivalent point, 848 Titrino Plus Metrohm was used. The instrument measures the change in the redox potential of the solution after the addition of the titrant. It has a redox electrode made of a Pt ring and based on the internal standard Ag/AgCl. The titration was carried out with the Dynamic Equivalence Point Titration (DET), where the thyosulphate was added in a volume depending on the slope of the curve. Smaller volumes were added when the end of the titration was close. This allowed to have more accurate results.

3.2.6 Copper beams

Copper beams were produced using the aforementioned apparatus. The plasma ion source was used and sodium chloride, TraceSelect, was chosen for the secondary target production.

3.2.6.1 Copper beams production and ionization efficiency determination

For copper beams production and ionization efficiency determination, the MM and oven systems were used coupled to the SPES PIS. 40 µL of copper standard solution (1 g/L,

Fluka Analytics) were dropped on a 10x10 mm tantalum foil and the MM, after being folded, was inserted into the oven at 80 mm distance from the opening. The oven was then closed on one side and connected to the transfer line on the other one. The following parameters were set for the FE operation: transfer line current 415 A, oven maximum current 80 A, extractor position 50%, S1, S2, S3 and S4 0 V and Q1, Q2 and Q3 1395, 695 and 1398 V. Natural copper is an isotopic mixture: ^{63}Cu (69.17%) and ^{65}Cu (30.83%). For all the tests the most abundant isotope was considered. For the isolation of mass 63, the WF was used (V_p 2579, V_{pe} 590 V[3] and I_{WF} 111 A) and the slits were open (18 mm). The ^{63}Cu beam current was measured until no more current could be detected. The current was integrated and the value of charge calculated.

3.2.6.2 Copper beams deposition and copper analysis

Copper deposition tests were carried out placing the secondary target in a different position of the beam line, due to the upgrades of the FE. A second triplet system was, indeed, installed after the second FC, which allowed a better beam focalization. A third diagnostic unit, equipped with a FC3 and a BP3, was installed at the end of the line. The sodium chloride discs (1.8 g) used for copper deposition were installed inside the new FC. This way the target could be moved in and out from the channel, using the motors of the FC.

Prior to each deposition, one MM loaded with 200 µL of copper nitrate (1 g/L) was inserted into the oven (from 4 to 8 cm from the oven closure) and connected to the PIS transfer line. The slits were open at 18 mm, and the triplets and steerers set as follow: Q1, Q3 and Q3 875, 695 and 1398 V and S1, S2, S3 and S4 0 V. The WF was switched on V_p 2579, V_{pe} 590 V and I_{WF} ~111 A. The I_{WF} was checked prior to each test, closing the slits at 2 mm in order to allow the best mass selection (^{63}Cu). The second triplets subsystem was set as follow: QT1, QT2 and QT3 1760, 850 and 1775 V, respectively. The best focalization was possible thanks to the use of the BP3.

The oven was then switched on, the FC3 with the NaCl disk built on it was put into the channel, while the FC2 and all the other interceptive devices were removed from the channel, to allow the copper beam to impinge on the secondary target. The oven was heated up to a maximum of 65 A, and the deposition carried out for 4-5 hours. The FC2

[3] This parameter Vpe was used only for copper beams, after an upgrade of the FE.

was used to detect the ^{63}Cu current every 20-30 minutes. The values of current were integrated in time using the software Origin Pro (2015) in order to estimate the total copper atoms reaching the NaCl target.

After the deposition, the target was removed and dissolved for analysis. Prior to dissolution, since the beam spot was very clear and to reduce the sodium chloride amount, the portion of the disk were the copper was visible was separated from the rest, breaking the substrate. Two different procedures were followed for copper extraction from the disc. In the first 2 depositions, the disk was dissolved in 20 mL of HNO_3 0.5 M, under stirring and mild heating. After 20 minutes the solution was quantitatively transferred to a 100 mL flask and the volume adjusted with HNO_3 0.5 M. The 3rd and 4th disks were treated differently; after weighing, they were transferred to a Teflon vessel, and 6 mL of concentrated HNO_3 were added. The vessels were then closed and heated up thanks to a microwave oven to 180 °C for 20 minutes. After cooling down, the solutions were transferred to two 50 mL-flasks and the volume adjusted to 50 mL. In both cases standards at 100 μg/L were prepared for Graphite Furnace Atomic Absorption Spectroscopy (GF-AAS, Varian ©, lamp current = 4 mA, λ= 327.4 nm).

3.3 Results

The results of ionization and deposition for yttrium, iodine and copper are here reported.

3.3.1 Yttrium ionization

Yttrium beam production was plagued by difficult atom evaporation. Yttrium has a very high boiling temperature. At atmospheric pressure its boiling point is 3370 °C; this value decreases when operating in vacuum conditions ($5 \cdot 10^{-6}$ mbar), reaching the value of 1600 °C [3.24]. To overcome this limiting factor two different possibilities where studied: (*i*) the choice of the most volatile yttrium salt and (*ii*) the positioning of the MM in the hottest region of the ion source without folding it as in the case of iodine and copper.

Preliminary tests with the conventional MM system were not successful; very low beam currents were produced. For this reason, tests were later performed positioning the MM in the transfer line (40 mm from the gas injection and very close to the hot cavity), after folding the MM only once. With this set-up the observed yttrium currents were higher, up to a value of ~30 nA, when the temperature was ~2200 °C, see figure 3.2.

As already mentioned, the Plasma Ion Source (PIS) was used to ionize yttrium. The crucial parameters for this kind of apparatus are described here. Firstly, the transfer line (later only line) temperature, which was responsible for yttrium evaporation; the heating of the line influenced the cathode temperature as well. The electron current was influenced also by the anode potential, which was fixed at 150 V. Moreover, a constant argon flux was used for plasma formation. To increase the ionization efficiency a small axial magnetic field (current 5 A, max voltage 30 V) was produced in the anode region, with a coil surrounding the ion source. The magnetic field improved the ion source performances by means of a plasma confinement effect. Since the oven was not used (MM placed directly in the transfer line), the only way to control yttrium evaporation was the transfer line heating, which also controlled the electron current, and so yttrium ionization. As can be observed from picture 3.2, sharp peaks were present in the trend of the yttrium beam current throughout the ionization test, corresponding to the imposed increases in the cathode temperature. The cathode was heated up by 420 A in order to obtain yttrium evaporation and ionization; at 380 A, the temperature had been proved to be above 2000 °C [3.16]. The use of the same numerical method allowed the calculation

of the temperature of the transfer line at 420 A which turned out to be higher than 2200 °C.

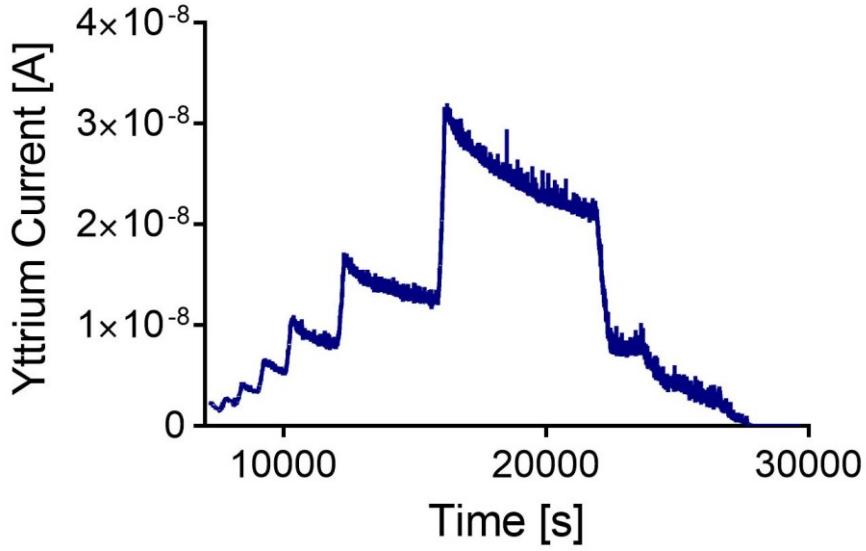

Figure 3.2. Trend of yttrium beams during tests. Sharp peaks correspond to to the increase in the cathode temperature.

From 350 A, electron current was detected and a consistent ion beam was produced. A representative mass scan is presented in figure 3.3A. As can be observed many peaks can be observed at low mass values (N_2 mass 28 for example), but no peak was detected corresponding to mass 89. Figure 3.3B, instead, shows a mass scan obtained after the introduction of YCl_3 in the MM.

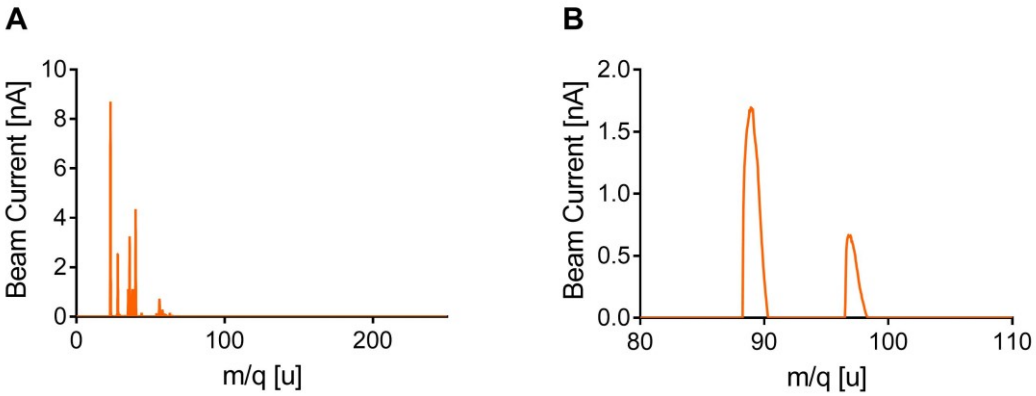

Figure 3.3 (A) Mass scan prior to yttrium introduction. (B) Mass scan evidencing yttrium mass, after yttrium introduction.

Tests were performed to compare yttrium nitrate and chloride as possible species to introduce in the mass marker. As can be observed from the graph of figure 3.4, yttrium chloride gave beam currents higher than those obtained with the nitrate at similar anode currents, i.e. cathode temperatures. For this reason, YCl_3 was chosen for the deposition tests.

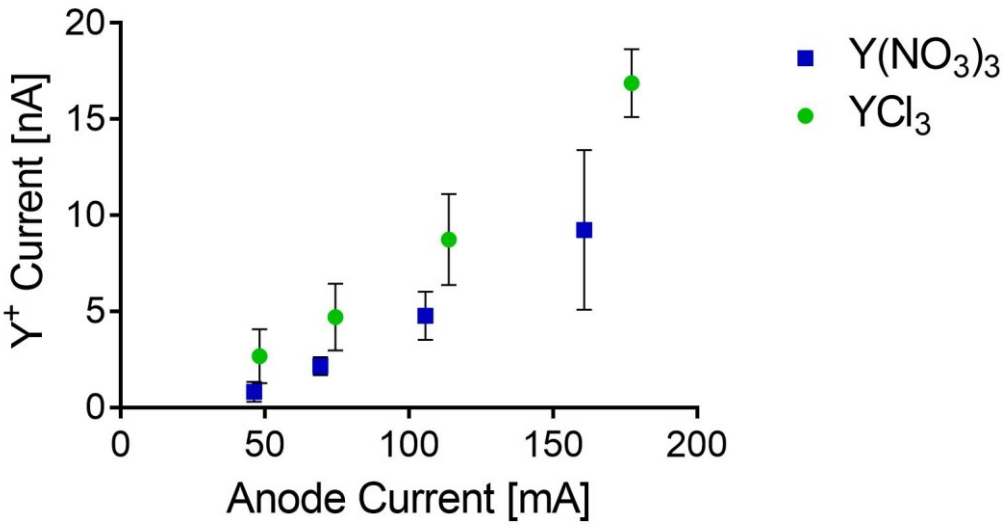

Figure 3.4. Comparison between the yttrium currents in the chloride vs the nitrate form is made. To make a meaningful comparison, the yttrium currents were evaluated at similar anode currents. For each value the chloride gives always higher currents.

We observed that the MMs loaded with $Y(NO_3)_3$, after the heating, had a white fine powder on them. For this reason, we hypothesized the formation of yttrium oxide, a highly refractory material, on the MM.

Before performing deposition, some tests were performed to monitor the trend of the beam current with increasing cathode temperatures, as reported in figure 3.2. The integration of the curve made it possible to calculate the number of atoms in the beam, $N_t = 1.62 \cdot 10^{15}$. This was important to estimate the yttrium quantity on the secondary target. Assuming that the sodium chloride disc would be dissolved in a volume of 10 mL, a concentration of about 24 μg/L was expected in the solution. ICP-OES turned out to be a precise and accurate technique in this concentration range (see paragraph 3.3.2).

3.3.2 Yttrium quantification

In figure 3.5 the three calibration ICP-OES curves at λ = 371.030, 360.073 and 377.433 nm are reported. The experimental data were fitted with a straight line, f(x)=ax+b,

where a and b turned out to be, respectively: 2393 and 179 for λ = 371.030 nm, 1251 and -1210 for λ = 360.730 nm, 1200 and 447 for λ = 377.433 nm.

The one at λ = 371.030 nm turned out to be the best one in terms of sensitivity of the analysis (slope $\lambda_{371.030} = 2394 >> \lambda_{360.073} \sim \lambda_{377.433}$).

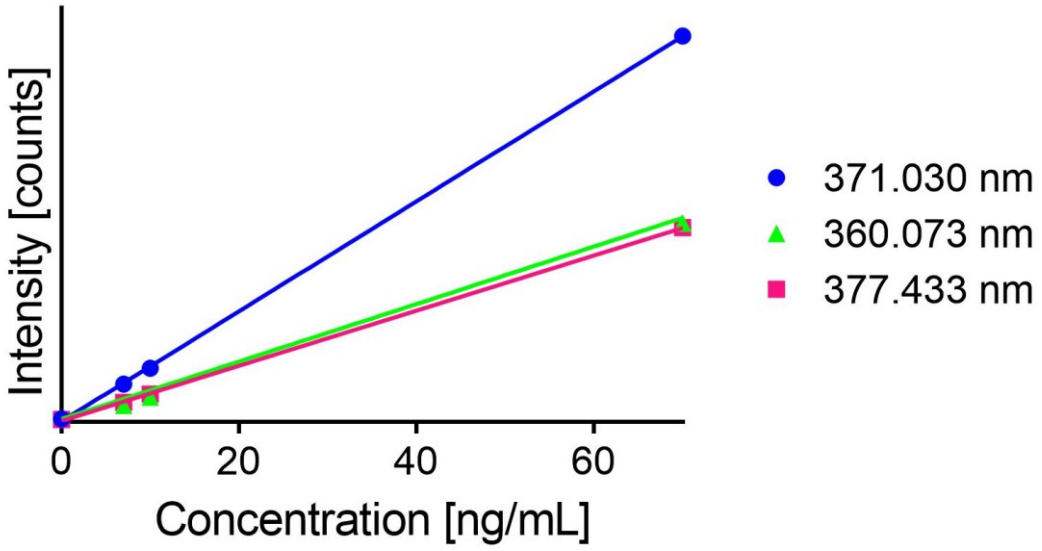

Figure 3.5. Calibration curves for yttrium at three different wavelengths.

In table 3.3 and figures 3.6, 3.7 and 3.8 the observed values, the W% and the DS% are reported for each wavelength. The observed values were calculated from the equation of the straight lines, while W% was calculated according to equation 3.8.

Table 3.3. Results of ICP-OES for yttrium. Comparison of wavelength.

μ	$\bar{V}$			**W%**			**DS%**			***f*%**		
[ng/mL]	371 nm	360 nm	377 nm	371 nm	360 nm	377 nm	371 nm	360 nm	377 nm	371 nm	360 nm	377 nm
0	0.4	0.7	0.5	-	-	-	17.5	20	12.8	-	-	-
7	6.8	6.6	6.7	97.3	95.0	96.2	7.0	4.0	3.4	9.5	8.8	7.1
10	9.7	9.6	9.7	96.9	95.7	97.0	1.3	4.3	1.2	4.3	8.4	4.2
70	70.1	70.1	70.1	100.1	100.1	100.1	3.6	6.0	5.7	3.7	6.1	5.8

The *f*% values calculated from equation 3.9 indicated that the LD values were 10 ng/mL for λ=371 and 377 nm and 70 ng/mL for λ=360 nm, since the percentage of indetermination (*f*%) allowed for the analysis was 7.5 [3.23].

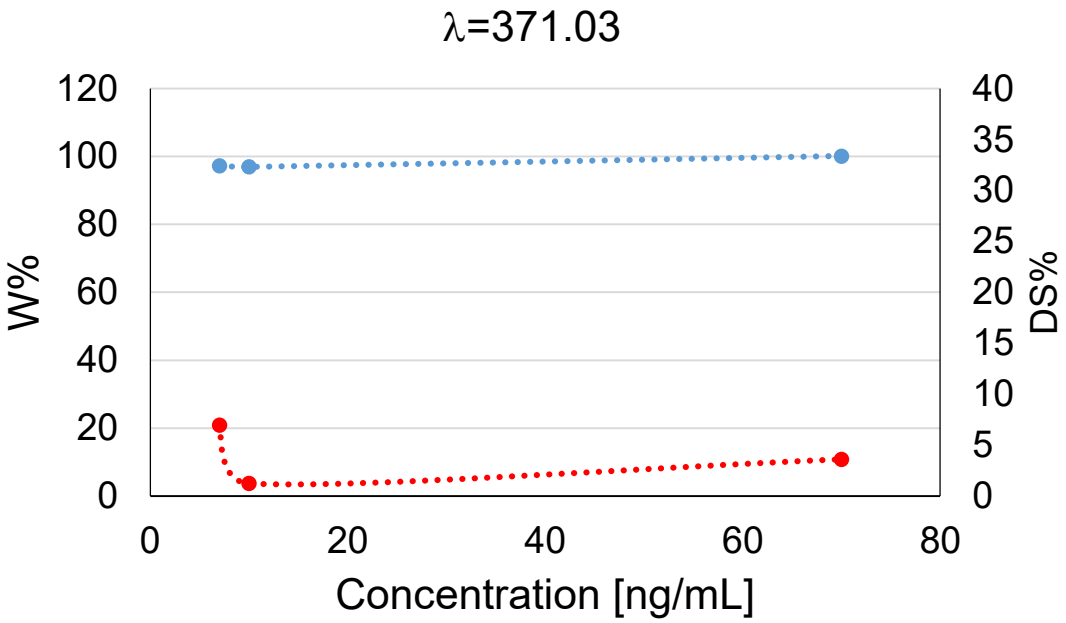

Figure 3.6. Accuracy (blue line) and precision (red line) of the method for the analysis of Y^{3+} at 371.030 nm

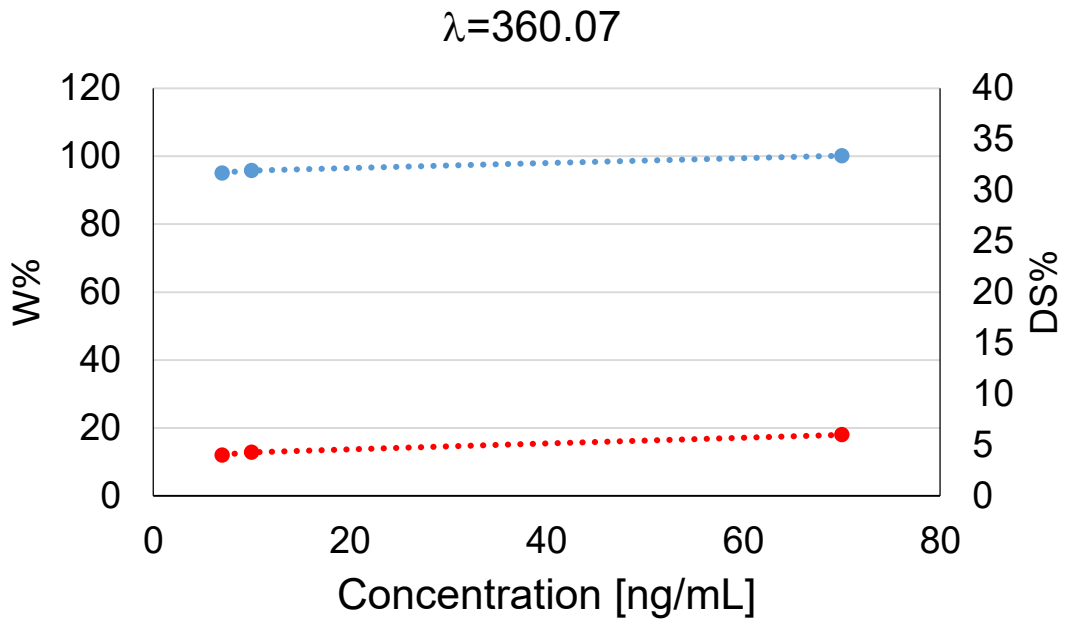

Figura 3.7. Accuracy (blue line) and precision (red line) of the method for the analysis of Y^{3+} at 360.073 nm

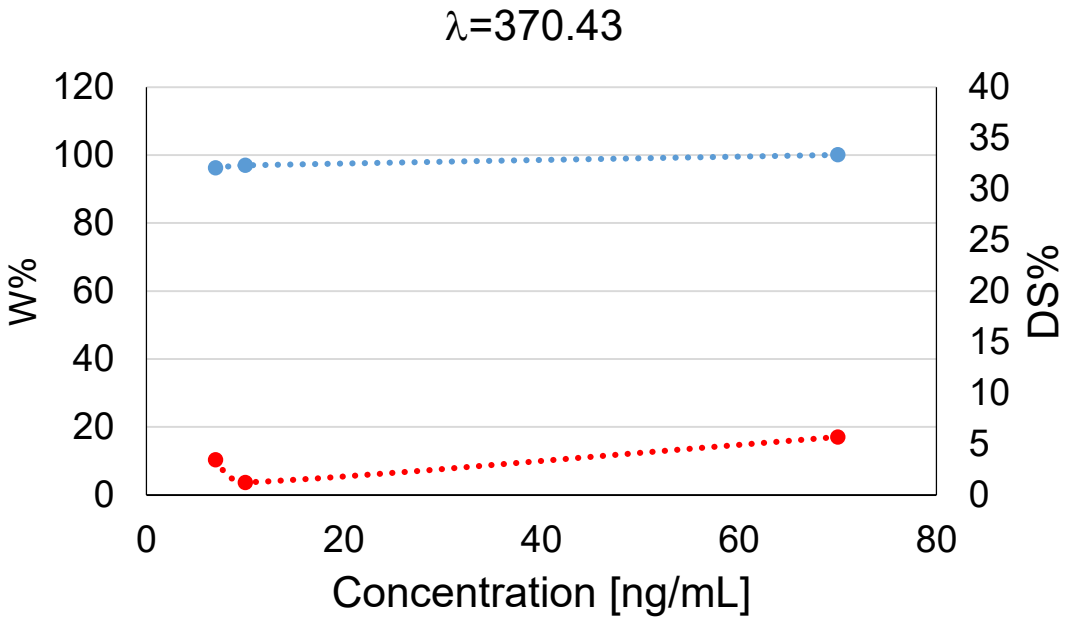

Figura 3.8. Accuracy (blue line) and precision (red line) of the method for the analysis of Y^{3+} at 377.433 nm

Due to the higher sensitivity, accuracy and precision, the analysis were carried out considering the λ=371.03 nm.

3.3.3 Yttrium deposition

The trend of the first deposition test is reported in figure 3.9; the curve was integrated obtaining the values reported in table 3.4 (Test 1). The same was done for test number 2. During the first deposition 1.3×10^{-4} C, corresponding to 8.0×10^{14} yttrium atoms, reached the NaCl target. A second deposition test was carried out, where the yttrium charge impinging the NaCl disk was 10.0×10^{-5} C, corresponding to 6.2×10^{14} atoms. After irradiation, the substrates were dissolved in 10 mL of HNO_3 0.1 M and analyzed by means of ICP-OES. The solution of the first disc had a concentration of 12.96 ±1.4 ng/mL, the second one 5.00 ±0.1 ng/mL, corresponding to 8.78×10^{14} and 3.39×10^{14} yttrium atoms, respectively. The results are summarized in table 3.4.

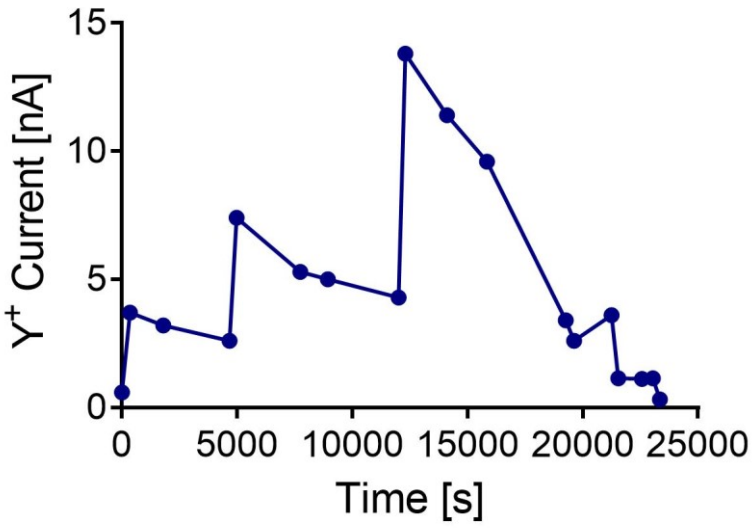

Figure 3.9. Yttrium beam trend during a deposition test. The FC2 was inserted at certain times (blue dots) to monitor the beam. Integration of the curve gives the number of ionized atoms that reach the deposition substrate.

Table 3.4. Results for yttrium depositions.

Test	Integrated charge [C]	Yttrium atoms impinging the target [N]	Yttrium atoms detected with ICP-OES [N]	Atoms recovered from the substrate [%]
1	$1.3 \cdot 10^{-4}$	$8.0 \cdot 10^{14}$	$8.8 \cdot 10^{14}$	100.0
2	$1.0 \cdot 10^{-4}$	$6.2 \cdot 10^{14}$	$3.4 \cdot 10^{14}$	54.8

3.3.4 Iodine

Iodine beams were produced by the SPES FE for the first time. The ionization efficiency of iodine with the SPES PIS was not known so three tests were performed to evaluate it. Efficiency turned out to be 19.34 % (SD=0.34) when operating with the cathode at 400 A. Iodine evaporation was efficiently controlled by means of the oven heating. No close interfering masses were observed as shown in figure 3.10. Iodine evaporation and consequently its ionization started at oven currents of 10 A.

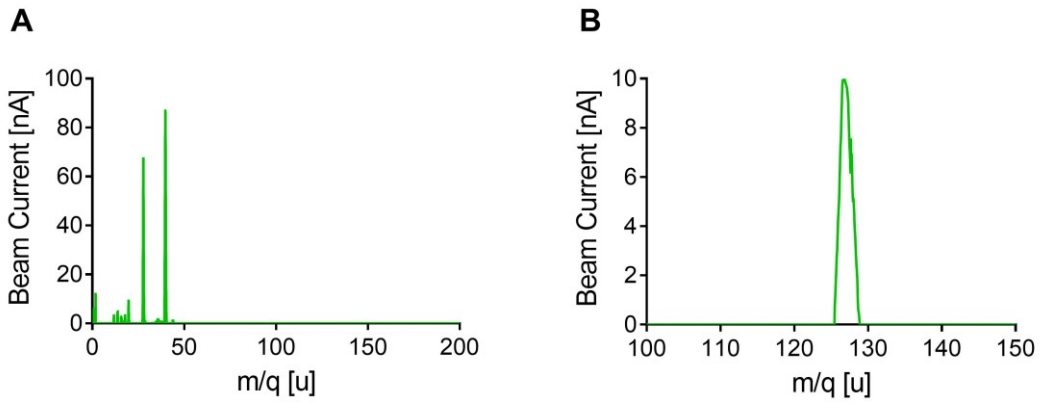

Figure 3.10. (A) Mass scan prior to iodine introduction. (B) Mass scan after iodine introduction and oven heating.

Analytical methods and the iodine recovery process from the AC/PVA matrix were set. The Limit of Quantification (LOQ) for iodine analysis was $3 \cdot 10^{-8}$ moles of I^-.

In contrast to the previous deposition tests, the beam current was continuously monitored on the activated carbon substrate (FC3) during the test. Carbon is, indeed, a conductive material so the substrate was used as a homemade FC. The home-made FC had no suppression electrode, so a correcting factor for the count of the exact iodine current had to be applied. The AC/PVA substrate turned out to register 12.9% more current than the suppressed FC. This was kept under consideration for the following calculations.

Three deposition tests for iodine were carried out; the beam trend for the first test is outlined in figure 3.11 and data reported in table 3.5. The number of atoms loaded in the MM was calculated on the ground of iodine ionization efficiency, which was calculated and was ~19%, and the detection limit of the analytical technique, in order to be able to quantify iodine after extraction form the AC/PVA disc. The number of iodine atoms reaching the AC/PVA target was calculated from the integration of the FC3 signal over time, applying the aforementioned suppression correction. Following extraction, iodine was titrated and the final quantification and efficiency data are reported in table 3.5. After the first two depositions we could titrate $2.16 \cdot 10^{16}$ and $1.7 \cdot 10^{16}$ atoms of iodine, which are 22.7 and 17.2% of the total number of iodine atoms impinging the AC/PVA target. In the third deposition, we measured $1.2 \cdot 10^{17}$ atoms of iodine, 63.7% of the atoms impinging the target.

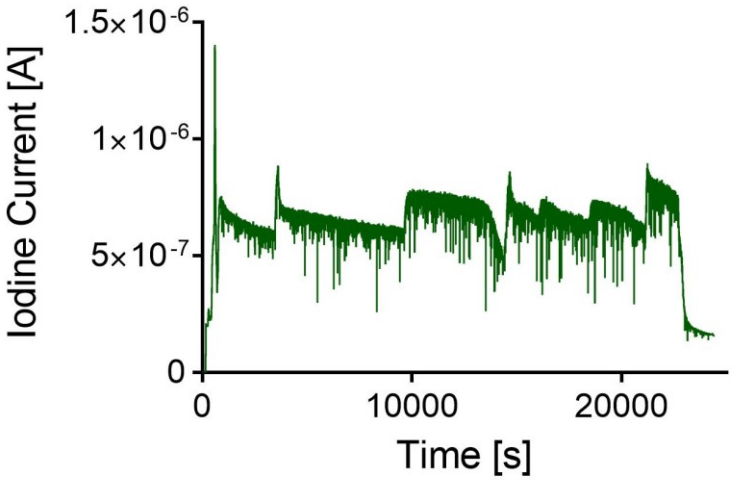

Figure 3.11. Iodine currents during deposition test on the AC/PVA matrix. Large fluctuations are due to the fact that the signal read on the substrate is unstable, because there is no electron suppression electrode.

Table 3.5. Results of iodine depositions tests.NMM is the number of iodine atoms loaded on the MM; N_t is the number of iodine ions impinging on the AC/PVA target, calculated from integration of the current. The third column reports the number of iodine atoms measured the titration.

Test	Integrated charge [C]	Iodine atoms impinging the target [N]	Iodine atoms extracted from the target	Chemical recovery from the target
1	$5.5 \cdot 10^{17}$	$9.4 \cdot 10^{16}$	$2.1 \cdot 10^{16}$	22.7 %
2	$5.5 \cdot 10^{17}$	$9.9 \cdot 10^{16}$	$1.7 \cdot 10^{16}$	17.2 %
3	$7.5 \cdot 10^{17}$	$1.9 \cdot 10^{17}$	$1.2 \cdot 10^{17}$	63.7 %

3.3.5 Copper ionization

Copper was ionized for the first time using the SPES PIS. It was introduced in the FE by means of the MM technique, so ionization occurred after the oven was heated up, using currents of ~30 A up to 80 A. Several mass scans were performed to prove copper ionization using the WF.

A typical mass scan for copper is reported in figure 3.12A. Copper is clearly identified thanks to the two peaks of masses 63 and 65. The isotopic abundance ratio was checked by the comparison of the peaks heights, which gave a value of 68.7/31.3, very close to expected values of 69.1/30.8.

The ionization efficiency was calculated repeating the assay every time with a new MM until all the copper was evaporated and no more copper current could be detected. The time necessary was around 4 hours keeping the Cu^{+} current at about 200 nA, giving an efficiency of about10%. In figure 3.12B we report the copper beam current trend.

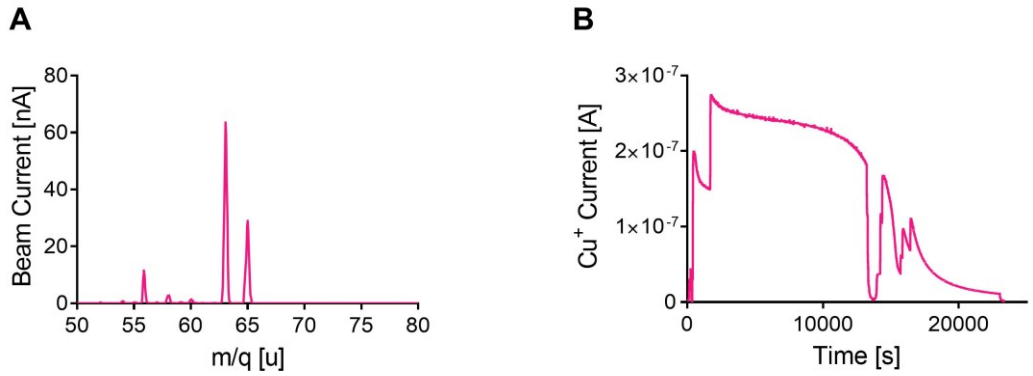

Figure 3.12. (A) Mass scan of copper beams and (B) trend of copper beam in time during ionization tests.

3.3.6 Copper beams deposition and copper analysis

All the targets irradiated during the copper depositions, resulted in clear brownish spots of the beam. The first 2 depositions, carried out with the FE at the upgrade level of July 2017, had a spot like that reported in figure 3.13A, while the latest, performed in September 2017 had a smaller spot (figure 3.13B).

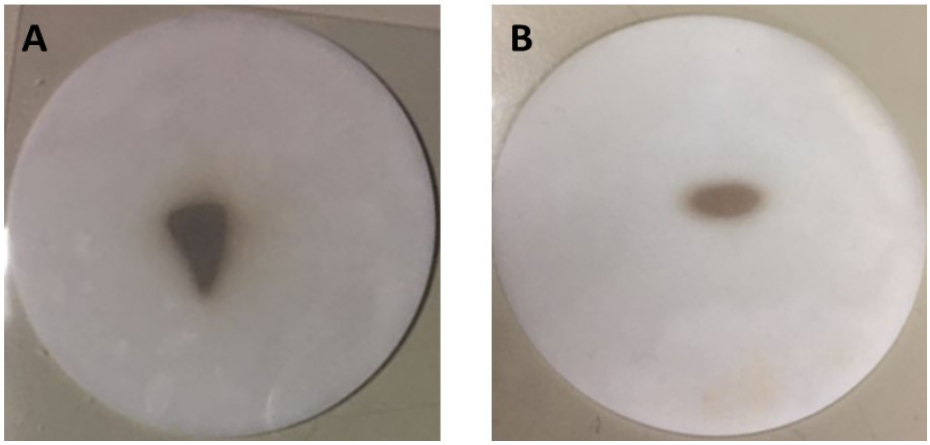

Fiugre 3.13. The copper beam spots on the sodium chloride discs after the July deposition tests (A) and September (B).

The quantities of expected copper on the substrate, calculated thanks to the integration of the beam current in time, and the real detected ones are reported in table 3.6. The first two depositions were carried out for a longer time period and at higher heating currents, for this reason the expected copper was 9.94 and 5.21 μg, while the measured ones, after dissolution in HNO_3 0.5 M, were 1.46 and 1.09 μg, respectively. During depositions 3 and 4, 1.12 and 0.94 μg was deposed, while the measured ones were 0.54 and 0.50 mg, respectively.

Table 3.6. Results of copper deposition.

	Copper (current) measured in FC2 and integrated in time [μg]	**Copper measured via GF-AAS [μg]**	
1st deposition	9.94	1.46	Target dissolved in HNO_3 0.5 M, mild heating
2nd deposition	5.21	1.09	Target dissolved in HNO_3 0.5 M, mild heating
3rd deposition	1.12	0.54	Target dissolved in concentrated HNO_3, 180 °C for 20 min
4th deposition	0.94	0.50	Target dissolved in concentrated HNO_3, 180 °C for 20 min

3.4 Discussion

To test the possibility of using RIBs produced at the SPES facility in Legnaro for radionuclides production, the SPES test bench, named Front End, was used in off-line mode and tests were performed by means of the Mass Marker technique. It was possible to produce iodine and copper ion beams with good ionization efficiencies > 19% and ~10%, respectively. It was also possible to ionize and detect yttrium ions, but the ionization efficiency for yttrium was very low.

The ionization of yttrium was greatly affected by its poor volatility (3300 °C atmospheric pressure, 1500 °C 10^{-6} mbar [3.24]). To observe appreciable yttrium currents (> 10 nA) the quantity of yttrium solution loaded on the MM had to be increased (900 μL), and the MM was not placed inside the oven, but directly into the transfer line of the ion source to facilitate the evaporation. Also the yttrium salt seemed to have an influence on the ionization, the use of YCl_3 was, indeed, more effective than $Y(NO_3)_3$. We hypothesized the possible formation of yttrium oxide, a highly refractory material, when using the nitrate, after heating. The presence of a fine white powder on the MM after the ionization test was considered another evidence of the occurrence of this phenomenon.

Although yttrium currents, and consequently yttrium quantities, were very low (~100 ng), thanks to a very sensible analytical method, yttrium could be detected after implantation on the secondary target. The recovery of yttrium from the secondary targets were high (100 and 53%). The results of the ionization of yttrium are not encouraging if one considers the possible production of ^{90}Y with the ISOL method. Nevertheless, ^{90}Y remains one the radionuclides considered for the production within the ISOLPHARM project, because ^{90}Sr, the mother radionuclide of ^{90}Y is also produced inside UC_x target and can be ionized and recovered more efficiently using the SPES Surface Ion Source [3.15,3.1,3.6]. For this reason, we can consider its production via a very pure ^{90}Sr/^{90}Y generator.

Iodine on the contrary is highly volatile, for this reason the MM was placed inside the oven. The ionization efficiency was good (>19%) and high currents could be detected at low oven temperatures (~10 A). The biggest problem for iodine was related to its chemical recovery from the AC/PVA secondary target. The first two depositions discs, indeed, were treated without heating, and this way the recovery efficiency was low (~20%). A great improvement (>60%) was possible for the third deposition target, that was heated up to 55 °C during iodine extraction.

The studies performed with copper are useful for the future production both of ^{64}Cu and ^{67}Cu with the ISOL method. The ionization efficiency was good (10%). In this case the recovery process was improved with the dissolution of the secondary target in concentrated nitric acid if compared to the use of 0.5 M HNO_3, 50% and 20%, respectively. The discrepancy between the expected copper deposition and the amount analysed via AAS (see table 3.6) can be due to the fact that the beam current was

measured from time to time during the deposition and fluctuation in the beam current are not detected, to losses during the beam transport, as the deposition target is quite far from the FC2, where the beam current for integration was read, or to a problem in the chemical dissolution.

3.5 Conclusions

In this chapter the experiments using the Front End, the test bench of the SPES project, were described. All three elements under test, yttrium, iodine and copper, could be ionized, collected on the secondary targets, and detected after dissolution, even if with difficult repeatability caused by instability of the FE. These results however represent a very positive starting point for the validation of the "ISOL" part of the ISOLPHARM project, making available secondary targets in which desired isotopes are collected.

Further improvements in the recovery processes of the collected atoms need to be developed, together with the consolidation of the experimental apparatus, in order to make the production and recovery of the radionuclides a reliable and reproducible process.

References

[3.1] F. Borgna, M. Ballan, S. Corradetti, E. Vettorato, A. Monetti, M. Rossignoli, M. Manzolaro, D. Scarpa, U. Mazzi, N. Realdon, A. Andrighetto, A preliminary study for the production of high specific activity radionuclides for nuclear medicine obtained with the isotope separation on line technique, Appl. Radiat. Isot. 127 (2017). doi:10.1016/j.apradiso.2017.06.022.

[3.2] T. Nilsson, European RIB facilities - Status and future, Nucl. Instruments Methods Phys. Res. Sect. B Beam Interact. with Mater. Atoms. 317 (2013) 194–200. doi:10.1016/j.nimb.2013.06.037.

[3.3] C. Müller, K. Zhernosekov, U. Koster, K. Johnston, H. Dorrer, A. Hohn, N.T. van der Walt, A. Turler, R. Schibli, A Unique Matched Quadruplet of Terbium Radioisotopes for PET and SPECT and for - and --Radionuclide Therapy: An *In Vivo* Proof-of-Concept Study with a New Receptor-Targeted Folate Derivative, J. Nucl. Med. 53 (2012) 1951–1959. doi:10.2967/jnumed.112.107540.

[3.4] C. Müller, E. Fischer, M. Behe, U. Köster, H. Dorrer, J. Reber, S. Haller, S. Cohrs, A. Blanc, J. Grünberg, M. Bunka, K. Zhernosekov, N. van der Meulen, K. Johnston, A. Türler, R. Schibli, Future prospects for SPECT imaging using the radiolanthanide terbium-155 - production and preclinical evaluation in tumor-bearing mice, Nucl. Med. Biol. 41 (2014) 58–65. doi:10.1016/j.nucmedbio.2013.11.002.

[3.5] V. Goffredo, A. Paradiso, G. Ranieri, C.D. Gadaleta, Yttrium-90 (^{90}Y) in the principal radionuclide therapies: An efficacy correlation between peptide receptor radionuclide therapy, radioimmunotherapy and transarterial radioembolization therapy. Ten years of experience (1999-2009), Crit. Rev. Oncol. Hematol. 80 (2011) 393–410. doi:10.1016/j.critrevonc.2011.01.012.

[3.6] A. Monetti, A. Andrighetto, C. Petrovich, M. Manzolaro, S. Corradetti, D. Scarpa, F. Rossetto, F. Martinez Dominguez, J. Vasquez, M. Rossignoli, M. Calderolla, R. Silingardi, A. Mozzi, F. Borgna, G. Vivian, E. Boratto, M. Ballan, G. Prete, G. Meneghetti, The RIB production target for the SPES project, Eur. Phys. J. A. 51 (2015). doi:10.1140/epja/i2015-15128-6.

[3.7] A. Andrighetto, S. Corradetti, M. Ballan, F. Borgna, M. Manzolaro, D. Scarpa, A. Monetti, M. Rossignoli, R. Silingardi, A. Mozzi, G. Vivian, E. Boratto, L. De

Ruvo, N. Sattin, G. Meneghetti, R. Oboe, M. Guerzoni, A. Margotti, M. Ferrari, A. Zenoni, G. Prete, The SPES High Power ISOL production target, Nuovo Cim. Della Soc. Ital. Di Fis. C. 38 (2015). doi:10.1393/ncc/i2015-15194-x.

[3.8] S. Corradetti, L. Biasetto, M. Manzolaro, D. Scarpa, S. Carturan, A. Andrighetto, G. Prete, J. Vasquez, P. Zanonato, P. Colombo, C.U. Jost, D.W. Stracener, Neutron-rich isotope production using a uranium carbide - carbon Nanotubes SPES target prototype, Eur. Phys. J. A. 49 (2013) 56. doi:10.1140/epja/i2013-13056-1.

[3.9] C. Müller, N.P. van der Meulen, M. Benešová, R. Schibli, Therapeutic Radiometals Beyond ^{177} Lu and ^{90} Y: Production and Application of Promising α-Particle, β^--Particle, and Auger Electron Emitters, J. Nucl. Med. 58 (2017) 91S–96S. doi:10.2967/jnumed.116.186825.

[3.10] F. Shi, X. Zhang, K. Wu, F. Gao, Y. Ding, R. Maharjan, R. Zhang, F. Zhang, C. Li, Metastatic malignant melanoma: computed tomography-guided 125I seed implantation treatment., Melanoma Res. 24 (2014) 137–43. doi:10.1097/CMR.0000000000000028.

[3.11] G. Rodrigues, X. Yao, A.D. Loblaw, M. Brundage, J.L. Chin, Low-dose rate brachytherapy for patients with low- or intermediate-risk prostate cancer: a systematic review, Can. Urol. Assoc. J. 7 (2013) 463. doi:10.5489/cuaj.1482.

[3.12] O.E. Seidlin SM, Marinelli LD, Radioactive iodine therapy; effect on functioning metastases of adenocarcinoma of the thyroid, J. Am. Med. Assoc. 132 (1946) 838–847.

[3.13] A. Wyszomirska, Iodine-131 for therapy of thyroid diseases. Physical and biological basis., Nucl. Med. Rev. Cent. East. Eur. 15 (2012) 120–3. http://www.ncbi.nlm.nih.gov/pubmed/22936505.

[3.14] M. Manzolaro, A. Andrighetto, G. Meneghetti, A. Monetti, D. Scarpa, M. Rossignoli, J. Vasquez, S. Corradetti, M. Calderolla, G. Prete, Ongoing characterization of the forced electron beam induced arc discharge ion source for the selective production of exotic species facility, Rev. Sci. Instrum. 85 (2014) 2–4. doi:10.1063/1.4857175.

[3.15] M. Manzolaro, A. Andrighetto, G. Meneghetti, M. Rossignoli, S. Corradetti, L. Biasetto, D. Scarpa, A. Monetti, S. Carturan, G. Maggioni, Ionization efficiency estimations for the SPES surface ion source, Nucl. Instruments Methods Phys.

Res. Sect. B Beam Interact. with Mater. Atoms. 317 (2013) 446–449. doi:10.1016/j.nimb.2013.07.045.

[3.16] M. Manzolaro, G. Meneghetti, A. Andrighetto, G. Vivian, F. D'Agostini, Thermal-electric coupled-field finite element modeling and experimental testing of high-temperature ion sources for the production of radioactive ion beams, Rev. Sci. Instrum. 87 (2016) 2–5. doi:10.1063/1.4933081.

[3.17] B. Wolf, The Handbook of Ion Sources, 1995.

[3.18] J.S. Al-Khalili, E. Roeckl, eds., The Euroschool Lectures on Physics with Exotic Beams, Vol. III, Springer Berlin Heidelberg, Berlin, Heidelberg, 2009. doi:10.1007/978-3-540-85839-3.

[3.19] W. Wien, Verhandlungen Physik. Gesellsch, Berlin, 1897.

[3.20] F. Schwellnus, R. Catherall, B. Crepieux, V.N. Fedosseev, B.A. Marsh, C. Mattolat, M. Menna, F.K. Österdahl, S. Raeder, T. Stora, K. Wendt, Study of low work function materials for hot cavity resonance ionization laser ion sources, Nucl. Instruments Methods Phys. Res. Sect. B Beam Interact. with Mater. Atoms. 267 (2009) 1856–1861. doi:10.1016/j.nimb.2009.02.068.

[3.21] B. Crepieux, Préparation et domaine d'exploitation des Mass-Marker des cibles ISOLDE, Intern. Report, Cern. (2006).

[3.22] M. Manzolaro, G. Meneghetti, A. Andrighetto, Thermal-electric numerical simulation of a surface ion source for the production of radioactive ion beams, Nucl. Instruments Methods Phys. Res. Sect. A Accel. Spectrometers, Detect. Assoc. Equip. 623 (2010) 1061–1069. doi:10.1016/j.nima.2010.08.087.

[3.23] V. Di Noto, D. Ni, L.D. Via, F. Scomazzon, M. Vidali, Determination of platinum in human blood using inductively coupled plasma atomic emission spectrometry with an ultrasonic nebulizer, Analyst. 120 (1995) 1669. doi:10.1039/an9952001669.

[3.24] Honig RE, Radio Corporation of America Vapor Pressure Data for the Solid and Liquid Elements, RCA Rev. 23 (1962) 567–586.

Chapter 4

Chemical purification from isobaric contaminants

4.1 Introduction

In this chapter the purification method developed for the separation of Sr^{2+} and Y^{3+} is described. As previously discussed, the isotopic contaminants of the radionuclides can be purified thanks to the ISOL technique by means of mass separation [4.1,4.2]. However, not only the isotopic contaminants can decrease the quality of a radionuclide, also isobaric and pseudo-isobaric contaminants can affect the purity of the final radiopharmaceutical precursors. This is true when long-lived radioisotopes of the same mass are produced inside the primary target and have a sufficiently low boiling temperature, so they can escape from the target together with the radionuclide of interest [4.2].

^{89}Sr is a radionuclide used in the clinics as a chloride ($SrCl_2$) for painful bone metastases secondary to prostate cancer [4.3]. It is one of the radioisotopes which can be produced thanks to uranium fission inside the SPES UC_x target [4.2]. For this reason its production with ISOL method was previously studied [4.2]. Uranium-fission products of mass 89 are neutron-rich radionuclides which quickly decays to ^{89}Sr. For this reason, after waiting for a short time all the parents radionuclides of mass 89 cannot be found in the secondary target and no purification method has to be developed to remove radionuclidic contaminants [4.2]. The only element of mass 89 that will be present in the secondary target is yttrium, which is also strontium-89 daughter. Nevertheless, the presence of this stable contaminant (^{89}Y) was considered as relevant for further ^{89}Sr radiopharmaceutical developments, which do not foresee the use of strontium in the form of a chloride, but bound to a chelator. The big advantage of the ISOL method for ^{89}Sr is the possibility of producing this radionuclide as carrier-free. In this work a method to purify strontium from yttrium was developed.

An ion exchanger inorganic material, sodium nonatitanate, previously developed for nuclear aqueous waste management thanks to its ability to trap strontium [4.5,4.6], was synthetized and used for this purpose. Since this material had been described in a patent of Sylvester [4.7] for its potential use as a resin for a $^{90}Sr/^{90}Y$ generator, the synthetized resin was also tested for the purification of ^{90}Y from ^{90}Sr and to develop a generator for $^{90}Sr/^{90}Y$ loading ^{90}Sr produced with the ISOL technique.

Sodium nonatitanate ($Na_4Ti_9O_{20}\cdot xH_2O$), abbreviated as NaTi, structure in figure 4.1, was chosen for its very high selectivity and affinity for strontium [4.6,4.8,4.9]. Moreover, it is an inorganic material and this guarantees a higher resistance to radiations compared to organic resins [4.10].

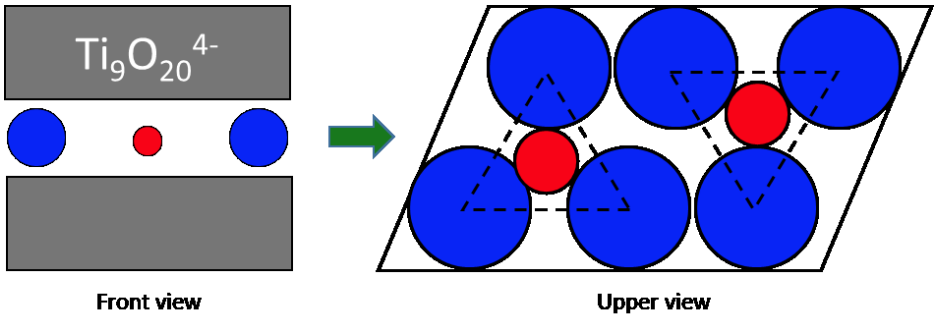

Figure 4.1. Sodium nonatitanate's geometry [9]. Red spheres are sodium atoms, blue ones are water molecules.

The synthesis was performed with a hydrothermal method according to previously published procedures [4.6,4.11,4.12]. Hydrothermal methodology is characterized by a heterogeneous reaction where the solvent, in our case water, at high temperature and pressure can dissolve and then recrystallize the starting and target compounds that would not be soluble under standard conditions [4.13,4.14]. Hydrothermal synthesis can be carried out in two different conditions: supercritical and subcritical. In the first case the synthesis is performed above the critical point (T_c=374.1 °C and P_c=22.1 MPa for water) and no phase separation between liquid and vapor can be distinguished. On the other hand, in subcritical conditions, and above the boiling point of the solvent, the solvent and its vapor can coexist in the reaction chamber. The volume occupied by the solvent must be in case of water >32% of the total vessel volume. Key feature of the system is the fact that it is a closed system: this way the increase in temperature results in the rise of pressure. Autoclaves, where temperature and pressure can be controlled individually, and "bombs" are systems that can be used for hydrothermal synthesis. The latter is the one used for the synthesis of NaTi here reported. A picture of the used bomb

and a scheme of it are shown in figure 4.2. Teflon vessel (Volume = 23 mL), where the reaction mixture is prepared, is closed inside the metallic container that guarantees the safety of the system when the pressure inside increases.

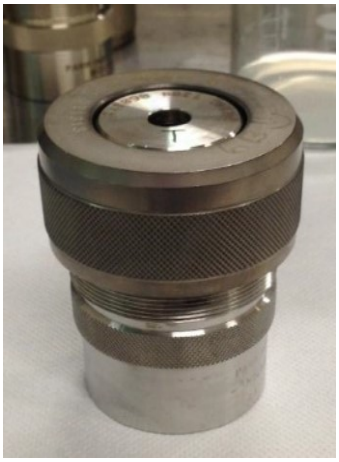

Figure 4.2. Hydrothermal vessel used for the synthesis.

The increase in temperature of the system turns out in the change of some of the solvent characteristics, such as viscosity, dielectric constant and density. The crystallization process is the step necessary to pass from particle suspension to crystalline powder. This happens through nucleation, aggregation and particle growth [4.13,4.14].

In the case of sodium nonatitanate the synthesis was carried out at the limit temperature of 175 °C, in order to have a semi crystalline structure, ideal for strontium trapping. As described by Merceille [4.12] the semi crystalline NaTi has the correct distance between its layers. Its structure is not yet fully understood, but it is assumed to be composed of TiO_6 octahedral chains linked into layers with exchangeable Na^+ cations in between [4.12]. The uptake of strontium occurs after the exchange with two Na^+ ions.

In this work NaTi was synthetized at different temperatures 100, 150 and 175 °C, characterized and used for strontium and yttrium purifications. The best conditions for the purification were studied and experiments with cold strontium and yttrium were carried out in order to assess a simple and fast method for ISOL ^{89}Sr and $^{90}Sr/^{90}Y$.

For these tests analytical methods for strontium and yttrium were used. For the first one atomic absorption spectroscopy with graphite furnace atomizer was used (GF-AAS) adjusting the samples matrix with the addition of HNO_3 to maximize the signal [4.15]. Yttrium was analyzed with a spectrophotometric technique using the complexant Arsenazo (III) [4.16,4.17].

4.2 Materials and Methods

4.2.1 Materials

All the reagents were purchased from Sigma Aldrich: sodium hydroxide (≥98%, pellets), titanium isopropoxide (≥97%), strontium nitrate (Standard for AAS, TraceCERT® 1000 mg/L in nitric acid), yttrium nitrate (Standard for ICP, TraceCERT® 1000 mg/L in nitric acid), nitric acid (≥69%, TraceSELECT®), hydrochloric acid (≥37%, TraceSELECT®), sodium nitrate (99.995% trace metal basis), sodium chloroacetate for synthesis (EMD Millipore), Arsenazo (III) (calcium-sensitive dye), sodium chloride (TraceSELECT).

4.2.2 Synthesis of Sodium Nonatitanate (NaTi)

Sodium nonatitanate (NaTi) was idrothermally synthetized according to a previously published procedure [4.6,4.11,4.12]. The reaction involved in the synthesis was (4.1):

$$9Ti(OC_3H_7)_4 + 4NaOH \rightarrow Na_4Ti_9O_6 \cdot xH_2O \quad (4.1).$$

Around 2.5 g of titanium isopropoxide were quickly added to 2.8 g of a solution of NaOH (50% w/w in water) previously prepared in a teflon vessel (internal volume 23 mL). After stirring, 2 mL of deionized water was added to the mixture and the vessel was closed inside the synthesis bomb. The bomb was then heated up inside an oven at 100, 150 and 175 °C for 21 hours. After removing the bomb from the oven, it was cooled down and opened. The synthetized NaTi was carefully washed with deionized water and dried at 50 °C overnight. After drying, the powder was ground and sieved. The powder with a particle size >40 μM was used for the tests.

4.2.3 NaTi characterization

After the synthesis, NaTi100, NaTi150 and NaTi175 were characterized using different techniques: X-ray Powder Diffraction (XRD), physisorption analysis and Scanning Electron Microscopy (SEM). For XRD analysis the D8 Advance (Bruker®) diffract meter was used (θ = 5-60°, λ (Cu Kα) = 0.1542 nm); this analysis was useful to determine the identity of the material and to verify its degree of crystallinity. The interlayer distance was also calculated with the Bragg's law [4.18], see equation 4.2:

$$2d \cdot sin\vartheta = n\lambda \quad (4.2),$$

where *d* is the distance between the layers, θ is the reflection angle, *n* is a positive number and λ is characteristic of the incident ray. The data were analyzed using Match! software and compared with the literature [4.6,4.8,4.9]. To verify how the difference in the synthesis temperature could affect the porosity of the material, the physisorption analysis was carried out using ASAP 2020 Plus (Micrometrics ®). The powder underwent a degassing step of 10 h before analysis at the same temperature of the synthesis (100, 150 and 175 °C for NaTi100, NaTi150 and NaTi175, respectively). The BET method was used for Surface Area determination. Powder morphologies were determined with Vega 3xmh (Tescan) scanning electron microscope.

4.2.4 Yttrium quantification method

For yttrium quantification an analytical method via UV-Vis spectroscopy was developed. Arsenazo(III) is a bis-azo derivative of chromotropic acid [4.17], see figure 4.3, and was used in this study for to its ability of forming colored complexes with metal ions. Moreover, this reagent allowed selectivity for yttrium analysis even in the presence of other metal ions, by adjusting the solution pH [4.16]. For this reason, based on previous studies [4.16], the pH was always adjusted to pH 2.1 thanks to the addition of the buffer sodium chloroacetate. The Y(III)-Arsenazo (III) complex formed had a violet color [4.16], (figure 4.11).

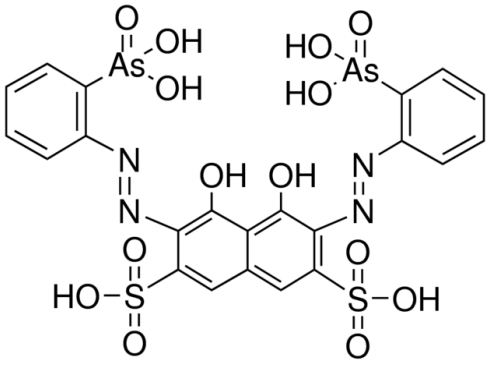

Figure 4.3. Az(III) structure.

The range of linearity of the method and its reproducibility were tested. The following procedure was used for yttrium quantification: 5 mL of the solution to be tested were buffered at pH 2.1 with the addition of sodium chloroacetate (0.1456 g) and of diluted (1:10) metal free HNO_3. This solution was then quantitatively transferred to a 25 mL flask and 2.5 mL of Az(III) 0.04% were added; to reach the final volume of 25 mL mQ

water was added to the flask. The solution was analyzed using a UV-Vis Cary 50 spectrophotometer (Varian ®), recording the spectrum in the UV-visible region from 800 nm to 250 nm. The absorbance for the calibration curve and sample analysis was measured at λ_{max}=654 nm. The baseline for background subtraction was prepared the same way as the samples, but without the addition of yttrium. Solutions of yttrium between 200 and 800 μg/L were prepared for the calibration curve. Depending on the sample matrix, different calibration curves were prepared.

The possible interference of strontium in solution [4.19] was verified analyzing a solution containing a high concentration of strontium (10 mg/L in a total volume of 5 mL) and treating the sample as for the analysis of yttrium. The pH was taken to 2.1 with sodium chloroacetate (0.1456 g) and diluted metal free HNO_3. 2.5 mL of Az(III) 0.04% were added to the solution after transferring it to a 25 mL flask and diluted with mQ water to the final volume and the absorbance measured at λ=654 nm. The same experiment was carried out at a slightly higher pH (3.1) treating the sample equally.

4.2.5 Strontium uptake in the resin depending on the synthesis temperature

The difference in the capabilities of NaTi100, NaTi150 and NaTi175 in up taking Sr^{2+} was tested. Around 50 mg of NaTi were slurried into a 50 mL test tube, together with 200 μg of $Sr(NO_3)_2$ in $NaOH/NaNO_3$ 0.05 M in a final volume of 5 mL. The test tube was gently mixed for 5 minutes and finally filtered on paper. The eluted solution was diluted with metal free HNO_3 in order to have an acidic concentration equal to 0.3 M, ideal for the analysis. The solutions were then analyzed with Graphite Furnace - Atomic Absorption Spectroscopy (GF-AAS, Varian®) to determine strontium concentration. A standard at the concentration of 100 μg/L in HNO_3 0.3 M was prepared for the calibration curve.

The uptake of strontium was tested also with a higher sodium chloride concentration. In particular, 0.3 M NaCl was used, because these are the conditions expected after dissolution of a 13 mm-diameter NaCl secondary target (see chapter 2).

4.2.6 Yttrium behavior at basic, neutral and acidic pH

NaTi was described as a selective ion exchanger for strontium [4.9]. Anyway other phenomena such as ions hydrolysis can lead to the loss in the resin selectivity. This was the case of yttrium, that at not-acidic pH forms colloids, which stick in the resin. The behavior of NaTi and yttrium was investigated at different pH values, from basic to acidic ones.

The experiments described in this and in the following paragraphs were carried out with a 2 mL plastic syringe, serving as a column, equipped with a polyethylene filter (pore size 20 μM). 10 mg of NaTi150 (grain size >40 μm) were loaded in the column and the powder wet with mQ water to remove the fines.

In the first experiments strontium and yttrium (40 μg of Sr^{2+} and 20 μg Y^{3+}) were loaded on the resin in a solution of NaOH 0.05M/$NaNO_3$ 0.05 M. The fractions recovered were analyzed to monitor the behavior of yttrium at basic pH.

After these tests, solutions containing 20 μg of yttrium in a total volume of 5 mL at pH values ranging from 1 to 7.5 (1.15, 2.20, 3.22, 4.06, 5.08, 6.09, 7.15 and 7.48) were passed through a column, where 10 mg of NaTi had been loaded. The pHs were obtained with sodium acetate 0.1 M solutions, buffered at the desired pH after the addition of few drops of HCl 0.1 M/NaCl 0.1 M. Before loading the solutions containing yttrium, the resin was wetted with solutions at the same pH of the corresponding yttrium solution, to buffer the resin. The pH of each solution was measured before and after the NaTi. The eluted solutions were analyzed to quantify yttrium.

In order to eliminate the precipitation of yttrium, which was identified as the responsible for yttrium uptake in the resin, a higher acetate concentration was used. Acetate could act as a counter ion for yttrium, able to prevent its hydrolysis. Acetate concentration was 0.3 M and the pH ~4.5. Two experimental set up were used: (i) 20 μg of yttrium were loaded on the resin (10 mg) in NaOH 0.05 M/$NaNO_3$ 0.05 M and then the resin was washed with 5 mL of the 0.3 M acetate solution, or (ii) yttrium (20 μg) was diluted in 5 mL of the acetate solution and passed through the resin (10 mg). The eluted solutions were analyzed to quantify yttrium.

Other strategies to prevent yttrium precipitation in the resin were used: first the washing of NaTi with ethanol prior to yttrium passage and afterwards diverse resin pre-

equilibrations with acidic solution. The used solutions were: HNO_3 0.1 M, HNO_3/CH_3COONa 0.1 M, $HNO_3/NaNO_3$ 0.1M. After washing 10 mg of NaTi with one of these solutions, 20 μg of yttrium in sodium acetate 0.1 M, pH ~6.5, were passed through NaTi and analyzed.

Additionally, the behavior of yttrium was tested after loading 20 μg of yttrium at basic pH by NaOH 0.05 M/$NaNO_3$ 0.05 M, and washing the resin with acidic solutions of diluted mineral acids (HCl or HNO_3) at pH values ranging from 0 to 4. Finally, the release of yttrium from the resin was tested in a solution of diluted nitric acid (0.1 M) with the addition of 0.1 M $NaNO_3$.

4.2.7 Strontium behavior at acidic pH

The affinity of NaTi for strontium depends strongly on the pH of the solution [4.6]. That is why for the sorption experiments, where the efficiency of trapping Sr^{2+} was evaluated, Sr^{2+} was always prepared in a sodium hydroxide solution. After studying the behavior of strontium at basic pH, it was studied at acidic ones. In particular strontium was trapped in the NaTi (40 μg of Sr^{2+} in NaOH 0.05 M and $NaNO_3$ 0.05 M), and then treated with acidic solutions. The resin was washed twice with 5 mL of HNO_3 or HCl 0.05, 0.1, 0.5 or 1 M and with HNO_3 0.1 M at increasing Na^+ concentrations (0.1, 0.2, 0.5 or 1 M). The release was also studied at slightly higher pH values, up to pH 4, with diluted HCl solutions. All the solutions were analyzed for yttrium quantification.

4.2.8 Purification of strontium from yttrium

Based on the results of NaTi behavior with strontium and yttrium at the different pH values and sodium concentrations, the following scheme, figure 4.4, for ^{89}Sr purification from the stable yttrium contaminant was hypothesized.

The developed procedure was divided into three steps: (1) loading of a solution containing Sr^{2+} and Y^{3+} (40 and 20 μg in 5 mL, respectively) in NaOH 0.05 M and NaCl 0.30 M; (2) elution with HCl 0.01 M and finally (3) the regeneration of the resin with 5 mL HNO_3 and $NaNO_3$ both 0.1 M. All the procedure was in a 2 mL plastic column, equipped with a polyethylene filter (PE) (20 μm pore size), where 10 mg of NaTi (> 40 μm) were loaded and wetted with water. Prior to the addition of solution 1, the resin was preconditioned with 5 mL of NaOH 0.05 M/NaCl 0.30 M.

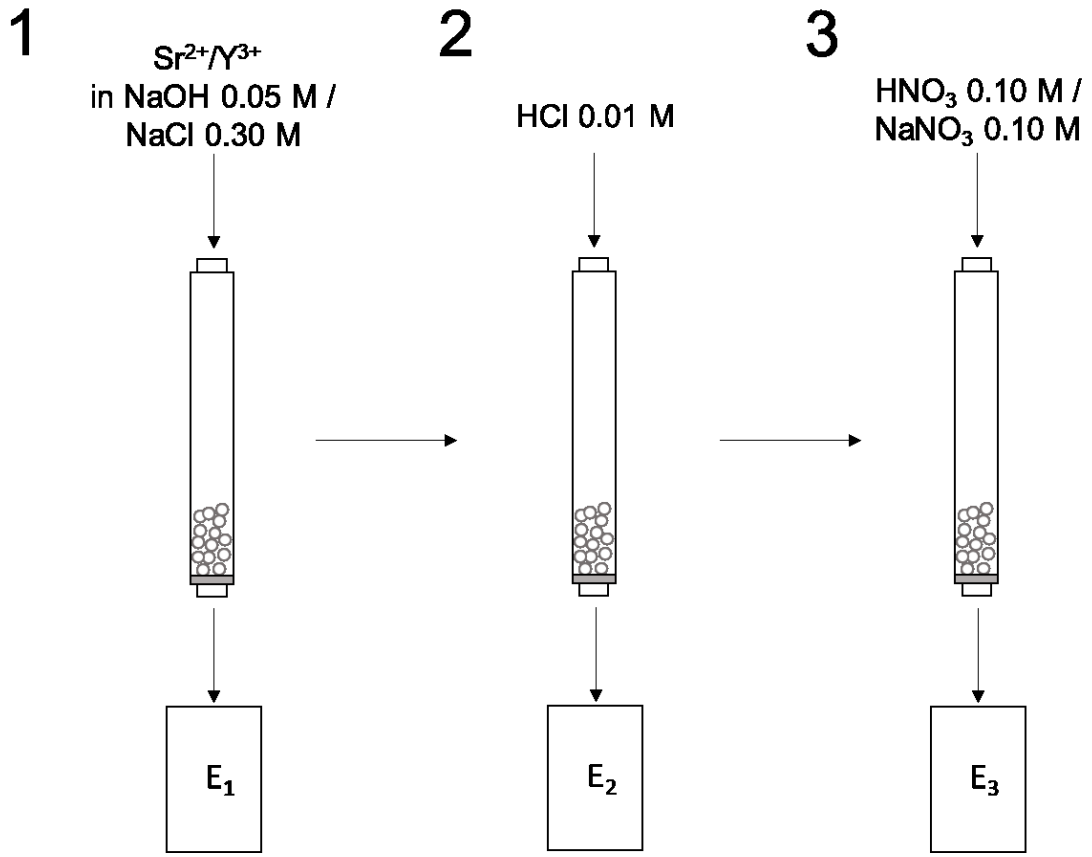

Figure 4.4. Scheme for strontium purification.

4.2.9 Purification of yttrium from strontium: a possible generator for ^{90}Y with NaTi

A purification scheme was developed for mass 90 purification, in particular for ^{90}Y decayed from ^{90}Sr, figure 4.5. ~10 mg of NaTi (>40 μm) were loaded into a 2 mL-plastic column, with one PE filter (20 μm pore size). In the first step strontium and yttrium (40 and 20 μg in 5 mL, respectively) in NaOH 0.05 M and NaCl 0.30 M were loaded. Immediately after loading, an acidic solution (HNO_3 0.1 M) was passed through the column. The eluted solution was eventually loaded again in column 1 to minimize strontium loss. After the step 2 the column was conditioned with (*i*) a basic solution of $NaOH/NaNO_3$ 0.1 M (pH 12), or (*ii*) a neutral solution (pH 7) of sodium acetate or (*iii*) a slightly acidic solution (pH 4.5) of sodium acetate 0.1 M buffered with few drops of NaCl 0.1 M in diluted HCl. After 10-15 days, the time necessary for strontium to decay into yttrium, we eluted the grown yttrium with Na^+/HCl 0.10 M (passage 3).

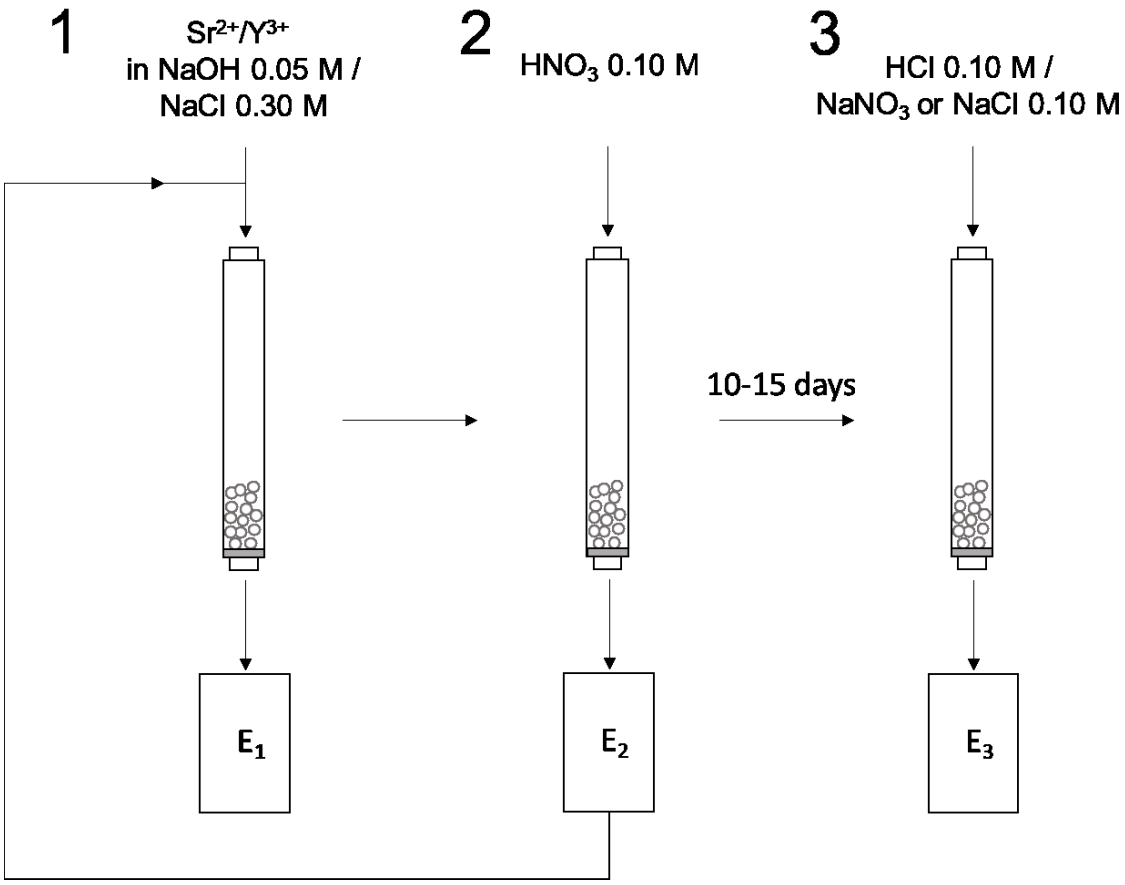

Figure 4.5. Scheme for yttrium purification

To simulate passage 3, a column was loaded with only yttrium (NaOH 0.05 M/NaCl 0.3M) and treated equally to the columns with strontium, but avoiding passage 2, in order to avoid the loss of yttrium. In these tests the elutions of yttrium were carried out without the addition of sodium (0.1 M), but in future this step will be carried out with the addition of sodium (see 4.14 (B)) to increase yttrium recovery.

4.3 Results

4.3.1 Synthesis of Sodium Nonatitanate

Three types of NaTis were created, depending on their synthesis temperature with good efficiencies (~1 g each bomb). XRD patterns, figure 4.6, of the compounds showed low crystallinity in all cases, with 4 main reflection peaks that are characteristic of pure NaTi; interlayer distances, calculated with Bragg's law, equation 4.1, are reported in table 4.1.

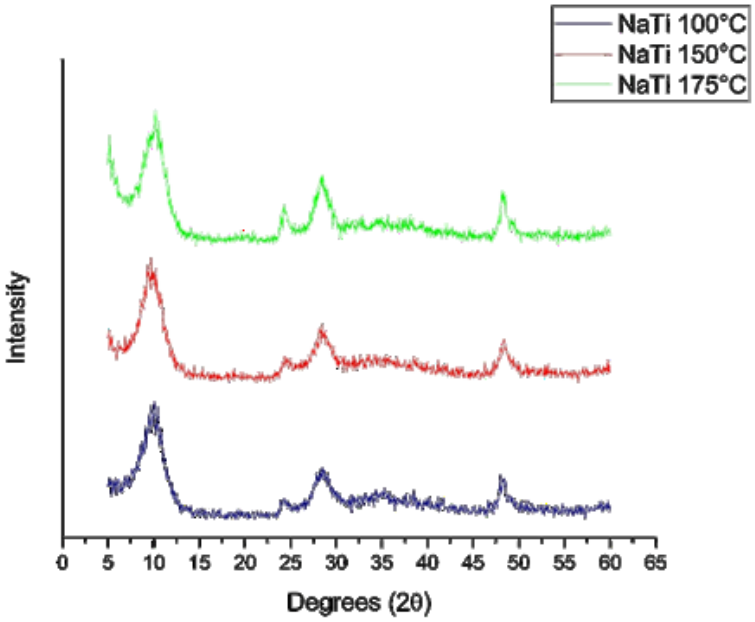

Figure 4.6. XRD patterns of synthetized NaTi: 100 °C blu line, 150 °C red line and 175 °C green line.

The interlayer distances of the three synthetized NaTis were 9.0, 9.1 and 8.7 A. These values were not considered as significantly different.

Table 4.1. Interlayer distances calculated with Bragg's law for NaTi synthetized at different temperatures.

Synthesis temperature [°C]	**First Reflection Peak [°]**	**Interlayer Distance [A]**
100	9.8	9.0
150	9.75	9.1
175	10.2	8.7

The obtainment of a semi crystalline material was regarded as ideal because it gives to NaTi the best configuration for Na^{+}/Sr^{2+} exchange. The semiamorphous nature was confirmed also by the SEM images. From these, indeed, a grain shape structure could be observed; crystalline NaTi instead is needle shaped [4.12]. In figure 4.7, NaTi SEM images are reported.

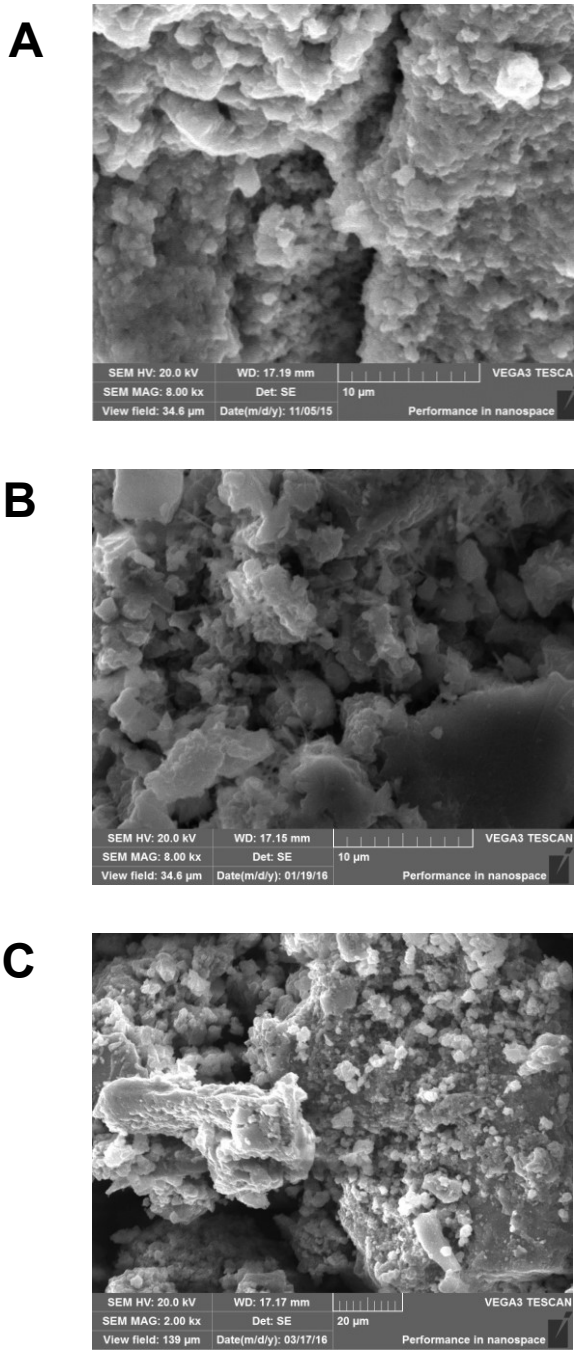

Figure 4.7. NaTi SEM images. In all the samples NaTi100 (A), NaTi150 (B) and NaTi175 (C), grains can be observed. No needle structure was present. The sharp surfaces that could be seen, especially in (B), were probably due to grain fragmentation. The image for the NaTi175 has different magnitude because a good resolution could not be obtained at 8.00 kx.

Synthesis temperature influenced greatly powder porosity, see the isotherm curves of the three NaTis, figure 4.8. The specific surface areas, calculated with BET method, of NaTi100, 150 and 175 were 4.2, 102 and 226 m^2/g, respectively.

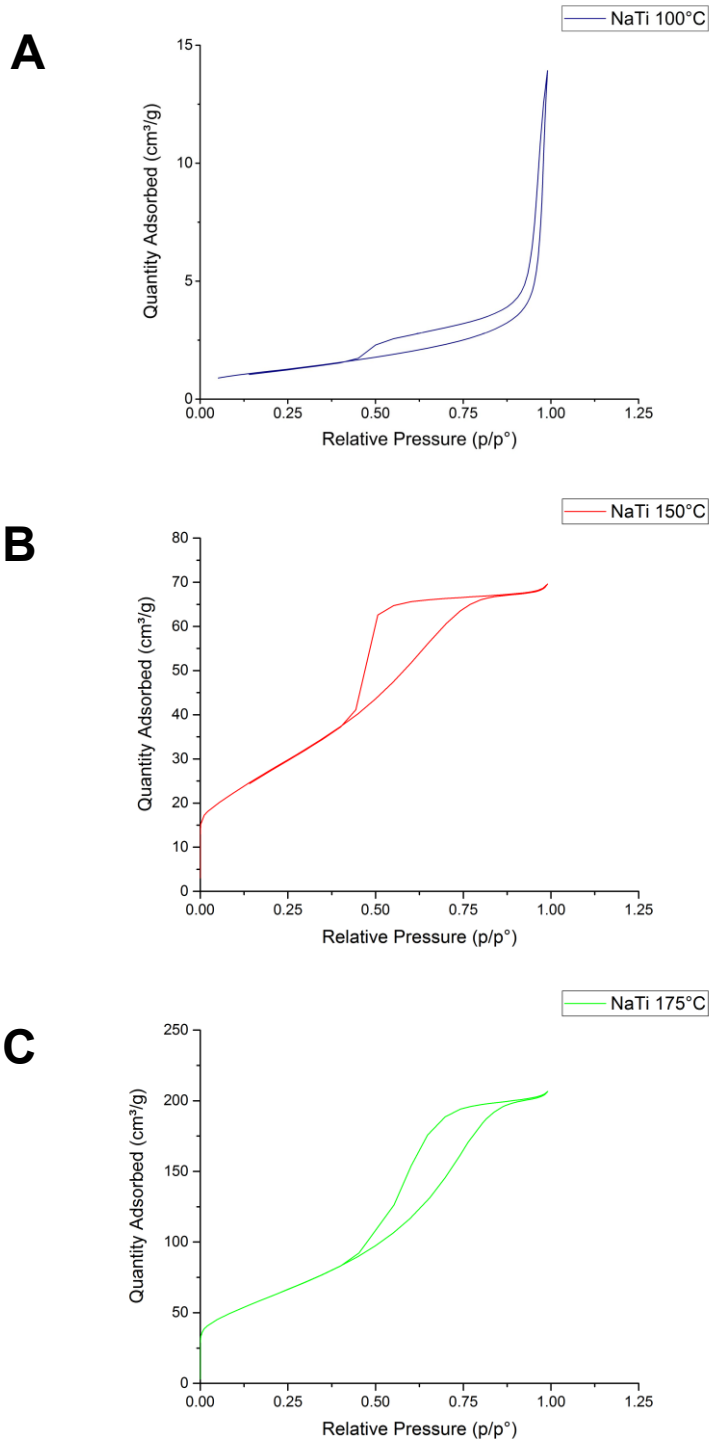

Figure 4.8. Isotherm curves obtained for NaTi samples. (A) is the curve of NaTi synthetized at 100 °C, no final saturation could be observed and small hysteresis was present. (B) and (C) are of NaTi synthetized respectively at 150 and 175 °C: they had very similar shape, with great absorption at small p/p^0 values and large hysteresis loops.

In figure 4.8 the isotherm obtained for each synthesis temperature are reported. NaTi 100 gave a curve of the III type with a H3 hysteresis loop, associated to slit-shaped

pores, according to IUPAC classification, see figure 2.5, chapter 2. NaTi 150 and NaTi175 had IV type curves with H2 hysteresis loops.

4.3.2 Yttrium quantification method

The developed quantification UV-Vis method allowed to quantify yttrium in a range between 300 and 800 µg/L, with the calibration curve method. Good linearity was checked by means of the calculation of the R^2 values. In figure 4.9 a typical spectrum of Az(III) without yttrium is presented. A broad characteristic peak could be observed at λ_{max}= 538 nm [4.17]. The UV-Vis spectrum registered for the solutions containing yttrium, figure 4.9 and 4.10 A, had two peaks at λ=605 and 654 nm.

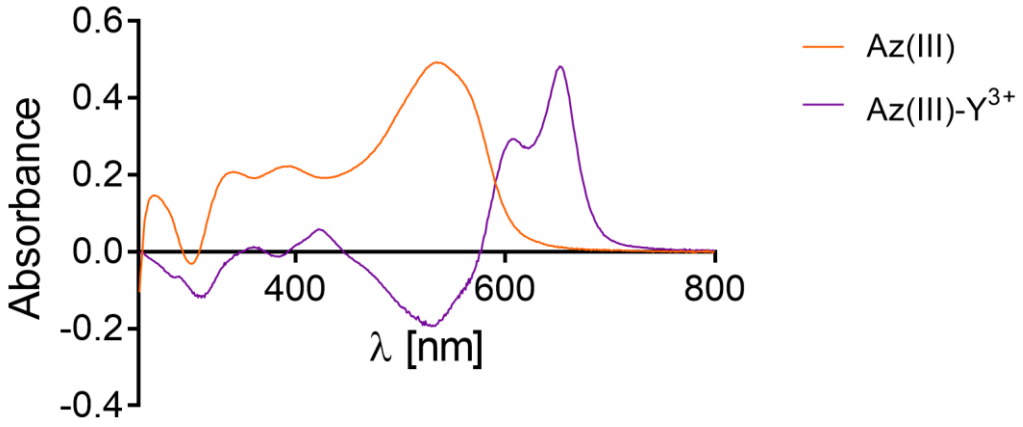

Figure 4.9. Example of a spectrum of a Az(III) solution, pH 2.31, orange line, and of a solution containing the complex Az(III)-Y^{3+}.

The measure of the absorbance values at 654 nm at different yttrium concentrations made possible to draw the linearity curve in figure 4.10 (B). The lowest concentration of yttrium that gave an absorbance value >0.1 was 300 µg/L. Good linearity was achieved with R^2 values > 0.99. Prior to every yttrium analysis, the calibration curve was prepared with freshly prepared standards, due to Az(III) complexes instability. The difference in yttrium concentrations could be qualitatively appreciated also with the human eye, see picture 4.11, thanks to the different violet intensities.

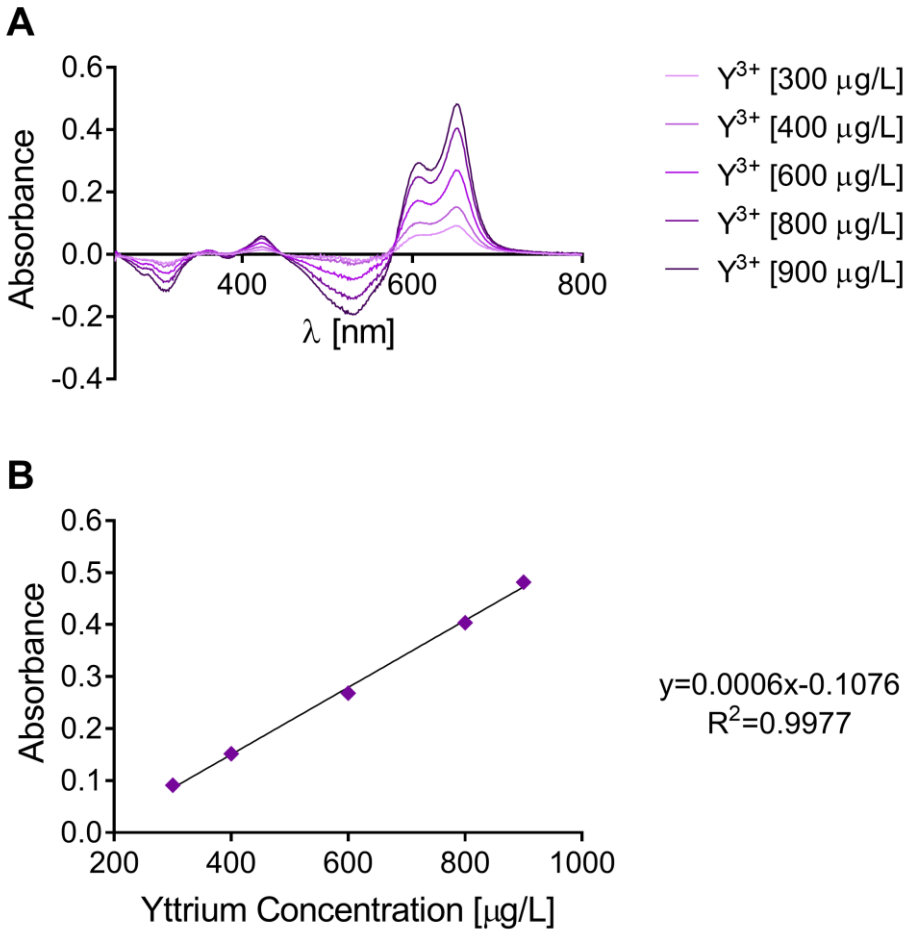

Figure 4.10. (A) UV spectra of Az(III)-Y complexes at increasing yttrium concentrations. (B) Calibration line for yttrium quantification.

When strontium was added to Az(III) at acidic pH (2.3 and 3.1), no Sr(II)-Az(III) was formed and no peak was visible, so it was concluded that the presence of strontium concomitant to yttrium did not influence yttrium analysis.

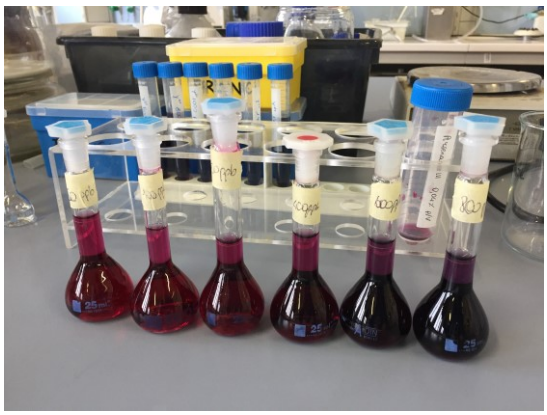

Figure 4.11. Yttrium samples, prior to UV analysis.

4.3.3 Strontium uptake in the resin

The three synthetized NaTi were tested for the strontium uptake capacities. The NaTi powder was grounded after synthesis and drying, because big grains were produced, figure 4.12 and 4.13.

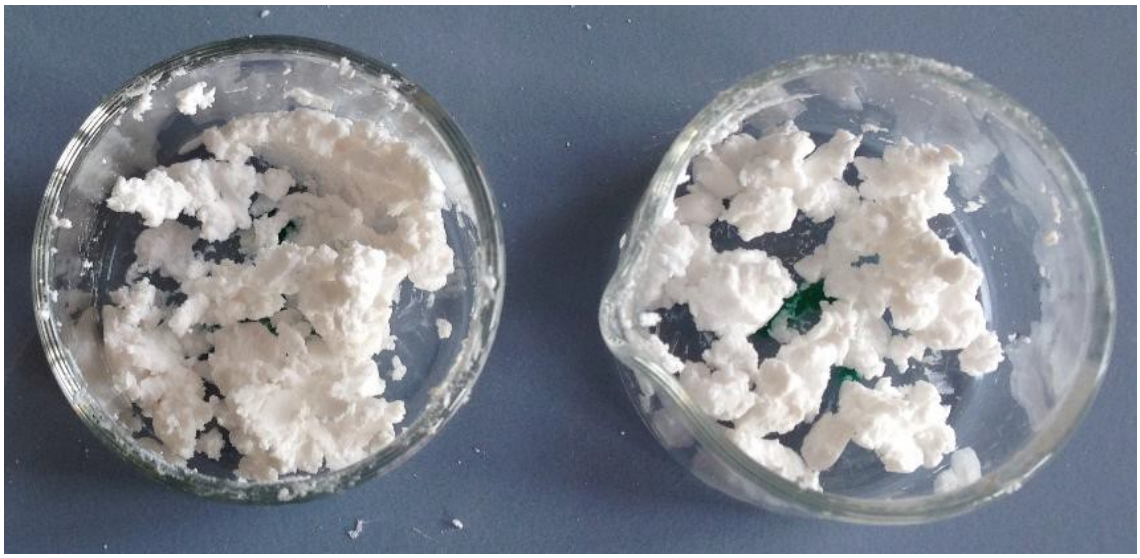

Figure 4.12. NaTi after synthesis, before drying.

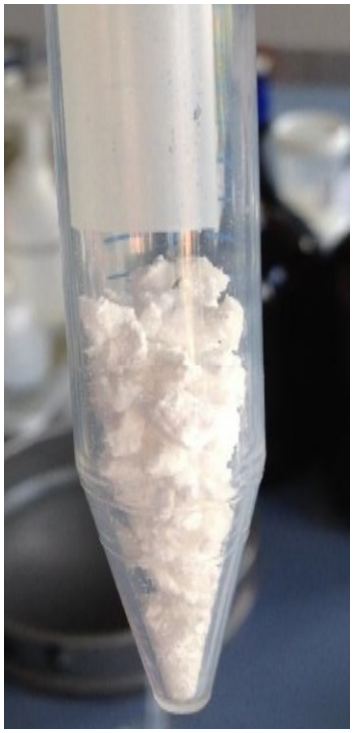

Figure 4.13. NaTi after drying.

To avoid the passage of the smallest particles through the filter in the column, the NaTi with a particle size > 40 μM was used. In all cases, Sr^{2+} uptake was very high (>99%),

proving a strontium up-take capacity >4 μg/mg of NaTi. No difference was observed when a sodium chloride concentration of 0.3 M was used for the uptake experiments.

4.3.4 Yttrium behavior at basic, neutral and acidic pH

After measuring the uptake efficiency of strontium in the resin, the behavior of yttrium was investigated. After passing the solution containing strontium and yttrium in the resin at basic pH, no yttrium could be detected in any conditions. For this reason, the behavior of yttrium at different pH was investigated. First yttrium was passed through the resin in solutions at pH values from 1 to 7. Prior to this step the resin was wetted with a solution at the same pH to prepare the environment. The pHs of these solutions were checked after the passage through the resin. No change in the pH was registered. In these preliminary results, we observed that only at acidic pH values, yttrium could be recovered. When the pH was > 4, the concentration of yttrium was below the quantification limit (300 μg/L). At pH 3, ~10 % of the yttrium which was passed through the resin could be measured, this quantity was higher at pH 2 ~58% and the entire amount of yttrium (100%) was recovered at pH=1.

All the strategies adopted to avoid yttrium precipitation, including the use of acetate at higher molarities (0.3 M) and the pre-washing step of the resin were not successful: yttrium in the eluted solutions was always below the quantification limit.

After these assays, it was decided to focus the attention on the behavior of both ions at acidic pH values, see figure 4.14 A.

At pH 4, we could detect 18.4 ±0.1% of the loaded yttrium, this value was stable also at pH 3, when 17.7 ±0.4% was measured. When the pH was 2 and 3, the recovered yttrium was 37.4 ±1.5% and 64.8 ±4.5%, respectively.

In figure 4.14 (B) a comparison was made between the % of yttrium released with and without the addition of $NaNO_3$ 0.1 M at pH 1 (HNO_3 0.1 M). When $NaNO_3$ was added to the exchange solution a higher release of yttrium was observed, 85.4 ±5.8% *vs* 64.8 ±4.5%.

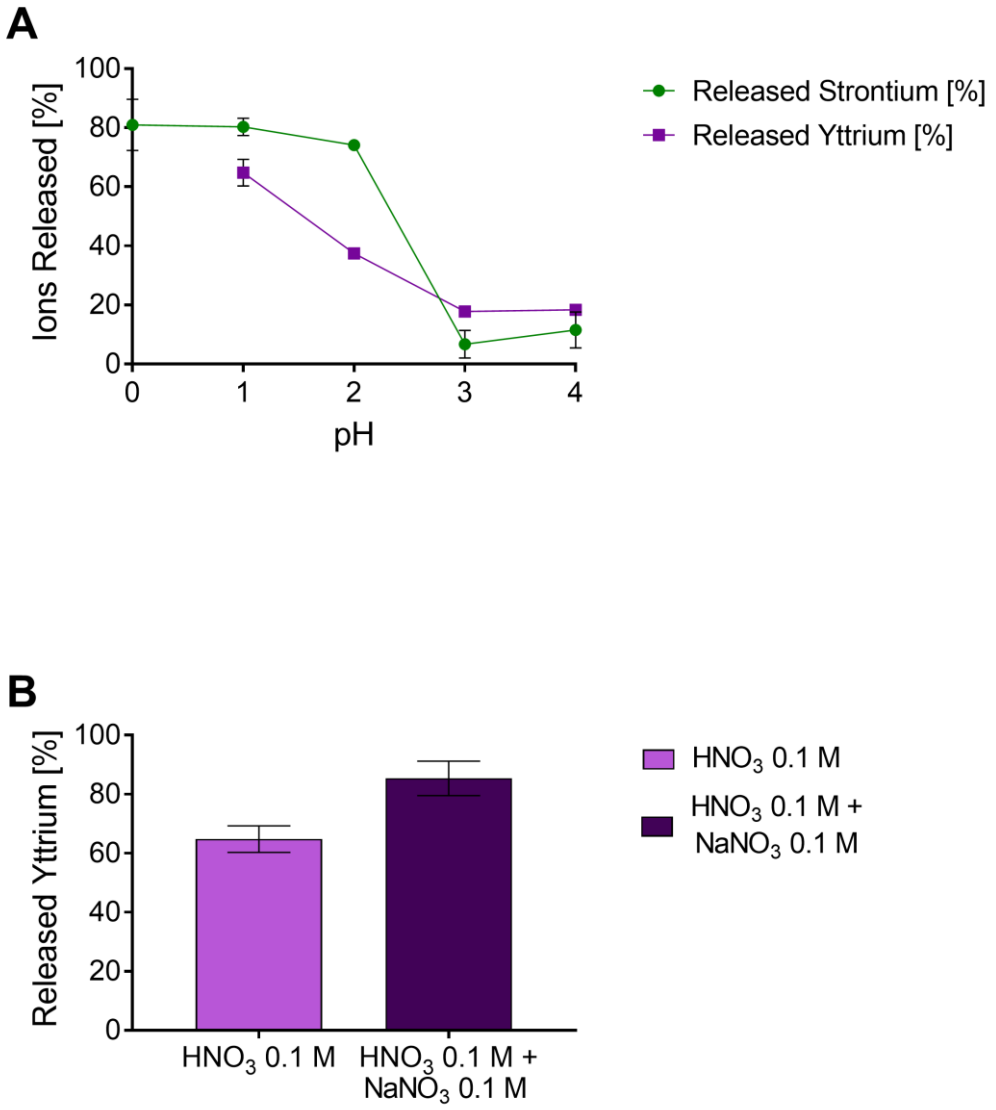

Figure 4.14. (A) Release of strontium (green lines) and yttrium (violet) lines at acidic pH. (B) Influence of $NaNO_3$ presence for yttrium release at pH=1.

4.3.5 Strontium behavior at acidic pH

The release of strontium from the resin at acidic pH by HCl (from 0 to 4), the only conditions which allowed the elution of yttrium, was studied. In figure 4.14 (A) the amount of strontium released from the resin in the first 5 mL of solution at the various pH is reported. At pH 3 and 4 the percentages of recovered strontium were 6.67 ±4.7% and 11.56 ±6.1% of the total strontium loaded in the column, respectively. The amount released increased tremendously at more acidic pH, being 74.12 ±0.9%, 80.29 ±2.9% and 80.99 ±8.7% at pH 2, 1 and 0, respectively.

When the second 5 mL used for the elution were analyzed no strontium could be detected, meaning that after the first washing, no more strontium could be recovered.

Afterwards the impact of the use of either HCl or HNO_3 on the release of strontium was studied. As can be observed from the graphs of figure 4.15, no influence could be observed.

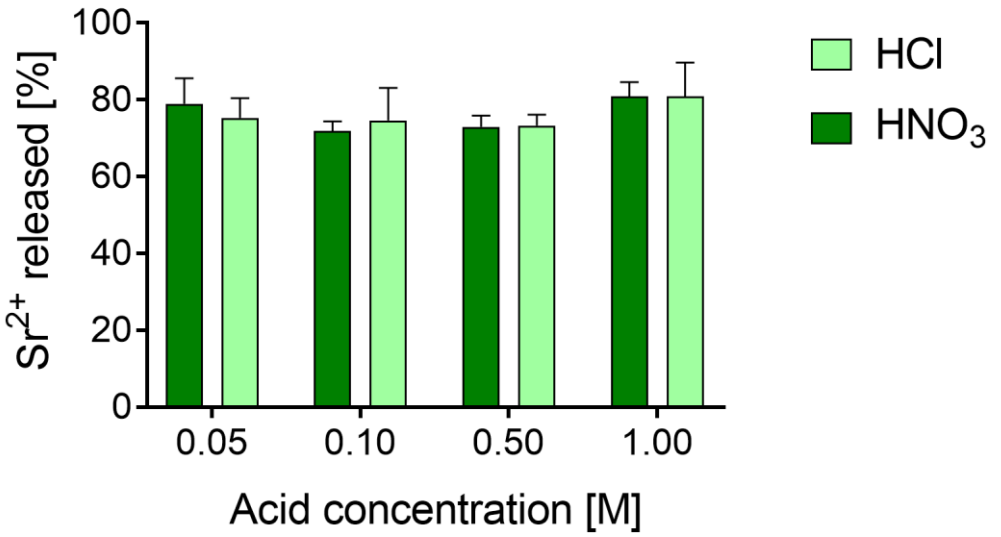

Figure 4.15. Release of strontium from NaTi using HNO_3 or HCl.

The amount of strontium released was not significantly different between hydrochloric and nitric acid; moreover, the results of these tests confirmed the data reported in figure 4.14 (A), because the released strontium was ~80% in a pH range between 1.3 (0.05 M) and 0 (1 M).

Finally, the presence of increasing quantity of $NaNO_3$ (0.1, 0.2, 0.5 and 1 M) in the acidic solution was evaluated and strontium release quantified. Independently on sodium nitrate amount, the release of strontium in the first 5 mL passed through the column was always ~60%, while no strontium was present in the solution analyzed after the elution with 5 mL more of acidic solution.

4.3.6 Purification of strontium from yttrium

The procedure developed for ^{89}Sr purification from the isobaric contaminant ^{89}Y, stable contaminant of strontium, is presented in figure 4.4. The process was developed on the ground of the behavior of NaTi with strontium and yttrium at the various pH using stable solutions of the elements under study. In the first step of the process, the eluted solution (E_1) had no detectable amounts of strontium and of yttrium. The second eluate (E_2) was the fraction containing the highest amount of strontium, because the eluent HCl 0.01 M (pH 2) allowed to recover ~74% of strontium, while minimizing yttrium

(~37% of the loaded), see figure 4.14 (A), discussed later. The third step allowed to eliminate all yttrium present in the resin and regenerate the column for further purifications.

4.3.7 Purification of yttrium from strontium: a possible generator for ^{90}Y with NaTi

For yttrium purification from strontium the procedure presented in figure 4.5 with NaTi was developed. The first step at basic pH, allowed to charge all strontium on the resin. The immediate acidic treatment was necessary to eliminate that part of strontium that would have been eluted during yttrium recovery. E_2 contained 60% of loaded strontium, which could be loaded on the column again. After 10-15 days the columns were treated with an acidic solution to recover yttrium. No strontium could be detected in the solutions coming from the columns where strontium had been loaded. In those where only yttrium was loaded, E_3 was evaluated. When a basic solution was passed through the column after passage 2, ~35% of yttrium was recovered. The acidic treatment, instead, allowed the recovery of ~40% of the loaded amount of yttrium, while the best conditions were those where the column was left at neutral pH. In these circumstances ~50% of yttrium could be recovered.

4.4 Discussion

In this chapter the synthesis and use of an inorganic resin, sodium nonatitanate, for yttrium and strontium purifications was described. All the tests were carried out with the use of stable ions, for this reason the analytical method had to be tuned according to the elements' concentrations and samples matrix. For strontium the analysis could be carried out thanks to atomic absorption adjusting the matrix with 0.3 M HNO_3 to increase the signal [4.15]. For yttrium a spectrophotometric analysis was developed with the use of the complexant Az(III) [4.16,4.17]. Thanks to the pH (2.1) it was possible to establish an accurate and linear method; this method proved to be selective for yttrium even at the presence of a high amount of strontium. The lowest yttrium concentration that could be quantified (Abs >0.1) was 300 μg/L. This value was in line with the literature data [4.16], but somehow limited the possibility of testing the resin

with lower amounts of yttrium. For each sample matrix it was possible to build linear and reliable calibration curves.

Sodium nonatitanate could be synthetized with a hydrothermal method at three different temperatures (100, 150 and 175 °C). The three types of NaTi, NaTi100, NaTi150 and NaTi175, respectively, had similar XRD spectra and showed all a low crystallinity. This result was expected, because NaTi can be produced with high crystallinity, only at higher temperatures of synthesis (> 180 °C) [4.12]. The morphology of the NaTi (see figure 4.7) obtained with SEM confirmed that our NaTis were semi-amorphous. Crystalline NaTi, synthesized by Merceille at 200 °C was needle shaped [4.12], while the NaTi100, NaTi150 and NaTi175 of this study were all grain-shaped. XRD spectra, even if not so clear due to the low crystallinity of NaTi, showed the four characteristic peaks of pure NaTi [4.12], confirming the nature of the resin. The interlayer distance of ~10 Å was typical of NaTi; the layers are made of TiO_6 octahedra spaced sodium ions and water molecules [4.8]. The BET results were also in line with the literature [4.12], the sample synthetized at 100 °C were scarcely porous (BET surface area 4.2 m^2/g), while highly mesoporous samples could be produced at higher temperature: 102 m^2/g and 226 m^2/g at 150 °C and 175 °C, respectively. These results, together with the efficiency in the uptake of strontium in the resin, which was not significantly different depending on the synthesis temperature (>99.8%), lead to the conclusion of always synthetizing NaTi at higher temperatures. Since the temperature of 175 °C, was at the safety limit for the synthesis vessel used in this study, for safety reasons the temperature of 150 °C was selected for the following NaTi productions.

The uptake of strontium in the resin was described as the ionic exchange between two Na^+ and one Sr^{2+}. Merceille demonstrated that the concentration of Na^+ influenced the uptake capacities of NaTi [4.6]. For this reason, in all experiments sodium concentration was strictly monitored. In particular, [Na^+] was kept constant at 0.1 M during the strontium sorption step. Since the secondary target developed for the collection of strontium ions (Chapter 2 and 3) is made of sodium chloride [4.2], we tested if a difference could be seen in the uptake of strontium when the concentration of NaCl was 0.3 M. This value is the calculated concentration of sodium chloride after dissolving the 13 mm secondary target in ~10 mL of solvent. In all the experiments the percentage of strontium retained in the NaTi was always >99.8%. The solutions to test the uptake of

strontium in the resin were always prepared at basic pH, because the affinity increases at pH>8 [4.6].

Sylvester described in a US patent in 2005 [4.7] the possibility of eluting ^{90}Y with a solution of a sodium salt at pH ≥ 7, from a generator made with NaTi, where ^{90}Sr had been loaded and let decay. In the tests performed for this PhD thesis yttrium could never be quantified after eluting the resin with a neutral or basic solution. Also the use of counter ions (as acetate) did not help. This was probably due to yttrium hydrolysis that at pH ≥8 forms yttrium hydroxide, a colloid that stuck in the resin. In our conditions it was possible to make yttrium go through the column only at acidic pH. When the solutions had pH >4 the concentration of yttrium was below the quantification limit (300 μg/L). At lower pHs: ~10 % of yttrium was measured (pH 3), ~58% at pH 2 and the entire amount of yttrium (100%) was recovered at pH=1. When yttrium was previously loaded at basic pH and then eluted with acidic solutions, the efficiencies were slightly reduced, see figure 4.14 (A). The use of sodium in the solution improved the recovery of yttrium from ~65% to ~85% at pH 1 (figure 4.14 (B)). The reason why yttrium could be recovered only at strong acidic pH values is that probably yttrium undergoes hydrolysis phenomena even at slightly acidic pH, forming colloids that stay in the resin. Moreover, NaTi is a resin that keeps a basic behavior because it has high affinity for H^+, so it exchanges protons for sodium ions, making the solutions more basic [4.5] and the pH at the interface with NaTi might be higher and cause yttrium precipitation *in situ*.

Since no discrimination between yttrium and strontium could be observed at neutral and basic pH, the behaviors of both ions were studied at acidic pH, after loading both of them on NaTi in a basic medium, and were compared in figure 4.14 (A). The pH which showed the highest difference between the two ions and so could be used to separate them was pH 2. At this pH the release of strontium was 74.12 ±0.9% and the release of yttrium was 37.4 ±1.5%. Thanks to these results the purification set up for ^{89}Sr, figure 4.4, was hypothesized. According to the suggested process the sodium chloride target where ^{89}Sr will be collected, will be dissolved in a basic solution made of NaOH 0.05 M. The solution will be loaded on the resin (>99.8% of Sr^{2+} will stay in the NaTi together with ^{89}Y). A simple elution with HCl 0.01 M (pH 2) will guarantee to recover ~80% of ^{89}Sr and ~37% of yttrium. Based on the consideration that very few yttrium atoms will be present as contaminants, due to the very low efficiency of its ionization

[4.2] and on the fact that it is a stable nuclide, the reduction of ~60% of yttrium could be considered satisfactory.

Regarding the purification of yttrium from strontium, the impossibility of recovering yttrium at neutral pH made the use of NaTi for this purification more challenging. The possibility of using the resin for the separation of ^{90}Y directly produced with ISOL technique from ^{90}Sr was excluded. For this reason, the studies were addressed to the use of NaTi for a generator ^{90}Sr/^{90}Y for ^{90}Sr produced with ISOL technique. Based on the observation that, after loading Sr^{2+} on the resin, only in the first passage of the acidic solutions strontium was released (74.12%, pH 2), while no Sr^{2+} could be detected after washing again, the procedure described in picture 4.5 was developed. This method foresees the loading of ^{90}Sr in NaOH 0.05 M and the washing with HCl 0.01 M, where part of ^{90}Sr will be lost, being this the weak point of the method. After waiting for the residual ^{90}Sr to decay, yttrium can be eluted with HCl/NaCl 0.1 M. The ^{90}Sr lost in the second step can be eventually recovered using a second column or loading the first column again.

4.5 Conclusion

In this chapter the synthesis and characterization of NaTi was described. This material was hydrothermally synthesized and three types of NaTis, depending on the temperatures of synthesis, were produced. The NaTi synthetized at 150 °C was then used to develop the purification method of strontium and yttrium. All the assays were carried out using the cold elements, for this reason analytical methods for strontium (GF-AAS) and for yttrium (UV-Vis) were developed. The affinity of NaTi for strontium was very high at basic pH, but also yttrium was retained in the resin. Yttrium could be recovered from NaTi only at acidic pH (<4), when also strontium was released. For this reason, the separation of the two ions turned out to be more challenging. An evaluation of the behavior of the two ions in the pH range from 0 to 4 made it possible to find a condition where the two ions behaved differently (pH 2). Its use for the purification of ^{89}Sr from the stable contaminant ^{89}Y, considering the very low amount of ^{89}Y in the solution, was satisfactory with a reduction of >60% of the initial amount. NaTi as a resin for a ^{90}Sr/^{90}Y generator was also studied and a process developed. In the

hypothesized system it will be possible to elute pure ^{90}Y after ^{90}Sr decay. The weak point of the system is the loss of ^{90}Sr in the loading process that needs to be optimized.

References

[4.1] C. Müller, K. Zhernosekov, U. Koster, K. Johnston, H. Dorrer, A. Hohn, N.T. van der Walt, A. Turler, R. Schibli, A Unique Matched Quadruplet of Terbium Radioisotopes for PET and SPECT and for - and --Radionuclide Therapy: An *In Vivo* Proof-of-Concept Study with a New Receptor-Targeted Folate Derivative, J. Nucl. Med. 53 (2012) 1951–1959. doi:10.2967/jnumed.112.107540.

[4.2] F. Borgna, M. Ballan, S. Corradetti, E. Vettorato, A. Monetti, M. Rossignoli, M. Manzolaro, D. Scarpa, U. Mazzi, N. Realdon, A. Andrighetto, A preliminary study for the production of high specific activity radionuclides for nuclear medicine obtained with the isotope separation on line technique, Appl. Radiat. Isot. 127 (2017). doi:10.1016/j.apradiso.2017.06.022.

[4.3] I. Kuroda, Effective use of strontium-89 in osseous metastases, Ann. Nucl. Med. 26 (2012) 197–206. doi:10.1007/s12149-011-0560-5.

[4.4] A. Monetti, A. Andrighetto, C. Petrovich, M. Manzolaro, S. Corradetti, D. Scarpa, F. Rossetto, F. Martinez Dominguez, J. Vasquez, M. Rossignoli, M. Calderolla, R. Silingardi, A. Mozzi, F. Borgna, G. Vivian, E. Boratto, M. Ballan, G. Prete, G. Meneghetti, The RIB production target for the SPES project, Eur. Phys. J. A. 51 (2015). doi:10.1140/epja/i2015-15128-6.

[4.5] P. Sylvester, Strontium From Nuclear Wastes : Ion Exchange, (1989) 4261–4267.

[4.6] A. Merceille, E. Weinzaepfel, Y. Barré, A. Grandjean, The sorption behaviour of synthetic sodium nonatitanate and zeolite A for removing radioactive strontium from aqueous wastes, Sep. Purif. Technol. 96 (2012) 81–88. doi:10.1016/j.seppur.2012.05.018.

[4.7] P. Sylvester, Ion exchange materials for the separation of ^{90}Y from ^{90}Sr, US 6,974,563 B2, 2005. doi:10.1016/j.(73).

[4.8] P. Sylvester, T. Möller, T.W. Adams, Improved separation methods for the recovery of ^{82}Sr from irradiated targets, Appl. Radiat. Isot. 64 (2006) 422–430. doi:10.1016/j.apradiso.2005.08.014.

[4.9] A. Villard, B. Siboulet, G. Toquer, A. Merceille, A. Grandjean, J.F. Dufrêche, Strontium selectivity in sodium nonatitanate $Na_4Ti_9O_{20}$·xH2O, J. Hazard. Mater. 283 (2015) 432–438. doi:10.1016/j.jhazmat.2014.09.039.

[4.10] C.L. Hanks, D.J. Hamman, Radiation Effects Design Handbook: Section 3.

Electrical Insulating Materials and Capacitors, Security. (1971) 88. doi:NASA CR-1787.

[4.11] E.A. Behrens, P. Sylvester, A. Clearfield, Assessment of a Sodium Nonatitanate and Pharmacosiderite-Type Ion Exchangers for Strontium and Cesium Removal from DOE Waste Simulants, Environ. Sci. Technol. 32 (1998) 101–107. doi:10.1021/es9704794.

[4.12] A. Merceille, E. Weinzaepfel, Y. Barré, A. Grandjean, Effect of the synthesis temperature of sodium nonatitanate on batch kinetics of strontium-ion adsorption from aqueous solution, Adsorption. 17 (2011) 967–975. doi:10.1007/s10450-011-9376-9.

[4.13] G. Demazeau, Solvothermal reactions: an original route for the synthesis of novel materials, J. Mater. Sci. 43 (2008) 2104–2114. doi:10.1007/s10853-007-2024-9.

[4.14] H. Hayashi, Y. Hakuta, Hydrothermal Synthesis of Metal Oxide Nanoparticles in Supercritical Water, Materials (Basel). 3 (2010) 3794–3817. doi:10.3390/ma3073794.

[4.15] W. Frech, A. Cedergren, Investigations of reactions involved in flameless atomic absorption procedures, Anal. Chim. Acta. 88 (1977) 57–67. doi:10.1016/S0003-2670(01)96049-0.

[4.16] E. Bruneel, D. Verbauwhede, D. Van de Vyver, J. Schaubroeck, S. Hoste, I. Van Driessche, Accurate determination of the composition of Y-Ba-Cu-O superconductor by spectrophotometry, gravimetry and flame AAS, Supercond. Sci. Technol. 18 (2005) 907–911. doi:10.1088/0953-2048/18/6/019.

[4.17] H. Rohwer, N. Collier, E. Hosten, Spectrophotometric study of arsenazo III and its interactions with lanthanides, Anal. Chim. Acta. 314 (1995) 219–223. doi:10.1016/0003-2670(95)00279-9.

[4.18] W.H. Bragg, W.L. Bragg, The Crystalline State, Volume I, A general survey, G. Bell & Sons, London, 1933.

[4.19] V. Michaylova, N. Kouleva, Spectrophotometric study of the reactions of arsenazo III with alkaline-earth metals, Talanta. 21 (1974) 523–532. doi:10.1016/0039-9140(74)80181-5.

Chapter 5

Radiolabeling and Characterization of Plasma Protein-Binding Ligands

The work described in this chapter was carried out at the Center for Radiopharmaceutical Sciences (CRS) of Paul Scherrer Institute (PSI), in the group of PD Dr. Cristina Müller, who kindly gave me the possibility of working on this project. Her research focus is the development of small molecular weight radiopharmaceuticals for targeting the folate receptor and the prostate specific membrane antigen. The work was, recently published in the journal Bionjugate Chemistry: http://pubs.acs.org/doi/10.1021/acs.bioconjchem.7b00378.

5.1 Introduction

Drug discovery is aimed at the development and selection of drug candidates with favorable pharmacokinetic (PK) and pharmacodynamic profiles in order to optimize the biological activity and minimize undesired side effects [5.1]. Drug candidates that are cleared too fast from the blood circulation require large dosage and/or repeated administration which may lead to unwanted toxicity to healthy organs and tissue [5.2]. Increasing the half-life of therapeutics in the blood has, therefore, been regarded as a valuable means to reduce the number of injections and improve the efficacy of the drug. A wide variety of techniques meant to enhance the blood circulation time of drug candidates have been proposed and studied [5.3,5.4]. Conjugation of drug molecules with high-molecular weight polyethyleneglycole (PEG) or carbohydrate polymers has been used to increase the blood permanence by reducing glomerular filtration [5.4]. In the case of peptide-based molecules, chemical modification with for instance unnatural amino acids have been employed to reduce unwanted enzymatic degradation [5.5]. Another strategy to increase the blood circulation time of drugs is to enhance their binding capability to blood components with long circulation half-lives, such as the Fc region of IgG isotype antibodies, lipoproteins or blood plasma proteins[5.1,5.6]. Indeed,

the extent of binding to plasma proteins influences the pharmacokinetic profile of drugs which show reduced blood clearance with high binding capability [5.1]. While plasma binding properties may reduce the therapeutic effect as only the free fraction can penetrate biological barriers and reach the therapeutic target [5.2], it is considered as a valuable strategy to avoid undesired side effects of drugs with a narrow therapeutic window such as anticancer therapeutics [5.7].

The most important proteins responsible for drug binding are human serum albumin (HSA) and α_1-acid glycoprotein (α_1-AGP) [5.1]. The HSA accounts for 55% of the total plasma protein pool (blood plasma concentration: ~700 μM) and is, thus, a major protein component of blood plasma [5.8]. It is composed of a single, non-glycosylated amino acid chain with a molecular weight of ~66 kDa and a long blood plasma half-life of ~19 days [5.1,5.7]. HSA plays an important role in the transport of various endogenous and exogenous compounds as it has an extraordinary ligand binding capacity and can reversibly bind acidic and neutral compounds [5.1]. It is composed of three main domains (I, II, III) which are each divided into two helical subdomains (A and B) [5.8]. Two main drug binding sites have been identified: (*i*) Sudlow's site I is located on the subdomain IIA and binds bulky heterocyclic anions such as the anticoagulant warfarin, whereas (*ii*) Sudlow's site II is located in the subdomain IIIA and binds preferentially extended aromatic carboxylates molecules such as ibuprofen, a non-steroidal anti-inflammatory drug [5.8].

α_1-AGP is smaller (38-48 kDa) than HSA, highly glycosylated and present at lower blood plasma levels (10-30 μM) [5.1]. Its blood plasma half-life of ~2-3 days is dependent on the extent of glycosylation [5.9]. α_1-AGP is responsible for the transport of lipophospholipids and biliverdin, but also for exogenous ligands such as antibiotics and anticancer drugs. The binding capacity of α_1-AGP is lower than of HSA, but the binding affinity of its ligands, mostly basic compounds, is commonly higher [5.1].

Human transthyretin (hTTR) − originally referred to as pre-albumin − is a protein (55 kDa) present in blood plasma at much lower levels (~5 μM) than HSA. It acts as a transport molecule for thyroxine hormones and holo-retinol-binding protein [5.10]. hTTR is a homo-tetramer and has an *in vivo* half-life of ~2 days [5.11]. Recently, drug binding to hTTR has been demonstrated as a novel strategy to prevent fast clearance of therapeutic drugs [5.11].

Targeted radionuclide therapy makes use of a tumor targeting agent to deliver the therapeutic radionuclide to the tumor site where it acts as a source of radiation to damage cancer cells [5.12]. These radiotherapeutic drugs should ideally accumulate specifically at diseased sites while sparing healthy tissue from radiotoxic effects [5.13]. In recent years, it has been demonstrated pre-clinically that plasma protein binding may be of value for the development of radiopharmaceuticals enabling high tumor uptake and reducing renal clearance and related toxicities [5.14,5.15]. More recently, a DOTA-based bisphosphonate as well as PSMA-targeting ligands have been modified with an albumin-binding entity to improve their tissue-distribution profile [5.16–5.18]. It is, thus, of interest to identify and compare different types of plasma protein binding entities to be conjugated with targeting ligands in order to optimize the pharmacokinetics of these (radio)therapeutics.

The aim of this study was to evaluate and compare three different plasma protein binders potentially useful in combination with radiopharmaceuticals. Among those was a 4-(4-iodophenyl)butyric acid derivative (PPB-01) previously discovered from a DNA-encoded chemical library by Dumelin *et al.* [5.19]. This entity was previously used in combination with antibody fragments [5.20] as well as with folic acid radioconjugates [5.15,5.21] where the desired effect of enhanced blood circulation of the biomolecule was successfully demonstrated. The second compound was based on an ethynyl benzene entity (PPB-02). The ethynyl moiety served as a bioisosteric replacement of the iodine of compound PPB-01 based on a study in which the ethynyl group was evaluated as a halogen bioisostere [5.22]. The third entity (PPB-03) was recently reported to effectively bind to transthyretin (hTTR) [5.23]. The three entities were functionalized with a DOTA chelator via a L-lysine and β-alanine linker moiety using solid phase peptide chemistry (Figure 5.1). Radiolabeling was performed with ^{177}Lu (^{177}Lu: $T_{1/2}$ = 6.7 d; $E\beta^-_{average}$ = 134 keV; Eγ = 113 keV, 208 keV), an established radiometal used in clinics for targeted therapy. The three radioligands were investigated extensively *in vitro* and compared with regard to their blood clearance in mice.

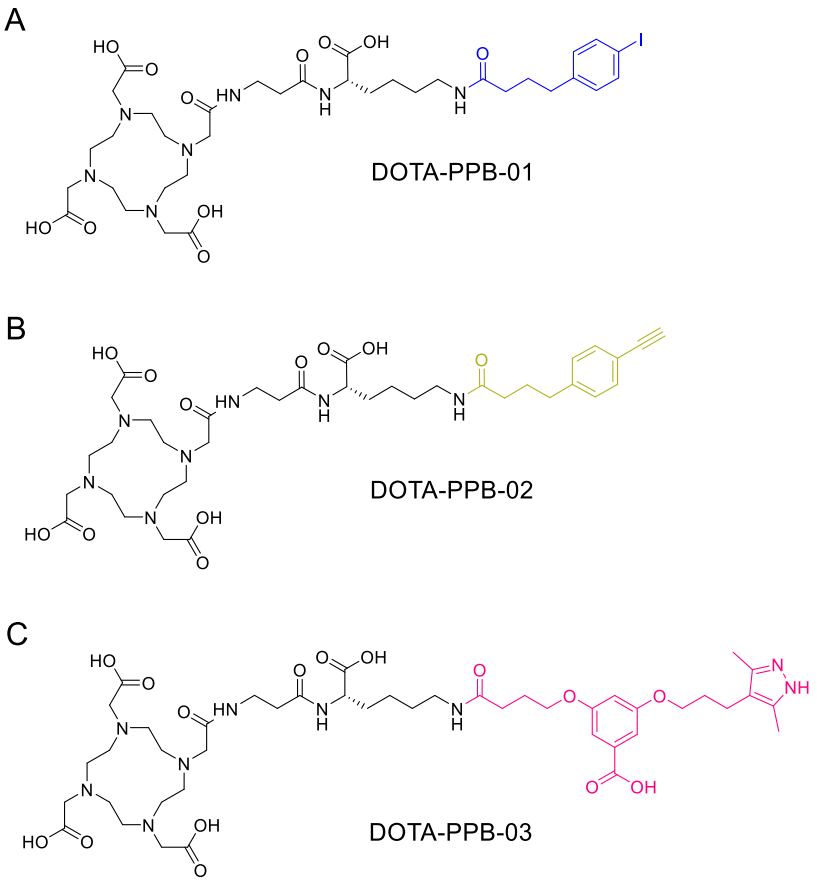

Figure 5.1. Chemical structures of the investigated plasma protein-binding ligands: DOTA-PPB-01, DOTA-PPB-02 and DOTA-PPB-03.

5.2 Experimental

All reagents and solvents were purchased from Sigma-Aldrich (Germany), Merck (Germany) and Fluka (Switzerland), respectively, and used without further purification or drying. All chemicals used for the radiolabeling were metal-free and obtained from Sigma-Aldrich (Germany) in Suprapur quality. Analytical radio-HPLC was performed on a Merck-Hitachi HPLC equipped with a L-6200A pump, a L-3000 Photo Diode Array detector and a Berthold LB 508 radiometric detector. For this purpose, a reversed-phase C18 column (5 µm, 4.6 mm x 150 mm, XTerra^{TM} MS, Waters, USA) was used. The compounds were synthetized in PD Dr. Müller's group [5.24].

5.2.1 Preparation of ^{177}Lu-DOTA-PPB Ligands and ^{177}Lu-DOTA.

Each compound, DOTA-PPB-01, DOTA-PPB-02, DOTA-PPB-03 and DOTA, respectively, was labeled at the specific activity up to 50 MBq/nmol with ^{177}Lu (Isotope Technologies Garching ITG GmbH). The reaction mixture consisted of HCl 0.05 M and

Na-acetate 0.5 M (pH 8) at the ratio of 5:1 in order to obtain a solution of pH ~4.5. After the addition of the compounds (stock solutions of 1 mM), the reaction mixture was incubated at 95 °C for 10 min. The quality control of ^{177}Lu-DOTA-PPB-01, ^{177}Lu-DOTA-PPB-02 and ^{177}Lu-DOTA-PPB-03 was carried out by reversed-phase high-performance liquid chromatography (RP-HPLC) analysis (Merck LaChrom HPLC) using a C18 column (5 µm, 4.6 mm x 150 mm, XTerra^{TM} MS, Waters USA). The eluent consisted of acetonitrile (solvent A) and 0.1% TFA in H_2O (solvent B). A gradient of 5-80% A and 95-20% B was used over 15 min at a flow rate of 1.0 mL/min. The quality control of ^{177}Lu-DOTA was carried out via thin layer chromatography (TLC) using silica gel plates (~100 x 100 mm^2 obtained from commercial plates available at 200 x 200 mm^2, 200 µm, 60Å, VWR, Switzerland). As a liquid phase ammonium acetate 10% and methanol (1:1 volume ratio, pH 5.5) was used over a front of 50 mm. The ^{177}Lu-labeled DOTA complex migrated with the liquid phase (R_f = 0.5) and free ^{177}Lu remained at the starting line (R_f = 0). The TLC plate was exposed to a multisensitive medium phosphor screen (Type MS, Perkin Elmer) for 15 s using a Cyclone Plus Storage Phosphor System (Perkin Elmer) and analyzed with *Optiquant* software (version 5.0).

5.2.2 Stability of the radioligands

The three compounds DOTA-PPB-01, DOTA-PPB-02, DOTA-PPB-03 were labeled at a specific activity of 50 MBq/nmol for testing the stability in PBS pH 7.4 and human plasma. The radiochemical purity was determined immediately after production (T = 0) using HPLC. Dilutions of the labeling solution of each compound were prepared at low activity concentration (~10 MBq/500 µL) using PBS pH 7.4 with and without the addition of ascorbic acid (~120 µg). In addition, the stability of the radioligands was checked at higher activity concentrations (250 MBq/500 µL) with the addition of a higher amount of ascorbic acid (3 mg). In the latter case, it was necessary to adjust the pH by addition of a solution of sodium acetate (0.5 M, pH 8, 150 µL) to obtain a value of 7.0-7.5. The integrity of the radioligands was determined after incubation periods of 4 h, 24 h and 48 h.

For the determination of plasma stability, the radioligands were diluted to 30 MBq/500 µL using PBS pH 7.4. An aliquot of the prepared dilutions (50 µL, ~3 MBq) were incubated in human plasma (Foundation Blood Donation SRK Aargau-Solothurn,

Switzerland, ~250 µL) at 37 °C. The compounds' integrity was determined after 4, 24 and 48 h. For this purpose, aliquots of the plasma (50 µL) were treated with three-fold volume of methanol to precipitate plasma proteins. After centrifugation the supernatants were filtered and used for analysis using HPLC.

The HPLC chromatograms were analyzed by determination of the peak area of the radioligand and set into relation to the area of the radioligand observed at T = 0 which was set to 100%.

5.2.3 Determination of LogD values

The n-octanol/PBS distribution coefficients (logD values) of the ^{177}Lu-labeled compounds (DOTA-PPB-01, DOTA-PPB-02, DOTA-PPB-03 and DOTA, respectively) were determined using a previously published procedure [5.25]. In brief, the compounds were labeled at the specific activity of 50 MBq/nmol. A sample of the ^{177}Lu-labeled compound (25 µL; ~500 kBq) was mixed with PBS pH 7.4 (1475 µL) and n-octanol (1500 µL). The vials were vortexed vigorously for 1 min and then centrifuged (2000 rpm) for 6 min for phase separation. The activity concentration in a defined volume of each layer was measured in a γ-counter (Perkin Elmer, Wallac Wizard 1480). The distribution coefficient was expressed as the logarithm of the ratio of counts per minute (cpm) measured in equal volumes of the n-octanol phase to the cpm measured in the PBS phase. The values reported are the mean (± standard deviation, SD) of the results of three independent experiments, each performed with five replicates. Significance of the data was determined using a one-way ANOVA with Bonferroni`s multiple comparison post-test (*GraphPad Prism* software, version 5.01). A p-value of <0.05 was considered statistically significant.

5.2.4 Determination of Plasma Protein-Binding Properties

An ultrafiltration assay was performed for determination of the plasma protein binding of the three labeled compounds and of the control ^{177}Lu-DOTA. For this purpose, the compounds were labeled at the specific activity of 50 MBq/nmol. The labeling solutions were diluted to an activity concentration of 10 MBq in 500 µL PBS pH 7.4. Ascorbic acid (120 µg) was added to these solutions to prevent radiolysis of the radioligands. The diluted radioligands (25 µL, ~500 kBq, 0.01 nmol) were added to human plasma (250 µL) as well as to solutions of human serum albumin (HSA, Sigma Aldrich, fatty acid-

free, globulin free, ≥99%, 700 μM, 250 μL), human α_1-acid glycoprotein (hAGP, Sigma Aldrich, ≥99%, 30 μM, 250 μL), human transthyretin (hTTR, Sigma Aldrich, ≥99%, 5 μM, 250 μL) diluted in PBS pH 7.4, respectively, and incubated at 37°C for 30 min. A control experiment was performed using PBS pH 7.4 only. After incubation, the samples were loaded onto the ultrafiltration devices (Centrifree ultrafiltration devices; 30,000 Da nominal molecular weight limit, methylcellulose micropartition membranes, Millipore) and centrifuged at 2000 rpm for 40 min at 20 °C. The filtered solutions were measured in a γ-counter. The counts of the filtered solutions were calculated as a fraction of the radioactivity in the corresponding loading solutions which was set to 100%. The reported values represent the average of three independent measurements (± standard deviation), each performed with two replicates. Significance of the data was determined using a two-way ANOVA with Bonferroni`s multiple comparison post-test (*GraphPad Prism* software, version 5.01). A p-value of <0.05 was considered statistically significant.

5.2.5 Determination of Relative Binding Affinity to Plasma Proteins

In order to better understand the binding properties of the radioligands, the percentage of bound radioligand to plasma proteins was determined at different plasma proteins/radioligand ratios, by means of an ultrafiltration assay. The compounds were labeled at a specific activity of 50 MBq/nmol and diluted with PBS (pH 7.4) to 10 MBq/500 μL. Ascorbic acid (120 μg) was added to these solutions to prevent radiolysis of the radioligands. The diluted radioligands (25 μL, 0.01 nmol for ^{177}Lu-DOTA-PPB-01 and ^{177}Lu-DOTA-PPB-03 and 12.5 μL, 0.005 nmol for ^{177}Lu-DOTA-PPB-02) were added to previously prepared plasma dilutions. Five different plasma concentrations were prepared in a volume of 250 μL using PBS (pH 7.4) (Table 5.1).

The samples were incubated for 30 min at 37 °C followed by filtration as described above in order to determine the bound fraction. The obtained values were analyzed by a semi-logarithmic plot to obtain the IC_{50} values using the *GraphPad Prism* software (version 5.01). The IC_{50} value of ^{177}Lu-DOTA-PPB-01 was set to 1.0. The inverse ratio of the IC_{50} values of the other compounds was calculated to allow comparison of the binding affinities of all three radioligands.

Table 5.1. Dilutions for determination of relative plasma-proteins-binding affinity

Dilution	HSA concentration in plasma [μM]	[HSA] in plasma-to-[Radioligand] ratio
1	700	17500
2	40	1000
3	4	100
4	0.4	10
5	0.0004	0.01

5.2.6 Determination of the Affinity of the Radioligands to HSA and hTTR

The binding affinity of ^{177}Lu-DOTA-PPB-01 and ^{177}Lu-DOTA-PPB-02 to HSA was determined using the ultrafiltration method. A fixed concentration of HSA (35 μM) was incubated at room temperature for 30 min with increasing amounts of radioligand (10-150 μM), prepared by mixing radiolabeled compound (~10 MBq/nmol) with increasing amounts of cold compound and ascorbic acid in PBS pH 7.4. The solutions were then incubated at room temperature for 30 min before filtration. The affinity of ^{177}Lu-DOTA-PPB-03 to hTTR was determined using the same ultrafiltration method. A fixed concentration of hTTR (5 μM) was incubated at room temperature for 30 min with increasing amounts of radioligand (10-1000 nM), prepared by mixing radiolabeled compound (~10 MBq/nmol) with increasing amounts of cold compound and ascorbic acid in PBS pH 7.4. The amount of free radioligand was determined in the filtrate allowing calculation of the bound fraction. The counts of the bound fraction were plotted against the concentration of the radioligand with a non-linear fitting of the data points using *Graph Pad Prism* software (version 5.01) for determination of the K_D values.

5.2.7 Displacement Experiments on HSA using Warfarin and Ibuprofen

To estimate the preferential binding site of the compounds on HSA, displacement studies were carried out with warfarin (Sigma-Aldrich) and ibuprofen (Sigma-Aldrich, purity ≥98%) respectively, both used as sodium salts. These drugs served as specific markers for HSA binding sites Sudlow's site I (warfarin) and Sudlow's site II (ibuprofen), respectively [5.8]. HSA, warfarin and ibuprofen were dissolved in PBS (pH 7.4). The concentration of HSA was 70 μM for investigating ^{177}Lu-DOTA-PPB-01 and 140 μM for investigating ^{177}Lu-DOTA-PPB-02 and ^{177}Lu-DOTA-PPB-03, respectively. In order to saturate the binding sites, warfarin and ibuprofen were added to the HSA in 10-fold excess, which means at a concentration of 700 μM for the investigation of ^{177}Lu-DOTA-PPB-01 and 1.4 mM for the investigation of ^{177}Lu-DOTA-PPB-02 and ^{177}Lu-DOTA-PPB-03, respectively. After incubation of the mixtures for 30 min at 37 °C the binding was determined using the ultrafiltration assay. In each experiment control samples were treated equally but incubated without addition of the competitor. The result of the bound fraction in the control sample was set as 100% and the percentage of the radioligand bound to HSA in experiments performed with warfarin and ibuprofen, respectively, was expressed as a percentage of the control value.

5.2.8 Displacement Experiments on hTTR using L-Thyroxine

It is known that hTTR has a binding site for the transport of L-thyroxine in blood. The binding entity of ^{177}Lu-DOTA-PPB-03 was previously reported to bind to this binding pocket of hTTR [5.11]. A displacement assay was performed using a solution of hTTR (5 μM) and L-thyroxine (50 μM) in PBS followed by addition of ^{177}Lu-DOTA-PPB-03 (25 μL, ~500 kBq, 0.01 nmol, labeled at ~50 MBq/nmol) in a final volume of 250 μL. A control experiment was carried in parallel using the same mixture, but without the addition of L-thyroxine. The solutions were incubated at 37 °C for 30 min and then processed using the ultrafiltration assay. Displacement studies on hTTR were not performed for ^{177}Lu-DOTA-PPB-01 and ^{177}Lu-DOTA-PPB-02, respectively, due to the lack of binding of these radioligands to this protein (Figure 5.4 A).

5.2.9 Displacement Experiments using Plasma Protein-Binding Entities

Competition assays for HSA binding were performed with ^{177}Lu-DOTA-PPB-01, ^{177}Lu-DOTA-PPB-02 and ^{177}Lu-DOTA-PPB-03 using the respective binding entities PPB-01, PPB-02 and *PPB-03, a truncated version of PPB-03 [5.24]. ^{177}Lu-DOTA-PPB-03 was additionally tested with regard to hTTR binding using *PPB-03 for displacement. The concentrations of HSA and hTTR were 140 μM and 5 μM, respectively, while the binding entities were prepared at a 10-fold increased concentration as compared to the protein concentration. The mixed solutions were incubated for 30 min at 37 °C and the bound fractions of the respective radioligand were determined using the ultrafiltration assay.

5.2.10 In Vivo Studies

In vivo experiments were approved by the local veterinarian department and conducted in accordance with the Swiss law of animal protection. Female Balb/c mice at the age of 5 weeks were obtained from Charles River Laboratories (Sulzfeld, Germany). The mice received standard rodent chow (Kliba Nafag, Switzerland) ad libitum. For *in vivo* SPECT/CT scans, mice were anesthetized with a mixture of isoflurane (1.5-2.0%) and oxygen.

5.2.11 Blood Clearance

Blood clearance of the ^{177}Lu-labeled ligands (DOTA-PPB-01, DOTA-PPB-02 and DOTA-PPB-03, respectively) was determined in three mice per compound. The radioligands were prepared at the specific activity of 10 MBq/nmol. After labeling, ascorbic acid (2.4 μg per 10 MBq) was added to avoid radiolysis. Mice were intravenously injected with the radioligands diluted in PBS pH 7.4 (10 MBq, 1 nmol, 100 μL per mouse). Blood samples (1 μL) were taken in triplicate from the tail vein at 3 min, 1 h, 2 h, 4 h, 8 h and 24 h after injection of the radioligand, using 1 μL-capillaries. In the case of ^{177}Lu-DOTA-PPB-01 and ^{177}Lu-DOTA-PPB-03 blood sampling was also performed at later time points. The collected blood samples were measured in a γ-counter (Perkin Elmer, Wallac Wizard 1480). Assuming that the total blood volume of a mouse would be ~2 mL, the results were listed as percentage of injected activity per 2 mL of blood (% IA/2 mL). The total injected activity was determined by measuring a

defined volume of the original injection solution at the same time as the blood samples resulting in decay corrected values. The blood concentration values were analyzed and fitted with a bi-compartmental model using the *PK solver* software to obtain an area under the curve (AUC) over the time period of interest and extrapolated to infinite (0-∞) and the blood half-lives [5.26]. As a control, three mice were injected with ^{177}Lu-DOTA (10 MBq, 1 nmol, 100 µL per mouse) and blood samples were taken after 3 min, 15 min 30 min, 1 h and 2 h.

5.2.12 SPECT/CT Imaging Studies.

Imaging studies were performed using a four-head, multiplexing, multipinhole small-animal SPECT camera (NanoSPECT/CT™, Mediso Medical Imaging Systems, Budapest, Hungary). Each head was outfitted with a tungsten-based aperture of nine 1.4 mm-diameter pinholes and a thickness of 10 mm. The energy peaks for the camera were set at 56.1 keV (± 10%), 112.9 keV (± 10%) and 208.4 keV (± 10%). The compounds were labeled with ^{177}Lu at the specific activity of 20 MBq/nmol and diluted to 20 MBq/100 µL (~1 nmol injected per mouse). SPECT/CT scans of 40 min duration were performed 4 h after injection of mice followed by CT scans which lasted for 7.5 min. The images were acquired using the *Nucline* software (version 1.02, Mediso Ltd., Budapest, Hungary). The real-time CT reconstruction used a cone-beam filtered backprojection. The reconstruction of SPECT data was performed using the *HiSPECT* software (version 1.4.3049, Scivis GmbH, Göttingen, Germany). Images were prepared using the *VivoQuant* post-processing software (version 2.5, inviCRO Imaging Services and Software, Boston, U.S.). A Gauss post-reconstruction filter (full width at half maximum = 1 mm) was applied for the presentation of the SPECT image and the scale was adjusted to allow the best visualization of the radioligands distribution.

5.3 Results

5.3.1 Preparation of ^{177}Lu-Labeled Ligands

The radiochemical purity of ^{177}Lu-DOTA-PPB-01, ^{177}Lu-DOTA-PPB-02, ^{177}Lu-DOTA-PPB-03 and ^{177}Lu-DOTA, labeled at a specific activity of 50 MBq/nmol, was ≥97%. The HPLC retention times of ^{177}Lu-DOTA-01, ^{177}Lu-DOTA-PPB-02 and ^{177}Lu-DOTA-

PPB-3 were determined as 11.8 min, 11.3 min and 10.1 min respectively (Figure 5.2 and Table 5.2).

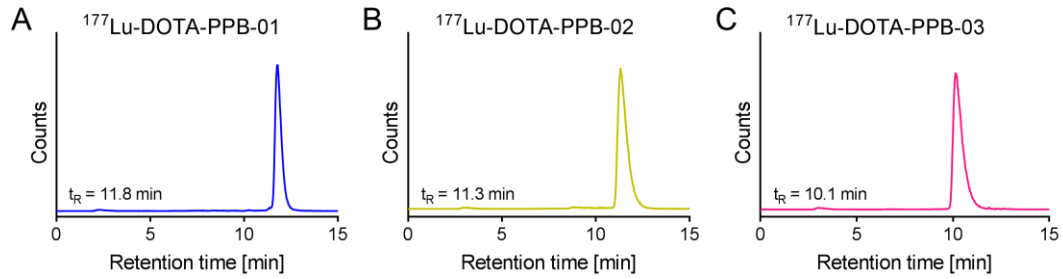

Figure 5.2. HPLC chromatograms of (A) ^{177}Lu-DOTA-PPB-01, (B) ^{177}Lu-DOTA-PPB-02 and (C) ^{177}Lu-DOTA-PPB-03 with corresponding retention times.

Table 5.2. Summary of the in Vitro Properties of the ^{177}Lu-Labeled Ligands

	^{177}Lu-DOTA-PPB-01	**^{177}Lu- DOTA-PPB-02**	**^{177}Lu- DOTA-PPB-03**	**^{177}Lu- DOTA**
HPLC retention times [min]	11.8	11.3	10.1	0.5**
LogD value	-3.15 ± 0.04	-4.02 ± 0.02	<-5	<-5
Plasma protein binding [%]	93 ± 1.5	70 ± 0.6	94 ± 0.6	<1
HSA binding [%]	95 ± 0.6	83 ± 0.6	57 ± 0.6	<1
Human α1-AGP [%]	39 ± 9.6	13 ± 4.5	4.0 ± 1.1	<1
Human Transthyretin* [%]	9.0 ± 1.0	7.0 ± 2.1	50 ± 0.6	<1

* also referred to as prealbumin; ** TLC R_f value

5.3.2 Stability of ^{177}Lu-Labeled Ligands

Stability experiments revealed that ^{177}Lu-DOTA-PPB-01 in PBS pH 7.4 (10 MBq/250 µL) was not sufficiently stable as only 88% intact compound were found after 4 h and this amount dropped further to 32% intact compound after 48 h. The addition of ascorbic acid increased the stability of ^{177}Lu-DOTA-PPB-01 significantly demonstrated by 97% completely intact after 4 h and 88% after 48 h. ^{177}Lu-DOTA-PPB-02 (10 MBq/250 µL) showed a similar behavior. Without ascorbic acid the product peak quickly decreased to 94% after 4 h and dropped further to 42% after 48 h. Stability was increased by addition of ascorbic acid resulting in 97% intact compound after 4 h and 87% after 48 h. ^{177}Lu-DOTA-PPB-03 (10 MBq/250 µL) revealed to be more stable with

>98% intact product after 4 h and still >75% after 48 h. The addition of ascorbic acid improved the stability allowing to maintain the compound completely intact (>98%) over the whole time of investigation (Figure 5.3).

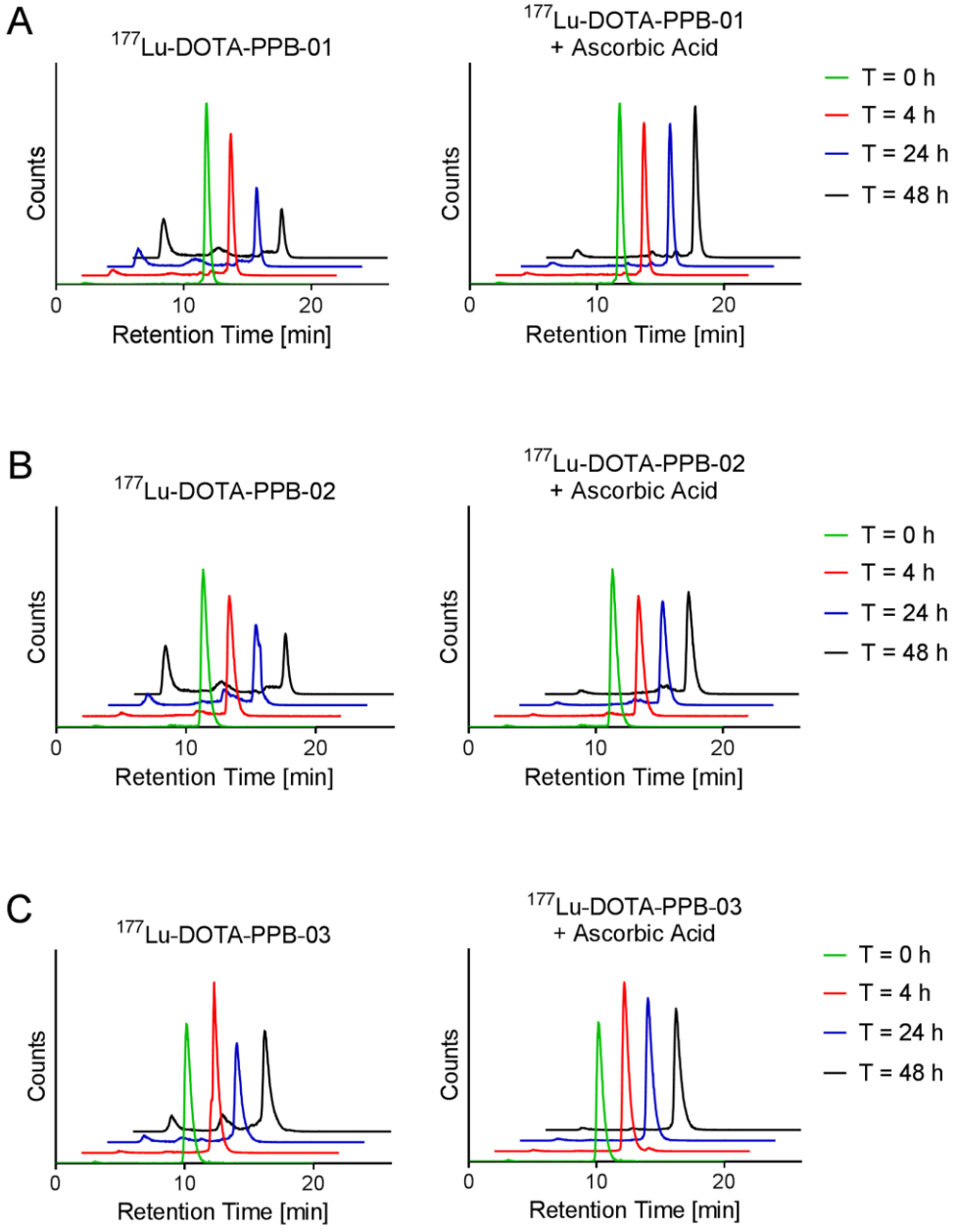

Figure 5.3. Results of the stability experiments performed with (A) ^{177}Lu-DOTA-PPB-01, (B) ^{177}Lu-DOTA-PPB-02 and (C) ^{177}Lu-DOTA-PPB-03. The stability was evaluated for the three radioligands diluted in PBS (10 MBq/250 µL), with and without the addition of the scavenger ascorbic acid, after incubation of up to 48 h.

With the addition of ascorbic acid (3 mg) all radioligands were stable even when diluted at high activity concentration (250 MBq/500 µL). ^{177}Lu-DOTA-PPB-01 and ^{177}Lu-DOTA-PPB-02 were almost completely intact (>97%) after 4 h and showed only slight

degradation after 24 h (>90% and >92% intact radioligand, respectively). Both radioligands remained relatively stable showing ~88% intact product at 48 h. Due to the high stability shown for ^{177}Lu-DOTA-PPB-03 at low activity concentrations, this compound was also evaluated at high activity concentration (250 MBq/500 µL) without addition of ascorbic acid. It was shown that this radioligand remained largely intact (~91%) after 4 h, but after 24 h only ~55% of intact radioligand was determined, however, when ascorbic acid was added the radioligand remained intact (>98%) over 48 h. All the three radioligands were stable (>95%) in human plasma over 24 h and even after 48 h, a high fraction of these radioligands were still intact (>93%).

5.3.3 n-Octanol/PBS Distribution Coefficients

All radioligands revealed to be hydrophilic as confirmed by the logD values found to be below -3 (Table 5.2). ^{177}Lu-DOTA-PPB-01 was the least hydrophilic (-3.15 ± 0.04), followed by ^{177}Lu-DOTA-PPB-02 (-4.01 ± 0.03). The logD values of ^{177}Lu-DOTA-PPB-03 and ^{177}Lu-DOTA could not be determined (<-5) as the radioactivity was only detectable in the hydrophilic phase. Based on the statistical analysis the logD values of the three radioligands were significantly different ($p<0.05$).

5.3.4 Determination of Plasma Protein Binding of the Radioligands

The binding capacities of the radioligands as well as of the ^{177}Lu-DOTA complex were evaluated using total human plasma and solutions of the most important proteins including HSA, α_1-AGP and hTTR, which are responsible for drug binding (Figure 5.4 A, Table 5.1). ^{177}Lu-DOTA-PPB-01 bound to a high extent to human plasma (93 ± 1.5%). It was found by the performance of ultrafiltration assays with a solution of HSA (700 µM) only, that the binding to HSA (95 ± 0.6%) was most prominent. ^{177}Lu-DOTA-PPB-01 bound also to α_1-AGP (39 ± 9.6%) as determined by ultrafiltration using an α_1-AGP solution. The binding to hTTR was considered negligible with a bound fraction of only 9.0 ± 1.0%. In the case of ^{177}Lu-DOTA-PPB-02, the plasma protein-bound fraction was with 70 ± 0.6% clearly lower when using full plasma. The bound fraction was, however, increased to 83 ± 0.6% when a HSA solution was used. The binding of ^{177}Lu-DOTA-PPB-02 to α_1-AGP (13 ± 4.5%) and to hTTR (7 ± 2.1%) was very low. ^{177}Lu-DOTA-PPB-03 showed significant binding to human plasma proteins (94 ± 0.6%) in full plasma but when solutions of single plasma proteins were investigated, it was

revealed, that the fraction bound to HSA was only 57 ± 0.6%. The fraction bound to hTTR was, however, 50 ± 0.6%. Binding to α_1-AGP was considered negligible also for this radioligand (4.0 ± 1.1%). Plasma protein binding of ^{177}Lu-DOTA was not observed (<1%) in plasma. Control experiments of the filter assay were performed after incubation of the radioligands in PBS. False positive results due to unspecific binding of the radioligands to the filter membrane were excluded by the fact that all the three radioligands completely passed through the membrane.

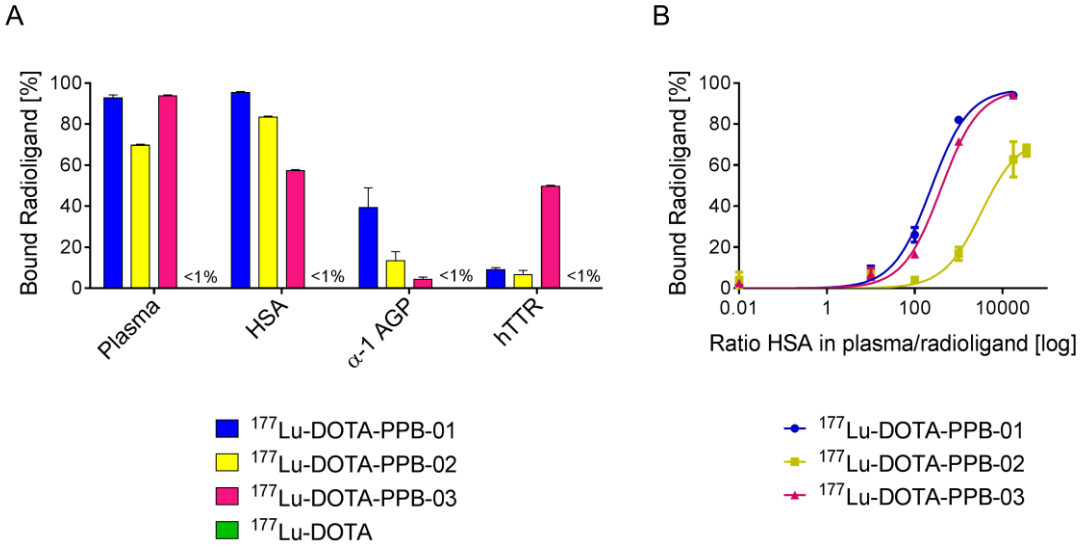

Figure 5.4. (A) Fraction of radioligands bound to proteins in full plasma as well as to specific plasma proteins determined by a filter assay. These values were calculated based on the measurement of the filtered fraction (i.e. free fraction) and expressed as the percentage of the corresponding loading solutions, which were set to 100%. (B) Results of the binding at different ratios between HSA and radioligand revealed relative plasma protein-binding affinities of 0.08 for ^{177}Lu-DOTA-PPB-02 and 0.59 for ^{177}Lu-DOTA-PPB-03 as compared to ^{177}Lu-DOTA-PPB-01 set to 1.

5.3.5 Relative Binding Affinity to Plasma Proteins

The percentage of bound radioligand (^{177}Lu-DOTA-PPB-01, ^{177}Lu-DOTA-PPB-02 and ^{177}Lu-DOTA-PPB-03, respectively) was determined and presented as three different semi-log binding plots (Figure 5.4 B). ^{177}Lu-DOTA-PPB-01 and ^{177}Lu-DOTA-PPB-03 were almost completely bound to plasma proteins (~93% and ~94%, respectively) at the highest ratios of [HSA]/[radioligand] when the concentration of HSA was in the physiological range of 700 µM. Under the same experimental conditions ~70% of ^{177}Lu-DOTA-PPB-02 was bound to HSA. When the HSA concentration was lowered so that the ratio between HSA and the radioligand was 1000, ^{177}Lu-DOTA-PPB-01 and ^{177}Lu-DOTA-PPB-03 were still bound with >80% and >65%, respectively. The binding

of ^{177}Lu-DOTA-PPB-02 was, however, decreased to <20%. Decreasing the ratio between HSA and the radioligand further to 100 resulted in ~30% binding for ^{177}Lu-DOTA-PPB-01 and ~17% binding for ^{177}Lu-DOTA-PPB-03 whereas the binding of ^{177}Lu-DOTA-PPB-02 was <5%. The half-maximum binding (50%) was obtained at [HSA]/[radioligand] ratios of 234, 3270, and 396 for ^{177}Lu-DOTA-PPB-01, ^{177}Lu-DOTA-PPB-02 and ^{177}Lu-DOTA-PPB-03, respectively. The relative plasma protein-binding affinities of ^{177}Lu-DOTA-PPB-02 and ^{177}Lu-DOTA-PPB-03 were 0.08 and 0.59, respectively, as compared to ^{177}Lu-DOTA-PPB-01 which was set to 1 (Table 5.3).

5.3.6 Determination of the Affinity of the Radioligands to HSA and hTTR

The absolute binding affinities (K_D values) of ^{177}Lu-DOTA-PPB-01 and ^{177}Lu-DOTA-PPB-02 to HSA and the affinity of ^{177}Lu-DOTA-PPB-03 to hTTR were determined using an ultrafiltration assay. K_D values of ^{177}Lu-DOTA-PPB-01 (5.0 ± 1.4 μM) and ^{177}Lu-DOTA-PPB-02 (54.1 ± 19.4 μM) for HSA differed by one order of magnitude, however, both values were still in the micromolar range. The K_D value of ^{177}Lu-DOTA-PPB-03 was in the sub-micromolar range (0.425 ± 0.082 μM) with regard to the binding affinity to hTTR.

Table 5.3. Affinity values for total plasma proteins, HSA and hTTR determined by ultrafiltration.

	DOTA-PPB-01	**DOTA-PPB-02**	**DOTA-PPB-03**
Binding to HSA: K_D [μM]	5.0 ± 1.4	54.1 ± 19.4	-
Binding to hTTR: K_D [μM]	-	-	0.425 ± 0.082
Relative plasma protein binding affinity*	1	0.08	0.59

* full plasma involving all plasma proteins

5.3.7 Displacement Experiments using Warfarin and Ibuprofen

The binding of ^{177}Lu-DOTA-PPB-01 to HSA was not significantly reduced when competed with warfarin as shown by the fact that more than 90% of the radioligand was found to be bound (control set as 100%). However, this radioligand was almost

completed displaced when competed with ibuprofen resulting in <20% binding to HSA binding (Figure 5.5 A). ^{177}Lu-DOTA-PPB-02 was displaced ~50% by warfarin, while only ~10% of the compound was bound to HSA when competed with an excess of ibuprofen. In the case of ^{177}Lu-DOTA-PPB-03 about ~50% and <30% was bound when warfarin and ibuprofen, respectively, were used as competitors (Figure 5.5 A).

5.3.8 Displacement Experiments on hTTR using L-Thyroxine

In the absence of L-tyroxine used as a competitor, ~50% of the radioligand was bound to hTTR. The addition of L-tyroxine reduced the binding of ^{177}Lu-DOTA-PPB-03 to 10%. This indicates that ^{177}Lu-DOTA-PPB-03 binds to the same binding pocked of hTTR as does L-tyroxine (Figure 5.5 A).

5.3.9 Displacement Experiments using Plasma Protein-Binding Entities

The ^{177}Lu-DOTA-PPB-01 and ^{177}Lu-DOTA-PPB-02 were displaced from their binding site on HSA resulting in only 14% and <10% bound compound when co-incubated with excess PPB-01 and PPB-02, respectively (Figure 5.5 B). The binding of ^{177}Lu-DOTA-PPB-03 to HSA was not reduced by the addition of excess sPPB-03, indicating that ^{177}Lu-DOTA-PPB-03 does not bind specifically to HSA. However, the binding of ^{177}Lu-DOTA-PPB-03 to hTTR was displaced when it was co-incubated with sPPB-03. Under these conditions less than 10% of the total ^{177}Lu-DOTA-PPB-03 was bound to hTTR (Figure 5.5 B).

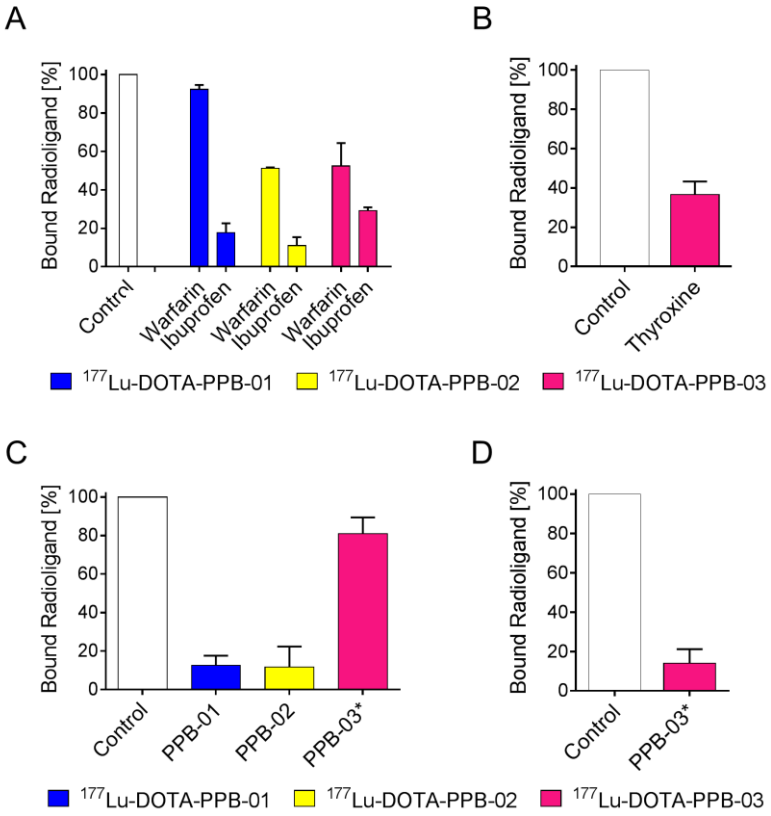

*Figure 5.5. Bound fractions of ^{177}Lu-DOTA-PPB-01, ^{177}Lu-DOTA-PPB-02 and ^{177}Lu-DOTA-PPB-03, respectively, determined after incubation with a 10-fold excess of the competitor for 30 min at 37°C followed by a filter assay and calculated as the percentage of a control experiment (set to 100%) performed without addition of competitor. (A) All three radioligands were incubated with HSA and warfarin and ibuprofen, respectively. In addition, ^{177}Lu-DOTA-PPB-03 was incubated with hTTR and L-thyroxine. (B) All three radioligands were incubated with HSA and PPB-01, PPB-02 and sPPB-03, respectively. In addition, ^{177}Lu-DOTA-PPB-03 was incubated with hTTR and *PPB-03.*

5.3.10 In Vivo Blood Clearance

The pharmacokinetic profile of ^{177}Lu-DOTA-PPB-01, ^{177}Lu-DOTA-PPB-02 and ^{177}Lu-DOTA-PPB-03 were evaluated and compared to the excretion profile of ^{177}Lu-DOTA using normal mice in order to assess how the *in vitro* properties correlate with the *in vivo* pharmacokinetic properties. All three plasma-binding radioligands showed a delayed plasma clearance as compared to ^{177}Lu-DOTA (Figure 5.6). The latter was quickly cleared from the blood, being no longer detectable 2 h after administration. The blood concentration of ^{177}Lu-DOTA-PPB-01 decreased very slowly, showing biphasic pharmacokinetics, well consistent with previous findings [5.19]. Within the first hour period, the radioactivity concentration dropped to 54.0 ± 9.8% IA/2 mL and remained

constant over a long period, showing still 41.6 ± 3.0% IA/2 mL after 8 h. The activity concentration decreased to 19.2 ± 4.1% IA/2 mL and to 7.2 ± 1.0% IA/2 mL after 24 h and 48 h, respectively. After 96 h the blood level of ^{177}Lu-DOTA-PPB-01 (1.0 ± 0.2% IA/2 mL) was negligible and not significantly above the detection limit of the γ-counter. In comparison, ^{177}Lu-DOTA-PPB-02 showed a faster excretion profile over the first hour (26.2 ± 5.2% IA/2 mL at 1 h p.i.), followed by a slow excretion phase resulting in almost complete excretion of the radioligand (0.8 ± 0.2% IA/2 mL) after 8 h. ^{177}Lu-DOTA-PPB-03 was initially cleared very quickly (40.8 ± 5.7% IA/2 mL at 1 h p.i.) followed by a moderate excretion profile as compared to ^{177}Lu-DOTA-PPB-02 resulting in remaining activity concentrations of 14.1 ± 0.9% IA/2 mL at 4 h p.i. and 4.6 ± 3.1% IA/2 mL at 8 h p.i..

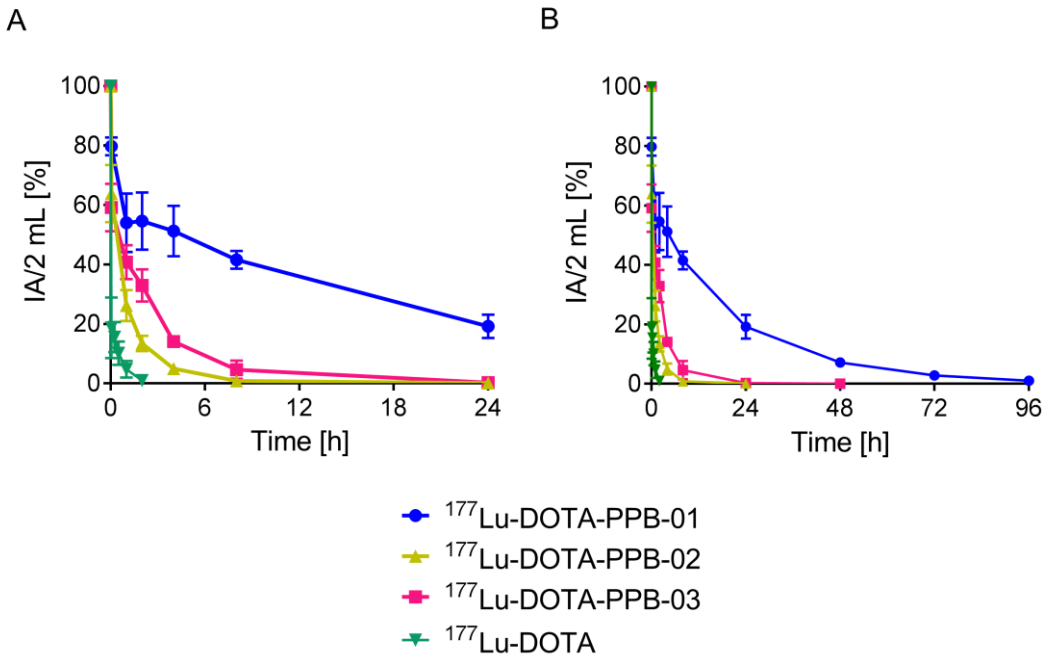

Figure 5.6. Results of the in vivo clearance of ^{177}Lu-DOTA-PPB-01, ^{177}Lu-DOTA-PPB-02, ^{177}Lu-DOTA-PPB-03 and ^{177}Lu-DOTA determined over a period of 24 (A) and 96 (B) hours. The blood concentration is reported as % of the injected activity (%IA). All plasma protein-binding radioligands had significantly longer blood half-lives as compared to the blood half-life of ^{177}Lu-DOTA.

The acquired data were fitted using the *PK solver* software. For all the radioligands the best fit was obtained with a bi-compartmental model. The pharmacokinetic values, $AUC_{0-\infty}$, the $T_{1/2,\ alpha}$ and the $T_{1/2,\ beta}$ were extrapolated from the fitting of the experimentally obtained plasma clearance data (Table 5.4). The $T_{1/2,alpha}$ of the

compounds were not significantly different (<0.05 h for all the radioligands). The $T_{1/2,beta}$ of ^{177}Lu-DOTA-PPB-01 was ~15.8 h, demonstrating a significantly extended circulating time as compared to ^{177}Lu-DOTA which showed a $T_{1/2,beta}$ value of ~0.4 h. The $T_{1/2,\ beta}$ values of ^{177}Lu-DOTA-PPB-02 and ^{177}Lu-DOTA-PPB-03 were ~1.1 h and ~2.3 h, respectively. As a consequence of these different excretion profiles, the $AUC_{0-\infty}$ values were significantly increased in all three cases of plasma protein-binding radioligands as compared to ^{177}Lu-DOTA (~0.1 nmol/mL·h).

Table 5.4. Blood Clearance Parameters Calculated Using PK Solver Software.

Radioligand	$AUC_{0-\infty}$ [nmol/mL·h]	$T_{1/2,\ alpha}$ * [h]	$T_{1/2,\ beta}$* [h]
^{177}Lu-DOTA-PPB-01	7.13 ± 0.64	0.05 ± 0.02	15.83 ± 2.56
^{177}Lu-DOTA-PPB-02	0.40 ± 0.07	0.03 ± 0.01	1.14 ± 0.10
^{177}Lu-DOTA-PPB-03	0.99 ± 0.24	0.01 ± 0.02	2.33 ± 0.44
^{177}Lu-DOTA	0.09 ± 0.04	0.01 ± 0.202	0.48 ± 0.12

* $T_{1/2\ alpha/beta}$ refers to the biological half-lives of the ligands.

5.3.11 SPECT/CT Imaging Studies

SPECT scans were performed 4 h after injection of 20 MBq (1 nmol) of the ^{177}Lu-labeled radioligands (Figure 5.7). The highest retention of activity in the blood pool and the heart was visible in the mouse which received ^{177}Lu-DOTA-PPB-01 (Fig. 5.7 A). ^{177}Lu-DOTA-PPB-02 (Fig. 5.7 B) and ^{177}Lu-DOTA-PPB-03 (Fig. 5.7 C) showed clearly less retention in the blood which was in agreement with the quantitative investigation of the clearance. In contrast to compound ^{177}Lu-DOTA-PPB-03 which was almost entirely excreted 4 h after injection, there was activity visible in the intestinal tract in mice which were injected with ^{177}Lu-DOTA-PPB-02.

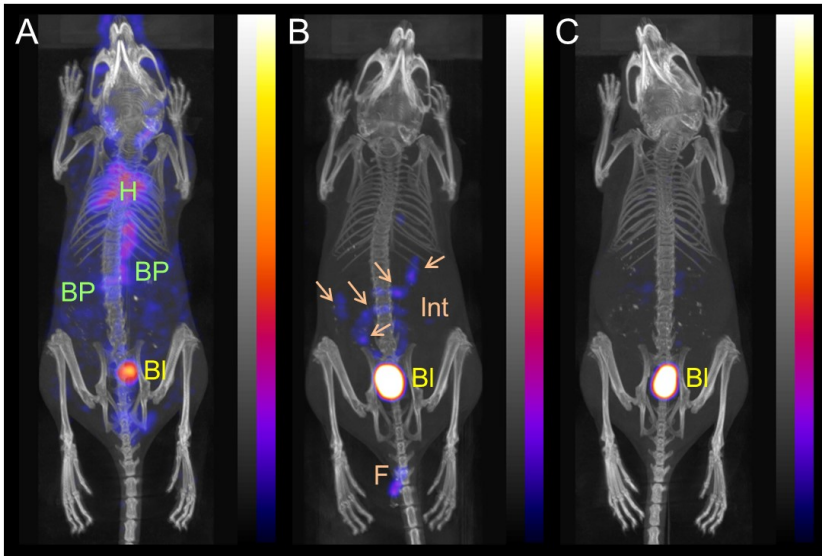

Figure 5.7. Maximal intensity projections (MIPs) of SPECT/CT scans obtained of Balb/c mice 4 h after injection of (A) ^{177}Lu-DOTA-PPB-01, (B) ^{177}Lu-DOTA-PPB-02 and (C) ^{177}Lu-DOTA-PPB-03, respectively. (H: heart; BP: blood pool; Bl: urinary bladder; Int: intestinal tract; F: feces)

5.4 Discussion

In this study, we investigated three different plasma protein-binding entities *in vitro* and *in vivo*. The aim was to compare their characteristics in view of their use for modification of radiopharmaceuticals in order to enhance the blood circulation time.

The radiolabeling of the three DOTA-functionalized plasma protein-binding ligands was achieved at a high specific activity (50 MBq/nmol) with high radiochemical purity (>98%). The stability of the radioligands up to 48 hours was guaranteed when ascorbic acid was added. Based on the *in vitro* results, it appeared that the 4-iodo-phenyl butyric acid group rendered the ^{177}Lu-DOTA-PPB-01 slightly more lipophilic than the other plasma protein binders (Table 5.2). ^{177}Lu-DOTA-PPB-01, carrying the HSA binding entity developed by Dumelin et al. [5.19], proved to bind to a large extent to HSA (~95%) and binding to α_1-AGP (~40%) was also observed. ^{177}Lu-DOTA-PPB-02 bound to a lesser extent to HSA (~84%) and α_1-AGP (~13%), respectively, indicating that the iodine substituent in the aromatic ring is responsible for the enhanced plasma protein binding properties of ^{177}Lu-DOTA-PPB-01. These findings are in agreement with a study in which the replacement of the iodine by an ethynyl group reduced the affinity to the protein of interest significantly even though the ethynyl group was thought to act as a halogen bioisostere [5.22].

The higher extent of binding of ^{177}Lu-DOTA-PPB-02 to pure HSA if compared to full plasma (~83% and ~70%, respectively) could be due to the presence of endogenous ligands in plasma, which can compete and cooperate with drug binding altering binding capacity of HSA [5.27] and to the different HSA concentration that can be in the range of 600 µM to 700 µM in plasma. The binding of ^{177}Lu-DOTA-PPB-03 to full plasma was similar to that of ^{177}Lu-DOTA-PPB-01, however, in this case about 50% of the binding could be ascribed to specific interaction with hTTR whereas the remaining fraction was due to the unspecific interaction with HSA, as discussed later.

Investigations using variable dilutions of full plasma and a fixed amount of radioligand allowed comparison of the three radioligands by presenting the relative affinities (Figure 5.4 B, Table 5.3). ^{177}Lu-DOTA-PPB-01 showed the highest plasma protein binding (relative binding 1.0) whereas the binding affinity of ^{177}Lu-DOTA-PPB-03 (relative binding 0.59) and ^{177}Lu-DOTA-PPB-02 (relative binding 0.08) was clearly reduced as compared to ^{177}Lu-DOTA-PPB-01. These experiments demonstrate that the percentage of plasma protein-bound radioligands is critically dependent on the amount of radioligand as shown in Figure 5.4 B. This should be kept in mind when using radioligands with plasma protein binding entities *in vivo*.

Determination of K_D values using a filter assay revealed a K_D value of 5.0 ± 1.4 µM for ^{177}Lu-DOTA-PPB-01 (Table 5.3), similar to what was determined by Dumelin *et al.* [5.19] who used the method of Isothermal Titration Calorimetry (ITC) for determination of the K_D value of the same albumin-binding entity coupled to acetic acid or 5-carboxyfluoroscein instead of a DOTA chelator. The K_D value of ^{177}Lu-DOTA-PPB-02 for HSA was 10-fold increased (54.2 ± 19.4 µM, Table 5.3) indicating significantly lower binding affinity.

The affinity of ^{177}Lu-DOTA-PPB-03 for hTTR was, however, very high (K_D = 425 ± 82.4 nM, Table 5.3). This value was in line with the literature in which this binding entity was proposed for the first time [5.11]. These findings indicate why the relative binding of ^{177}Lu-DOTA-PPB-03 to plasma proteins (0.59) was higher than for ^{177}Lu-DOTA-PPB-02 (0.08) even though its binding to HSA was weak (~50%; Table 5.3) and unspecific.

The displacement of the radioligands from HSA after the addition of warfarin or ibuprofen, respectively, allowed identification of the preferential Sudlow's binding site I and II, respectively. ^{177}Lu-DOTA-PPB-01 and ^{177}Lu-DOTA-PPB-02 were both

displaced (>90%) by ibuprofen, coherent with extended aromatic conformation of the compounds [5.8]. ^{177}Lu-DOTA-PPB-03 was partially displaced by both warfarin and ibuprofen. Both ^{177}Lu-DOTA-PPB-01 and ^{177}Lu-DOTA-PPB-02 were displaced (>90%) from HSA by their respective binding entities, while ^{177}Lu-DOTA-PPB-03 was only marginally displaced (<20%) by *PPB-03. These findings confirmed that the binding of ^{177}Lu-DOTA-PPB-03 to HSA is mostly due to unspecific interactions. On the contrary ^{177}Lu-DOTA-PPB-03 was, indeed, displaced from hTTR by its binding entity *PPB-03 and by the site-marker thyroxine (>80 and >60%, respectively).

The *in vitro* findings correlated well with the *in vivo* data which showed an enhanced blood clearance for all plasma protein binding compounds as compared to ^{177}Lu-DOTA. ^{177}Lu-DOTA-PPB-01 showed the slowest kinetics in line with the tightest plasma protein-binding properties followed by ^{177}Lu-DOTA-PPB-03 and ^{177}Lu-DOTA-PPB-02. All three plasma protein-binding entities are promising to be used in combination with radiopharmaceuticals and may be employed dependent on the desired modulation of the kinetics.

5.5 Conclusion

Three plasma protein-binding radioligands, potentially useful for modification of radiopharmaceuticals, were evaluated in this study. Our results confirmed the exceptionally high affinity of the 4-iodo-phenyl-butyric acid entity (PPB-01) to HSA while replacement of the halogen by an ethynyl entity (PPB-02) reduced the plasma protein binding significantly. A promising approach is the application of PPB-03 which binds with high affinity to hTTR. The fact that the concentration of plasma proteins may vary between different species and under conditions of inflammation, infection and cancer, should be kept in mind, however, when developing plasma-binding radiopharmaceuticals. This is particularly important for hTTR- and α1-AGP-binding compounds since these proteins are present at significantly lower concentrations as compared to HSA. Future studies in PD Dr. Cristina Müller's laboratory will be focused on the application of these binding entities in combination with clinically relevant targeting agents for diagnostic and therapeutic purposes in nuclear medicine.

References

[5.1] G. Lambrinidis, T. Vallianatou, A. Tsantili-Kakoulidou, *In vitro*, *in silico* and integrated strategies for the estimation of plasma protein binding. A review, Adv. Drug Deliv. Rev. 86 (2015) 27–45. doi:10.1016/j.addr.2015.03.011.

[5.2] D.A. Smith, L. Di, E.H. Kerns, The effect of plasma protein binding on *in vivo* efficacy: misconceptions in drug discovery, Nat. Rev. Drug Discov. 9 (2010) 929–939. doi:10.1038/nrd3287.

[5.3] L. Pollaro, C. Heinis, Strategies to prolong the plasma residence time of peptide drugs, Medchemcomm. 1 (2010) 319. doi:10.1039/c0md00111b.

[5.4] S.B. van Witteloostuijn, S.L. Pedersen, K.J. Jensen, Half-Life Extension of Biopharmaceuticals using Chemical Methods: Alternatives to PEGylation, ChemMedChem. 11 (2016) 2474–2495. doi:10.1002/cmdc.201600374.

[5.5] L. Gentilucci, R. De Marco, L. Cerisoli, Chemical modifications designed to improve peptide stability: incorporation of non-natural amino acids, pseudo-peptide bonds, and cyclization., Curr. Pharm. Des. 16 (2010) 3185–203. http://www.ncbi.nlm.nih.gov/pubmed/20687878.

[5.6] O. Jacobson, D.O. Kiesewetter, X. Chen, Albumin-Binding Evans Blue Derivatives for Diagnostic Imaging and Production of Long-Acting Therapeutics, Bioconjug. Chem. 27 (2016) 2239–2247. doi:10.1021/acs.bioconjchem.6b00487.

[5.7] B. Elsadek, F. Kratz, Impact of albumin on drug delivery - New applications on the horizon, J. Control. Release. 157 (2012) 4–28. doi:10.1016/j.jconrel.2011.09.069.

[5.8] M. Fasano, S. Curry, E. Terreno, M. Galliano, G. Fanali, P. Narciso, S. Notari, P. Ascenzi, The extraordinary ligand binding properties of human serum albumin, IUBMB Life. 57 (2005) 787–796. doi:10.1080/15216540500404093.

[5.9] K. Taguchi, K. Nishi, V. Tuan Giam Chuang, T. Maruyama, M. Otagiri, Molecular Aspects of Human Alpha-1 Acid Glycoprotein — Structure and Function, Acute Phase Proteins. (2013). doi:10.1006/rwcy.2002.0213.2.

[5.10] J.N. Buxbaum, N. Reixach, Transthyretin: the servant of many masters., Cell. Mol. Life Sci. 66 (2009) 3095–101. doi:10.1007/s00018-009-0109-0.

[5.11] S.C. Penchala, M.R. Miller, A. Pal, J. Dong, N.R. Madadi, J. Xie, H. Joo, J. Tsai, P. Batoon, V. Samoshin, A. Franz, T. Cox, J. Miles, W.K. Chan, M.S. Park, M.M. Alhamadsheh, A biomimetic approach for enhancing the *in vivo* half-life of

peptides, Nat. Chem. Biol. 11 (2015) 793–798. doi:10.1038/nchembio.1907.

[5.12] W.J.G. Oyen, L. Bodei, F. Giammarile, H.R. Maecke, J. Tennvall, M. Luster, B. Brans, Targeted therapy in nuclear medicine - Current status and future prospects, Ann. Oncol. 18 (2007) 1782–1792. doi:10.1093/annonc/mdm111.

[5.13] R. Meredith, B. Wessels, S. Knox, Risks to Normal Tissues From Radionuclide Therapy, Semin. Nucl. Med. 38 (2008) 347–357. doi:10.1053/j.semnuclmed.2008.05.001.

[5.14] C. Müller, K. Zhernosekov, U. Koster, K. Johnston, H. Dorrer, A. Hohn, N.T. van der Walt, A. Turler, R. Schibli, A Unique Matched Quadruplet of Terbium Radioisotopes for PET and SPECT and for - and --Radionuclide Therapy: An *In Vivo* Proof-of-Concept Study with a New Receptor-Targeted Folate Derivative, J. Nucl. Med. 53 (2012) 1951–1959. doi:10.2967/jnumed.112.107540.

[5.15] K. Siwowska, S. Haller, F. Bortoli, M. Benešová, V. Groehn, P. Bernhardt, R. Schibli, C. Müller, Preclinical comparison of albumin-binding radiofolates: Impact of linker entities on the *in vitro* and *in vivo* properties, Mol. Pharm. 14 (2017) 523–532. doi:10.1021/acs.molpharmaceut.6b01010.

[5.16] M. Meckel, V. Kubíček, P. Hermann, M. Miederer, F. Rösch, A DOTA based bisphosphonate with an albumin binding moiety for delayed body clearance for bone targeting, Nucl. Med. Biol. 43 (2016) 670–678. doi:10.1016/j.nucmedbio.2016.07.009.

[5.17] J.M. Kelly, A. Amor-Coarasa, A. Nikolopoulou, T. Wüstemann, P. Barelli, D. Kim, C. Williams, X. Zheng, C. Bi, B. Hu, J.D. Warren, D.S. Hage, S.G. DiMagno, J.W. Babich, Dual-Target Binding Ligands with Modulated Pharmacokinetics for Endoradiotherapy of Prostate Cancer., J. Nucl. Med. 58 (2017) 1442–1449. doi:10.2967/jnumed.116.188722.

[5.18] C.J. Choy, X. Ling, J.J. Geruntho, S.K. Beyer, J.D. Latoche, B. Langton-Webster, C.J. Anderson, C.E. Berkman, ^{177}Lu-labeled phosphoramidate-based PSMA inhibitors: The effect of an albumin binder on biodistribution and therapeutic efficacy in prostate tumor-bearing mice, Theranostics. 7 (2017) 1928–1939. doi:10.7150/thno.18719.

[5.19] C.E. Dumelin, S. Trüssel, F. Buller, E. Trachsel, F. Bootz, Y. Zhang, L. Mannocci, S.C. Beck, M. Drumea-Mirancea, M.W. Seeliger, C. Baltes, T. Müggler, F. Kranz, M. Rudin, S. Melkko, J. Scheuermann, D. Neri, A portable

albumin binder from a DNA-encoded chemical library, Angew. Chemie - Int. Ed. 47 (2008) 3196–3201. doi:10.1002/anie.200704936.

[5.20] S. Trüssel, C. Dumelin, K. Frey, A. Villa, F. Buller, D. Neri, New Strategy for the Extension of the Serum Half-Life of Antibody Fragments, Bioconjug. Chem. 20 (2009) 2286–2292. doi:10.1021/bc9002772.

[5.21] C. Müller, H. Struthers, C. Winiger, K. Zhernosekov, R. Schibli, DOTA conjugate with an albumin-binding entity enables the first folic acid-targeted ^{177}Lu-radionuclide tumor therapy in mice., J. Nucl. Med. 54 (2013) 124–131. doi:10.2967/jnumed.112.107235.

[5.22] R. Wilcken, M.O. Zimmermann, M.R. Bauer, T.J. Rutherford, A.R. Fersht, A.C. Joerger, F.M. Boeckler, Experimental and Theoretical Evaluation of the Ethynyl Moiety as a Halogen Bioisostere, ACS Chem. Biol. 10 (2015) 2725–2732. doi:10.1021/acschembio.5b00515.

[5.23] S.C. Penchala, M.R. Miller, A. Pal, J. Dong, N.R. Madadi, J. Xie, H. Joo, J. Tsai, P. Batoon, V. Samoshin, A. Franz, T. Cox, J. Miles, W.K. Chan, M.S. Park, M.M. Alhamadsheh, A biomimetic approach for enhancing the *in vivo* half-life of peptides, Nat. Chem. Biol. 11 (2015) 793–798. doi:10.1038/nchembio.1907.

[5.24] C. Müller, R. Farkas, F. Borgna, R.M. Schmid, M. Benešová, R. Schibli, Synthesis, Radiolabeling, and Characterization of Plasma Protein-Binding Ligands: Potential Tools for Modulation of the Pharmacokinetic Properties of (Radio)Pharmaceuticals, Bioconjug. Chem. 28 (2017). doi:10.1021/acs.bioconjchem.7b00378.

[5.25] C. Müller, T.L. Mindt, M. de Jong, R. Schibli, Evaluation of a novel radiofolate in tumour-bearing mice: promising prospects for folate-based radionuclide therapy, Eur. J. Nucl. Med. Mol. Imaging. 36 (2009) 938–946. doi:10.1007/s00259-008-1058-9.

[5.26] Y. Zhang, M. Huo, J. Zhou, S. Xie, PKSolver: An add-in program for pharmacokinetic and pharmacodynamic data analysis in Microsoft Excel, Comput. Methods Programs Biomed. 99 (2010) 306–314. doi:10.1016/j.cmpb.2010.01.007.

[5.27] J. Ghuman, P.A. Zunszain, I. Petitpas, A.A. Bhattacharya, M. Otagiri, S. Curry, Structural basis of the drug-binding specificity of human serum albumin, J. Mol. Biol. 353 (2005) 38–52. doi:10.1016/j.jmb.2005.07.075.

Chapter 6

Preliminary *in vitro* evaluation of TKIs-^{177}Lu-folate combination therapy in FR-positive cancer cells

6.1 Introduction

Cancer onset, progression and metastasis can be due to alterations in the cell cycle [6.1], and it is nowadays known that a key role in cell cycle regulation is played by tyrosine kinases (TKs) [6.2,6.3]. These proteins act as catalyzers of reaction where a phosphate molecule is transferred from an ATP molecule to a tyrosine residue of a target protein, thus leading to signal transduction. They can be receptor TKs (RTKs), as the epidermal growth factor receptor (EGFR), the fibroblast growth factor receptor 1 (FGFR-1), the vascular endothelial growth factor receptor 1 and 2 (VEGFR-1 and 2) and the platelet-derived growth factor receptor β (PDGFR-β), and cytoplasmic TKs, as Src, Abl and Lck [6.4]. The final effect of RTKs activation is cell growth stimulation and division [6.5]. While in healthy cells TKs activity is strictly regulated so that cell proliferation and apoptosis are balanced, in several cancer tissues TKs are up-regulated or undergo gain-of-function mutations [6.6,6.7]. For these reasons, TKs have been regarded as suitable molecular targets for cancer treatment and several inhibitors have been developed. They can be classified into two classes: (*i*) small organic compounds (TKIs) that act as ATP-mimicking inhibitors or growth factors binders, inhibiting this way the binding of ATP; (*ii*) monoclonal antibodies (mAbs) that act as growth factor-mimicking inhibitors and preventing this way RTK activation [6.8,6.9].

The blockage of tyrosine kinases signal has been reviewed as a valuable strategy for enhancing external beam radiotherapy efficacy in tumors [6.10]. In particular it was shown in previous studies that combination of EGFR inhibitors could enhance radiotherapeutic effect [6.11]. It is known that EGFR overexpression generally correlates with decreased survival, resistance to radiotherapy and treatment failure [6.12]. It was also demonstrated that the downstream signal of EGFR directly increases

radiation resistance in tumor cells, because radiation induces the release of EGFR ligands and thus the signaling that results in the activation of transcription factors responsible for enhanced tumor survival and DNA repair [6.13–6.15]. Going more into detail, the mechanism of EGFR inhibition and the possible mechanism underlying the radio sensitizing effect has been reviewed by Zheng *et al*. [6.16]. The cell response to radiation can be summarized in the 4Rs: repair of radiation damage, redistribution, reoxygenation, and repopulation [6.17]. EGFR inhibitors have been suggested to play a role in all these 4 mechanisms: (*i*) inhibition of DNA damage repair, (*ii*) blocking the cell in the G1 phase, not allowing redistribution, and prolongation in the radiation-induced G2 phase, (*iii*) inhibition of pro-survival downstream pathways PI3K/AKT and RAS/RAF/MEK/MAPK, and (*iv*) inhibition of reoxygenation through the blocking of tumor neo-angiogenesis [6.18].

Inhibition of PDGFR, another RTK, was also demonstrated to specifically increase cytotoxicity in glioblastoma cells treated with external radiations. The downstream mechanisms underlying this effect are unknown, but a possible way is the activation by PDGFR of Stat5 which is implicated in radioresistance in Bcr-Abl-expressing cells [6.19,6.20].

Radiosensitivity depends on intrinsic and extrinsic factors to cancer cells [6.21] and the modulation of tumor microenvironment is a strategy to increase radiation responsiveness [6.22]. Inhibition of PDGFR-β for example is related to the decrease in the interstitial pressure in solid tumors, thus facilitating the cellular up-take of cytotoxic agents, including for example radiopharmaceuticals [6.23,6.24].

For all the aforementioned reasons, it is rational to develop a combination therapy using TKIs and internal radiation therapy. Moreover, the use of combined-modality regimens in cancer therapy is a valuable strategy to overcome the emergence of resistance to therapy [6.25]. Targeting the cancer cell on diverse molecular path mechanisms makes the cell less prone to developing survival mechanisms. At the same time, the use of multimodality therapies allows to decrease the dosage of single therapies, thus reducing side-effects.

In this study, in particular, we preliminarily investigated the combination of two TKIs, imatinib and G475, with a therapeutic radiofolate, ^{177}Lu-cm10 [6.26]. The combination was tested on folate positive tumor cells, namely KB and IGROV-1, cervical and ovarian cancer cell lines, respectively.

Imatinib, structure in figure 6.1, is a small molecule that selectively inhibits the catalytic action of c-Abl kinase, stem cell factor receptor (c-Kit) and PDGFR tyrosine kinase. Its use is approved in the clinics for the treatment of patients suffering from chronic myeloid leukemia and gastrointestinal stromal tumors, where its targets are constitutively activated [6.27]. Since protein kinases are frequently deregulated in several tumor types, its use is currently under investigation in other tumor types. In particular PDGF family members play an important role in meningiomas, gliomas, melanomas, neuroendocrine tumors, sarcomas and ovarian, pancreatic, gastric, lung breast and prostate carcinomas [6.28–6.30].

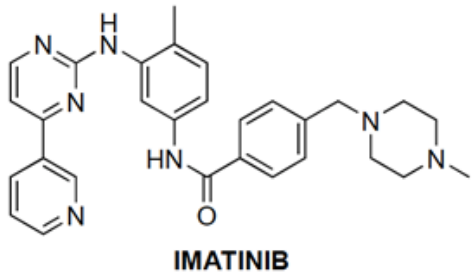

Figure 6.1. Chemical structure of imatininb.

G475, figure 6.2, is a novel quinazoline-based multi-tyrosine kinase inhibitor, developed by a team of the Department of Pharmaceutical and Pharmacological Sciences of the University of Padova [6.9]. This compound was selected as one of the most promising ones for its multi-targeting capacity and cell-death induction on a panel of cells. In particular, G475 targets EGFR, FGFR-1, PDGFR-β and Abl [6.9]. Its IC_{50} values on a panel of tumor cell lines derived from breast (MCF-7) and colon (HT-29) carcinomas, cervical cancer (HeLa), and from murine hepatocellular carcinoma (BNL 1 ME A.7R.1), were in the low micromolar range.

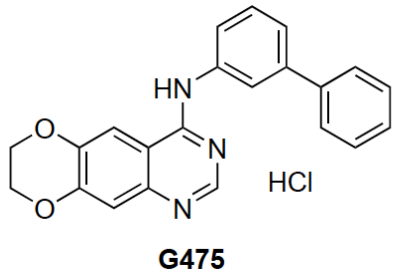

Figure 6.2. Chemical structure of G475 [6.9].

^{177}Lu-cm10, figure 6.3, is a therapeutic radiofolate developed in the group of PD Dr. Cristina Müller [6.26] for the treatment of folate receptor α (FR) positive cancer cells. The FR is expressed on a variety of tumor types (e.g. ovarian, endometrial, lung cancer, etc. [6.31]) and for this reason it is regarded as a promising tumor target in targeted therapy (TRT).

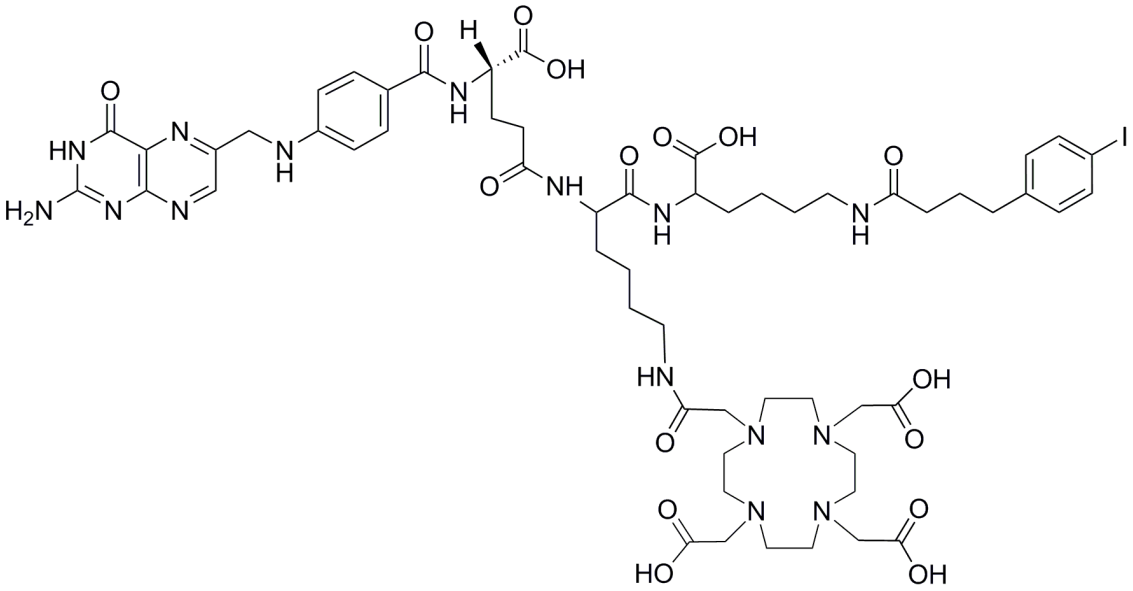

Figure 6.3. Chemical structure of cm10 [6.26].

The vitamin, folic acid, has been derivatized and used as a diagnostic tool with radionuclides in the clinics and as therapeutic probe in preclinical studies [6.26,6.32,6.33]. The translation to the clinics of radiofolate therapy has been hindered by the nephrotoxicity of this therapy, due to the overexpression of the FR in the kidneys and its renal clearance [6.34]. Several strategies are under development to overcome this issue, one of these is the development of combination therapies, which could allow the administration of a lower dose of radionuclides to patients, thus reducing side effects.

The cell lines used in this study, KB and IGROV-1, overexpressing the folic acid receptor, were extensively studied and characterized, and they were proved to be suitable for preclinical investigations in FR-targeting research over a panel of FR positive cell lines [6.35].

The TKs overexpression of the tested cell lines, KB and IGROV-1, was checked using the database GENEVESTIGATOR, which allows to check the gene overexpression profile in several cell types [6.36]. This allowed to verify if the molecular targets of imatinib and G475 were overexpressed on the tested cell lines. KB cells were found to

highly overexpress EGFR and Abl, and had a medium expression of PDGFR-β, FGFR1 and c-Kit. IGROV-1 cells have a high expression of EGFR, FGFR-1 and Abl, and a medium expression of PDGFR-β and c-Kit.

In this very preliminary study we tested first the single agents, imatinib, G475 and ^{177}Lu-cm10, on the selected cell lines, KB and IGROV-1, and afterwards we combined the TKIs and radionuclide therapy. For the evaluation of cells viability, we used a colorimetric (MTT) assay.

6.2 Materials and Methods

All reagents and solvents were purchased from Sigma-Aldrich. All chemicals used for the radiolabeling were metal-free and obtained from Sigma-Aldrich (Germany) in Suprapur quality. Analytical radio-HPLC was performed on a Merck-Hitachi HPLC equipped with a L-6200A pump, a L-3000 Photo Diode Array detector and a Berthold LB 508 radiometric detector. For this purpose, a reversed-phase C18 column (5 µm, 4.6 mm x 150 mm, XTerra^{TM} MS, Waters, USA) was used. The ligand cm10 was synthetized in the group of PD Dr. Cristina Müller, while imatinib and G475 were synthetized in the group of Prof. Giovanni Marzaro (UniPD). The experiments with the cells were performed in duplicates, with the exception of the combination therapy, which were performed only once and for this reason the results are given as indicative values only.

6.2.1 Preparation of radioligands

Radiolabeling of cm10 was performed at a specific activity (Sp. Act.) of 50 MBq/nmol. ^{177}Lu in HCl 0.05 M, obtained from Isotope Technologies Garching ITG GmbH, was added to sodium acetate 0.5 M, pH 8.0, in a ratio of 5:1, to a final pH of ~4.5. After mixing, the folate was added (1 mM stock solution) and the reaction vial was incubated for 10 minutes, 95 °C. Quality control of ^{177}Lu-cm10 was carried out by reversed-phase high-performance liquid chromatography (RP-HPLC) analysis (Merck LaChrom HPLC) using a C18 column (5 µm, 4.6 mm x 150 mm, XTerra^{TM} MS, Waters USA). The eluent consisted of acetonitrile (solvent A) and 0.1% TFA in H_2O (solvent B). A gradient of 5-80% A and 95-20% B was used over 15 min at a flow rate of 1.0 mL/min. 5 µL of Na-DTPA (5 mM), for the complexation of unreacted ^{177}Lu, were added to the

radioligand, before dilutions for cell experiments. Radiolabeling of ^{177}Lu-DTPA was carried out as for cm10, but after preparing the reaction mixture (^{177}Lu in HCl 0.05 M and Na-Acetate 0.5 M) Na-DTPA 5 mM was added in a ligand/radionuclide ratio of ~150.

6.2.2 Cell lines and cell culture

FR-overexpressing cell lines (KB and IGROV-1) were cultured in folate-deficient RPMI medium (FFRPMI, Cell Culture Technologies GmbH, Gravesano, Switzerland) supplemented with 10% fetal calf serum, L-glutamine, and antibiotics. Routine cell culture was performed twice a week using trypsin for detachment of the cells.
KB cells (cervical carcinoma cell line, subclone of HeLa cells, ACC-136) were purchased from the German Collection of Microorganisms and Cell Cultures (DSMZ, Germany). IGROV-1 cells (human ovarian carcinoma cell line) were a kind gift of Dr. Gerrit Jansen (Department of Rheumatology, Free University Medical Center, Amsterdam, The Netherlands).

6.2.3 Dilutions of imatinib and G475

Stock solutions of imatinib and G475 were prepared weekly at the concentration of 50 mM in dimethyl sulfoxide (DMSO). For cell experiments the stock solutions were diluted to 500 μM (dilution 1:100) in water with the addition of DMSO to avoid the compounds precipitation. Briefly, 40 μL of stock solution were diluted with 60 μL of DMSO and then 3.9 mL of water were slowly added, mixing the solution with the tip. These solutions were then filtered through 0.22 μm sterile filters and thus sterilized. Further dilutions were then performed with sterile medium to the desired concentrations.

6.2.4 Evaluation of anti-proliferative activity of TKIs

Cells were seeded into 96-well plates (2500 cells per well in a volume of 200 μL). After 24 h of incubation, the medium was removed and replaced with various concentrations of the tested compounds, 1 and 10 μM for G475 and 1, 10, 50 and 100 μM for imatinib, diluted in medium. Control cells were supplemented with fresh medium. The compounds were left on the cells for 1, 2, 3, 4, 5 and 6 days, incubating the plates at 37

°C, 5% CO_2. In each plate also blank wells, where no cells were added, were treated equally to control wells.

After the incubation period, 30 µL of thiazolyl blue tetrazolium bromide (MTT) reagent (5 mg/mL, Sigma Aldrich) were added to each well and incubated for 3-5 hours, 37 °C, 5% CO_2. The supernatant was removed, and the crystals dissolved adding 200 µL of DMSO. Color intensity was measured in a microplate reader, λ=560 nm (PerkinElmer, VICTOR X). Blank absorbance was subtracted from test wells intensities and control set as 100 %.

6.2.5 Evaluation of anti-proliferative activity of ^{177}Lu-cm10 and ^{177}Lu-DTPA

The cells (KB and IGROV-1) were seeded out in the same conditions as described in 6.2.3. The radioligands were prepared as described in 6.2.1 and diluted before incubation on the cells. For KB cells ^{177}Lu-cm10 and ^{177}Lu-DTPA were diluted in medium without additives and incubated on the cells at an activity concentration of 0.01, 0.05 and 0.15 MBq/mL. For IGROV-1 they were diluted to 5, 15 and 30 MBq/mL.

After removing the medium, the cells were washed with 200 µL PBS and the diluted radioligands were added and incubated for 4 hours at 37 °C, 5% CO_2. After the incubation period, the cells supernatant was removed, the cells washed with PBS (200 µL) and finally fresh medium (200 µL) was added. The cells were then incubated for 4 days, 37 °C, 5% CO_2. The MTT reagent was then added and the plates developed as described in paragraph 6.2.3 for cell viability measurements.

6.2.6 Evaluation of ^{177}Lu-cm10-TKIs combination

To evaluate the synergistic effect of ^{177}Lu-cm10 and imatinib or G475 therapy, KB and IGROV-1 cells were seeded out as previously described (§ 6.2.3). Activity was incubated and left on the cells for 4 hours, 0.10 MBq/mL and 5 MBq/mL on KB and IGROV-1, respectively. After washing the cells, imatinib or G475 were incubated in a range of concentrations from 1-100 µM and 1-1000 nM, respectively, and left for 4 days. After the period of incubation, the cells were treated as described in § 6.2.3 for MTT development.

6.2.7 Cell-uptake studies

KB and IGROV-1 cells were seeded out into 12-well plates (700'000 cells per well) and let to grow overnight. After removing the medium, the cells were washed with PBS and G475 or imatinib were added to the cells (975 μL, 0.1-10 μM and 50-100 μM, respectively) and incubated for 10 min. 975 μL of medium were added to control wells. Finally, ^{177}Lu-cm10 (25 μL, 1.5 MBq/mL, Sp. Act. 50 MBq/nmol) was added to each well and plates were incubated at 37 °C, 5% CO_2. After 1 or 4 hours the supernatant was discarded, cells washed with cold PBS (3x), lysed with NaOH (1 M, 1 mL) and transferred to RIA tubes for measurement in a γ-counter (PerkinElmer Wallac Wizard 1480). After homogenization of the cell suspensions by vortexing, the concentration of proteins was determined for each sample using a Micro BCA Protein Assay Kit (Pierce, Thermo Scientific) in order to standardize the measured radioactivity to the average content of protein (0.3 mg) in a single well. The results were expressed as the percentage of total added radioactivity.

6.3 Results

6.3.1 Preparation of radioligand

^{177}Lu-cm10 could be prepared with high radiochemical purity (>99.5%). The radioligand was eluted with a retention time of 9.6 min, and no scavenger was added to guarantee stability, as it was previously demonstrated that it was stable (>95%) over 4 hours [6.26].

6.3.2 Evaluation of anti-proliferative activity of TKIs

Anti-proliferative activity was evaluated with MTT assay on both cell lines with imatinib and G475, alone. The inhibitors were left on the cells from 1 to 6 days, in order to evaluate the time necessary to induce cell death. Both inhibitors were initially tested at 1 and 10 μM concentration, and afterwards imatinib was tested at 50 and 100 μM, as well, since the lower concentrations were not effective (figure 6.4).

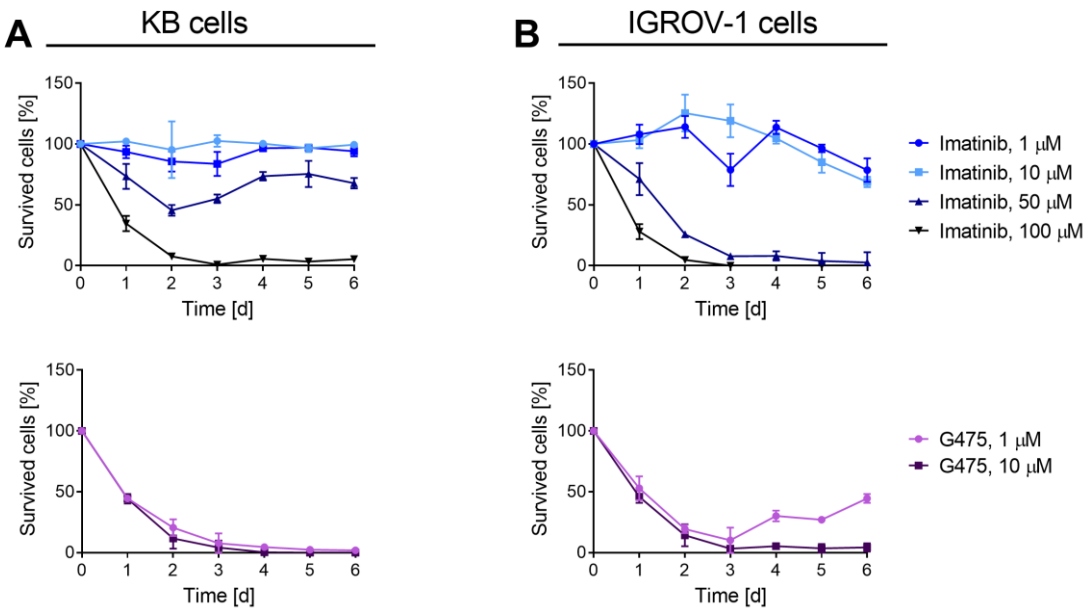

Figure 6.4 Results of MTT assay on KB (A) and IGROV-1 (B) cells after treatment with imatinib and G475.

KB cells were not affected by imatinib when its concentration was 1 or 10 μM, with % of viable cells not distinguishable from controls. When the imatinib concentration was increased to 50 and 100 μM, ~70 and 35% of cells, respectively, were alive after 1 day of treatment. When the treatment was imatinib 50 μM, ~50% of cells was still alive after 2 days, and this percentage increased after 3, 4, and 5 days with a percentage of viable cells of 55.07 ± 3.5%, 73.57 ± 3.6% and 75.49 ± 10.8%, respectively. In the plates treated with imatinib 100 μM, the cell number was drastically decreased after two and three days (7.69 ± 0.3% and <1%, respectively). A weak recovery could be observed after day 5 and 6 (3.48 ± 0.8% and 5.42 ± 0.6%).

IGROV-1 cells were more sensitive to imatinib than KB when the same inhibitor concentrations were applied. At 50 μM after 1 day of treatment 70% of cells were alive, but this number decreased dramatically to 25.9 ± 2.9% and 7.86 ± 2.9% after 2 and 3 days of treatment. In this case no cell recovery was observed. The highest concentration of imatinib (100 μM) killed irreversibly all the cells after 2 and 3 days 4.82 ± 0.2% and 0.09 ± 0.1%.

Both cell lines proved to be very sensitive to G475, with ~50% of survived cells after 1 day of treatment, independently on the applied concentration (1 or 10 μM). ~20% of KB cells were alive after 3 days, with this value slowly decreasing to 1.90 ±1.3% after 6 days of treatment with G475 1 μM. The same trend was observed with the highest

concentration, with only ~12% of cells alive after 2 days and <1% after 4 days. Cell survival for IGROV-1 was <5% after 3 days of treatment with G475 10 μM, while a slow recovery was observed with 1 μM treatment: 10.2 ± 10.5%, 30.3 ± 4.4%, 27.1 ±2 % and 44.5 ±3.7 % after 3, 4, 5 and 6 days, respectively.

The values of absorbance of control wells were measured in time, in order to check their growth, figure 6.5. After 4 days from the seeding out, the cells reached the plateau; for this reason, for IC_{50} determination, plates were measured after 4 days of incubation.

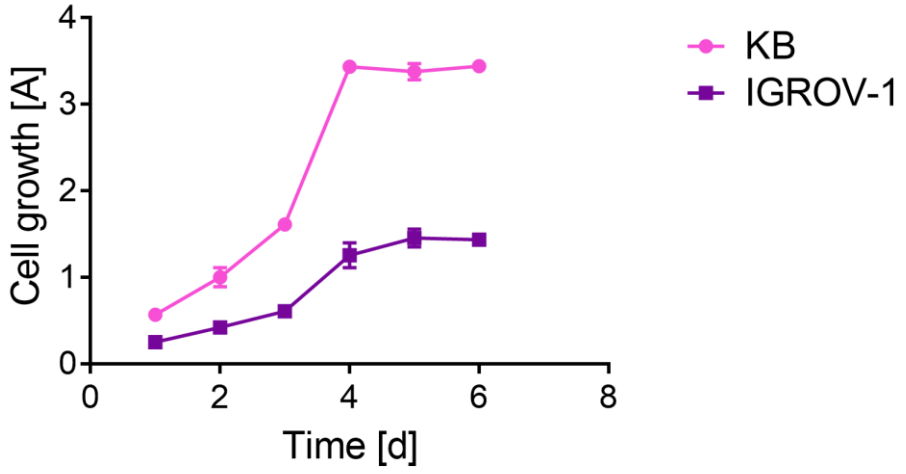

Figure 6.5. Control cells growth.

The IC_{50} of imatinib could not be accurately defined, because in these assays even when the highest concentration of compound was applied on the cells (100 μM), ~40% of the cells were still alive. Higher concentrations of the compound were not prepared to avoid the precipitation in the medium. For IGROV-1, instead, the value was determined and was found to be 64.63 ±8.4 μM. The IC_{50} of G475 on KB and IGROV-1 was in the low micromolar range, ~0.16 and 0.26 μM, respectively.

6.3.3 Evaluation of anti-proliferative activity of ^{177}Lu-cm10 and ^{177}Lu-DTPA

To evaluate the proper radioactivity concentration to incubate with cells in the combination therapy, a preliminary assay with ^{177}Lu-cm10 alone was carried out. The use of the radioligand ^{177}Lu-cm10, which is known to be internalized into the FR+ cells [6.26], was also compared to ^{177}Lu-DTPA, which is not internalized (figure 6.6).

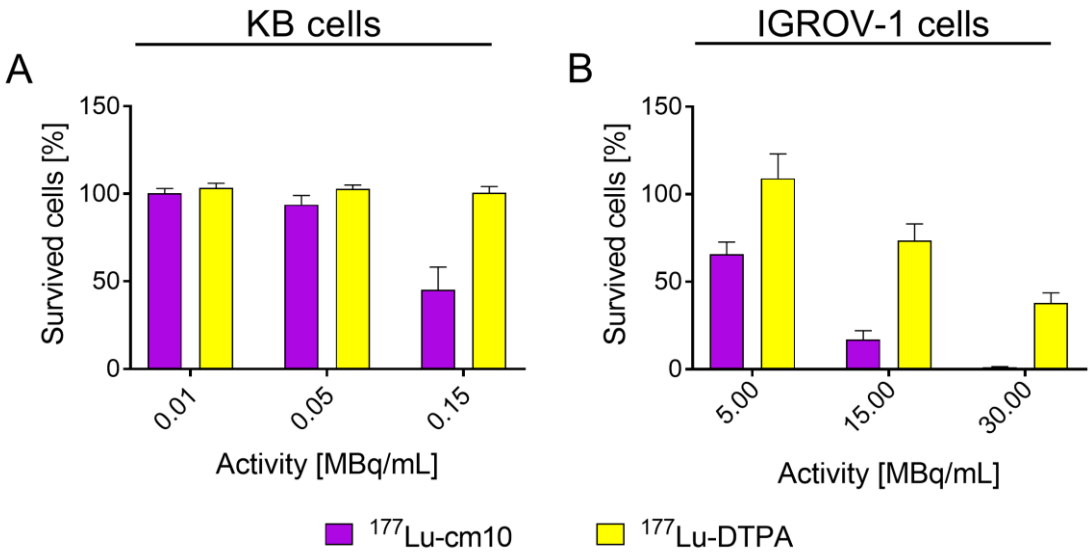

Figure 6.6. Results of MTT assays on KB (A) and IGROV-1 (B) cells after incubation of cells with ^{177}Lu-cm10 or ^{177}Lu-DTPA.

KB cells were incubated with ^{177}Lu-cm10 or ^{177}Lu-DTPA at the concentrations of 0.01, 0.05 and 0.15 MBq/mL. At the lowest radioactivity concentration, no cell death was observed in the cells treated with either ^{177}Lu-cm10 or ^{177}Lu-DTPA. ^{177}Lu-DTPA was not able to induce cell death even at the highest activity concentration (0.15 MBq/mL), conditions that enabled ^{177}Lu-cm10 to kill ~55% of cells.

IGROV-1 cells were incubated with ^{177}Lu-cm10 or ^{177}Lu-DTPA at the concentration of 5, 15 and 30 MBq/mL of activity. When the lowest concentration was applied, ~65% of cells were alive if the radiofolate was used, while no cell death was observed with ^{177}Lu-DTPA. At 15 and 30 MBq/mL of radiofolate only 17.1 ± 4.9% and 1.1 ± 0.4%, respectively, survived. A higher survival rate at these concentrations was observed for cells treated with ^{177}Lu-DTPA, 73.6 ± 9.5% and 37.8 ± 5.9%.

6.3.4 Combination therapy

The effect after combining ^{177}Lu-cm10 and one of the two inhibitors was evaluated. In all cases a sum effect was observed. In particular, for IGROV-1 we could measure a change in the IC_{50} values with both compounds. IC_{50} of imatinib on IGROV-1 was ~64 μM, this value was reduced, even if not significantly, to 50.70 ±17.0 μM, when also ^{177}Lu-cm10 was applied on the cells, see figure 6.7.

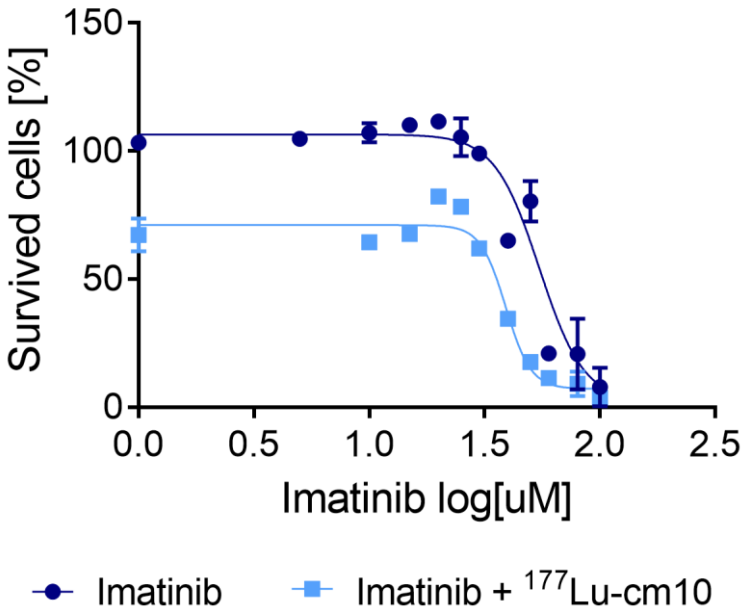

Figure 6.7. Curve of cell survival for IGROV-1 with imatinib alone and in combination with ^{177}Lu-cm10.

In the case of G475 on IGROV-1 cells the value was changed from ~260 nM to ~215 nM. On KB cells the use of both agents on the cells was influenced by the strong effect of radiation that in these experiments caused the death of ~70% of cells, differently from what was expected. For this reason, it was not possible to determine accurately the new IC_{50} values. Nevertheless, it was observed that when imatinib was 1 μM only ~9.8% of cells were alive, so the effect was summed to that of radiation alone. Moreover, at this concentration imatinib alone was not effective. G475 combined with ^{177}Lu-cm10, caused the death of >90% of KB cells when the inhibitor was applied at the concentration of 100 nM. This concentration of inhibitor alone was not able to induce significantly different cell death from untreated wells.

6.3.5 Cell-uptake studies

To verify that no interference in the cell-uptake of the radiofolate could happen because of the presence of either imatinib or G475 on the cells, uptake studies were carried out comparing cells where only the radiofolate was added, with cells where imatinib (50 or 100 μM) or G475 (0.1 or 10 μM) was previously added, figure 6.8.

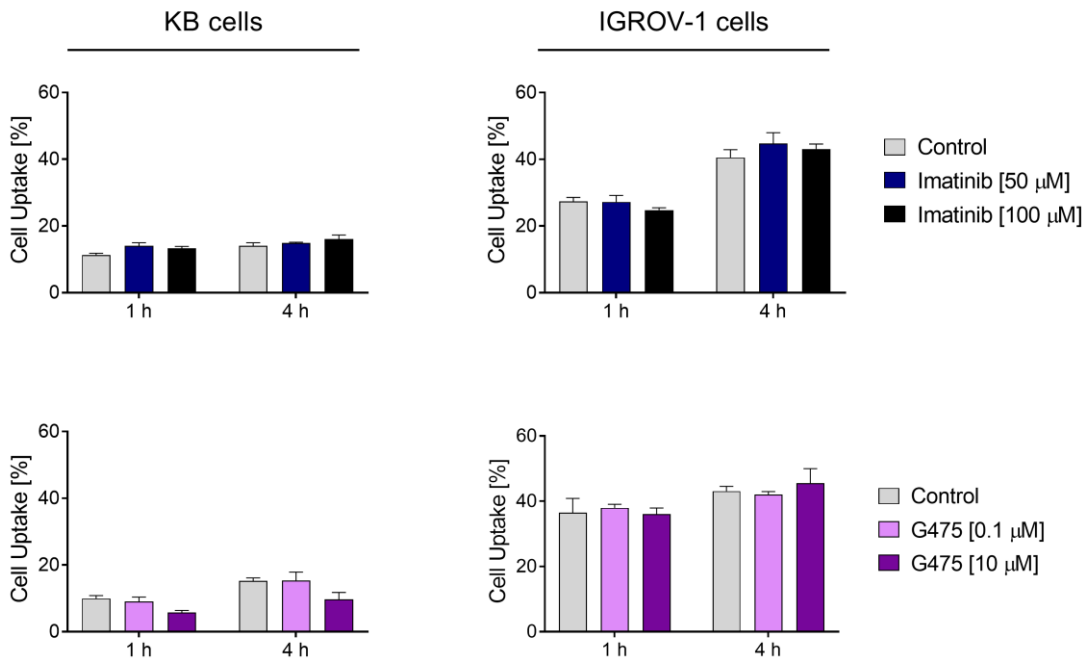

Figure 6.8. Results of the up-take studies on KB (upper part) and IGROV-1 (on the bottom) cells.

The uptake of ^{177}Lu-cm10 on both KB and IGROV-1 cells was not influenced when imatinib was added. No significant difference could be observed between control and treated cells after 1 and 4 hours of incubation. G475 did not influence the uptake of the radiofolate on IGROV-1 cells, while a slight decrease was observed in KB cells at the higher inhibitor concentration (10 μM), ~58 and 63% of controls after 1 and 4 hours, respectively.

6.4 Discussion

Small molecule-based radionuclide therapy is a valuable tool for the delivery of cytotoxic doses of radiations selectively to tumor tissues [6.37]. The success of the therapy can be limited by the accumulation of radioactivity into undesired tissues, like the kidneys as in the case of folic acid [6.34]. The development of combined regimens therapy is a valuable tool to decrease the single agent amounts, thus reducing side effects.

In this study we preliminary evaluated *in vitro* the combination therapy of a therapeutic radiofolate, ^{177}Lu-cm10, with two multi-tyrosine kinases inhibitors, imatinib and G475 on KB and IGROV-1 cells. We first evaluated the efficacy of the single agents on the

cells. Imatinib was found to be effective at concentrations >50 μM, while G475 had IC_{50} values in the low micromolar range, in agreement with previously published data. The difference between the potency of the two agents might be due to the different overexpression of the molecular targets of the two inhibitors. Further studies in our laboratory will be dedicated to the accurate study of the tyrosine kinases overexpression of the cells lines. Further investigations will also be carried out to study the cell cycle arrest, in order to determine the mechanism of action of the compounds on these peculiar cell lines. The cell cycle arrest studies will also be useful to understand the possible synergistic effect with radiations.

Very preliminary assays, where imatinib or G475 and ^{177}Lu-cm10 were both incubated on the cells, were carried out. These assays could not give a quantitative value of the synergistic effect of the two therapeutic agents, because a more extensive *in vitro* evaluation should be performed, which was not the aim of this preliminary study. Nevertheless, an encouraging trend could be observed, because in all the cases as described in the results, a sum effect was observed. The IC50 of imatinib used alone had an IC_{50} of ~64 μM, while the combination of imatinib with ^{177}Lu-cm10 (5 MBq/mL) had a lower IC_{50} value of ~50 μM) and made possible to kill >90% of KB cells when imatinib was 1 μM and radioactivity alone induced ~70% of cell death. Normally this concentration of imatinib induced no cell death (100 % of survival). When we combined G475 with ^{177}Lu-cm10 (5 MBq/mL) the IC_{50} of IGROV-1 was 215 nM, while the inhibitor alone, which was already very potent, had an IC_{50} of 260 nM. Also on KB cells a sum effect was observed: at a concentration of G475 of 100 nM with ^{177}Lu-cm10 (0.10 MBq/mL) >90% of KB cells were dead, when ^{177}Lu-cm10 alone induced 70% of cell death and G475 100 nM alone did not induce any cell death (100% of cells alive).

Cell uptake studies were also carried out to exclude a possible influence in the uptake of the radiofolate from the cells when also the inhibitors were present. Imatinib did not influence the uptake at all, as no significant difference was visible between controls and cells where imatinib (50 or 100 μM) was added. The same was observed for G475 on IGROV-1. This was not true for KB cells which, when the highest concentration of G475 was added (10 μM), had a significantly lower uptake of the radiofolate, 58 and 63% of controls after 1 and 4 hours, respectively (see figure 6.8). This was probably due to the decreased cell activity after the addition of a toxic amount of the compound (IC_{50}

value was in the low micromolar range). Such a high concentration will not be used in further combination studies.

On the ground of these data, further *in vitro* studies will be carried out. In particular, more combination experiments will be carried out to clearly define IC_{50} values; furthermore, a study to understand how the agents cooperate in inducing cell death will be carried out in our laboratory. If further *in vitro* studies will confirm this trend, *in vivo* studies will be carried out. In this context it will be possible to observe not only the intrinsic synergistic effect, but also the extrinsic one [6.22], which is believed to play a crucial role in the radiosensitivity of cells to radiation [6.21].

6.5 Conclusion

In this study two multi-tyrosine kinase inhibitors were tested alone and in combination with a therapeutic radiofolate, ^{177}Lu-cm10, on FR-positive cell lines. The tested compounds were imatinib, a clinically established inhibitor, and a novel compound G475, synthetized at the Department of Pharmaceutical and Pharmacological Sciences at the University of Padova. With cells survival assays (MTT) we could demonstrate that both compounds could induce cell death with different effectiveness and potency, with G475 being the most potent. The combination of the agents had a sum effect in inducing cell death. Further *in vitro* studies will be carried out to confirm these preliminary results and to study the mechanisms on interaction of the agents.

References

[6.1] K. Collins, T. Jacks, N.P. Pavletich, The cell cycle and cancer., Proc. Natl. Acad. Sci. U. S. A. 94 (1997) 2776–2778. doi:10.1073/pnas.94.7.2776.

[6.2] E. Zwick, Receptor tyrosine kinase signalling as a target for cancer intervention strategies, Endocr. Relat. Cancer. 8 (2001) 161–173. doi:10.1677/erc.0.0080161.

[6.3] A.C. Porter, R.R. Vaillancourt, Tyrosine kinase receptor-activated signal transduction pathways which lead to oncogenesis., Oncogene. 17 (1998) 1343–52. doi:10.1038/sj.onc.1202171.

[6.4] D.R. Robinson, Y.-M. Wu, S.-F. Lin, The protein tyrosine kinase family of the human genome, Oncogene. 19 (2000) 5548–5557. doi:10.1038/sj.onc.1203957.

[6.5] J. Schlessinger, Cell Signaling by Receptor Tyrosine Kinases A large group of genes in all eukaryotes encode for, October. 103 (2000) 211–225. doi:10.1016/j.cell.2010.06.011.

[6.6] J. Baselga, J. Arribas, Treating cancer's kinase "addiction," Nat. Med. 10 (2004) 786–787. doi:10.1038/nm0804-786.

[6.7] A. Levitzki, A. Gazit, Tyrosine kinase inhibition: an approach to drug development., Science. 267 (1995) 1782–8. http://www.ncbi.nlm.nih.gov/pubmed/7892601.

[6.8] A. Petrelli, S. Giordano, From single- to multi-target drugs in cancer therapy: when aspecificity becomes an advantage., Curr. Med. Chem. 15 (2008) 422–32. http://www.ncbi.nlm.nih.gov/pubmed/18288997.

[6.9] M.T. Conconi, G. Marzaro, L. Urbani, I. Zanusso, R. Di Liddo, I. Castagliuolo, P. Brun, F. Tonus, A. Ferrarese, A. Guiotto, A. Chilin, Quinazoline-based multi-tyrosine kinase inhibitors: Synthesis, modeling, antitumor and antiangiogenic properties, Eur. J. Med. Chem. 67 (2013) 373–383. doi:10.1016/j.ejmech.2013.06.057.

[6.10] M.R. Gill, N. Falzone, Y. Du, K.A. Vallis, Targeted radionuclide therapy in combined-modality regimens, Lancet Oncol. 18 (2017) e414–e423. doi:10.1016/S1470-2045(17)30379-0.

[6.11] Y. She, F. Lee, J. Chen, A. Haimovitz-Friedman, V.A. Miller, M.G. Kris, V.R. Rusch, F.M. Sirotnak, The Epidermal Growth Factor Receptor Tyrosine Kinase Inhibitor ZD1839 Selectively Potentiates Radiation Response of Human Tumors

in Nude Mice, with a Marked Improvement in Therapeutic Index, Clin. Cancer Res. 9 (2003) 3773–3778. www.ncbi.nlm.nih.gov/pubmed/14506170.

[6.12] P. Bossi, F. Platini, Radiotherapy plus EGFR inhibitors: synergistic modalities, Cancers Head Neck. 2 (2017) 2. doi:10.1186/s41199-016-0020-y.

[6.13] A. Yacoub, R. McKinstry, D. Hinman, T. Chung, P. Dent, M.P. Hagan, Epidermal growth factor and ionizing radiation up-regulate the DNA repair genes XRCC1 and ERCC1 in DU145 and LNCaP prostate carcinoma through MAPK signaling., Radiat. Res. 159 (2003) 439–52. http://www.ncbi.nlm.nih.gov/pubmed/12643788.

[6.14] M. Hagan, A. Yacoub, P. Dent, Ionizing Radiation Causes a Dose-Dependent Release of Transforming Growth Factor α *In vitro* from Irradiated Xenografts and during Palliative Treatment of Hormone-Refractory Prostate Carcinoma Ionizing Radiation Causes a Dose-Dependent Release of Transform, 10 (2004) 5724–5731.

[6.15] M.P. Kelly, S.T. Lee, F.T. Lee, F.E. Smyth, I.D. Davis, M.W. Brechbiel, A.M. Scott, Therapeutic efficacy of ^{177}Lu-CHX-A″-DTPA-hu3SI93 radioimmunotherapy in prostate cancer Is enhanced by EGFR inhibition or docetaxel chemotherapy, Prostate. 69 (2009) 92–104. doi:10.1002/pros.20856.

[6.16] D.J. Zheng, G.H. Yu, J.F. Gao, J.D. Gu, Concomitant EGFR inhibitors combined with radiation for treatment of non-small cell lung carcinoma, Asian Pac J Cancer Prev. 14 (2013) 4485–4494. http://www.ncbi.nlm.nih.gov/pubmed/24083690.

[6.17] H.R. Withers, The Four R's of Radiotherapy, in: 1975: pp. 241–271. doi:10.1016/B978-0-12-035405-4.50012-8.

[6.18] A. Debucquoy, J.-P. Machiels, W.H. McBride, K. Haustermans, Integration of Epidermal Growth Factor Receptor Inhibitors with Preoperative Chemoradiation, Clin. Cancer Res. 16 (2010) 2709–2714. doi:10.1158/1078-0432.CCR-09-1622.

[6.19] M. Holdhoff, K.-A. Kreuzer, C. Appelt, R. Scholz, I.-K. Na, B. Hildebrandt, H. Riess, A. Jordan, C.A. Schmidt, R.A. Van Etten, B. Dörken, P. le Coutre, Imatinib mesylate radiosensitizes human glioblastoma cells through inhibition of platelet-derived growth factor receptor, Blood Cells, Mol. Dis. 34 (2005) 181–185. doi:10.1016/j.bcmd.2004.11.006.

[6.20] S.J. Hattrup, R.H. Cofield, Osteonecrosis of the humeral head: Relationship of disease stage, extent, and cause to natural history, J. Shoulder Elb. Surg. 8 (1999)

559–564. doi:10.1016/S1058-2746(99)90089-7.

[6.21] M.T. Weigel, L. Dahmke, C. Schem, D.O. Bauerschlag, K. Weber, P. Niehoff, M. Bauer, A. Strauss, W. Jonat, N. Maass, C. Mundhenke, *In vitro* effects of imatinib mesylate on radiosensitivity and chemosensitivity of breast cancer cells, BMC Cancer. 10 (2010) 412. doi:10.1186/1471-2407-10-412.

[6.22] J. Karar, A. Maity, Modulating the tumor microenvironment to increase radiation responsiveness, Cancer Biol Ther. 8 (2009) 1994–2001. doi:10.1086/498510.Parasitic.

[6.23] K. Pietras, A. Östman, M. Sjöquist, M. Sjo, O. Arne, E. Buchdunger, R.K. Reed, C. Heldin, K. Rubin, Inhibition of Platelet-derived Growth Factor Receptors Reduces Interstitial Hypertension and Increases Transcapillary Transport in Tumors Inhibition of Platelet-derived Growth Factor Receptors Reduces Interstitial Hypertension and Increases Transcapillary, (2001) 2929–2934.

[6.24] K. Pietras, K. Rubin, T. Sjöblom, K. Pietras, K. Rubin, T. Sjo, E. Buchdunger, M. Sjo, Inhibition of PDGF Receptor Signaling in Tumor Stroma Enhances Antitumor Effect of Chemotherapy Inhibition of PDGF Receptor Signaling in Tumor Stroma Enhances Antitumor Effect of Chemotherapy 1, (2002) 5476–5484.

[6.25] J.S. Lopez, U. Banerji, Combine and conquer: challenges for targeted therapy combinations in early phase trials, Nat. Rev. Clin. Oncol. 14 (2016) 57–66. doi:10.1038/nrclinonc.2016.96.

[6.26] K. Siwowska, S. Haller, F. Bortoli, M. Benešová, V. Groehn, P. Bernhardt, R. Schibli, C. Müller, Preclinical comparison of albumin-binding radiofolates: Impact of linker entities on the *in vitro* and *in vivo* properties, Mol. Pharm. 14 (2017) 523–532. doi:10.1021/acs.molpharmaceut.6b01010.

[6.27] E. Ranza, A. Bertolotti, A. Facoetti, L. Mariotti, F. Pasi, A. Ottolenghi, R. Nano, Influence of imatinib mesylate on radiosensitivity of astrocytoma cells, Anticancer Res. 29 (2009) 4575–4578. doi:29/11/4575 [pii].

[6.28] A. Östman, PDGF receptors-mediators of autocrine tumor growth and regulators of tumor vasculature and stroma, Cytokine Growth Factor Rev. 15 (2004) 275–286. doi:10.1016/j.cytogfr.2004.03.002.

[6.29] J. Yu, C. Ustach, H.-R.C. Kim, Platelet-derived growth factor signaling and human cancer., J. Biochem. Mol. Biol. 36 (2003) 49–59.

http://www.ncbi.nlm.nih.gov/pubmed/12542975.

[6.30] D. George, Platelet-derived growth factor receptors: a therapeutic target in solid tumors., Semin. Oncol. 28 (2001) 27–33. http://www.ncbi.nlm.nih.gov/pubmed/11740804.

[6.31] P. Low, S. Kularatne, Folate-targeted therapeutic and imaging agents for cancer, Curr. Opin. Chem. Biol. 13 (2009) 252–262. doi:10.1016/j.cbpa.2009.03.022.

6.[32] C. Müller, J. Reber, S. Haller, H. Dorrer, P. Bernhardt, K. Zhernosekov, A. Türler, R. Schibli, Direct *in vitro* and *in vivo* comparison of ^{161}Tb and ^{177}Lu using a tumour-targeting folate conjugate, Eur. J. Nucl. Med. Mol. Imaging. 41 (2014) 476–485. doi:10.1007/s00259-013-2563-z.

[6.33] C. Müller, Folate based radiopharmaceuticals for imaging and therapy of cancer and inflammation., Curr. Pharm. Des. 18 (2012) 1058–83. http://www.ncbi.nlm.nih.gov/pubmed/22272825.

[6.34] N. Parker, M.J. Turk, E. Westrick, J.D. Lewis, P.S. Low, C.P. Leamon, Folate receptor expression in carcinomas and normal tissues determined by a quantitative radioligand binding assay, Anal. Biochem. 338 (2005) 284–293. doi:10.1016/j.ab.2004.12.026.

[6.35] K. Siwowska, R. Schmid, S. Cohrs, R. Schibli, C. Müller, Folate Receptor-Positive Gynecological Cancer Cells: *In Vitro* and *In Vivo* Characterization, Pharmaceuticals. 10 (2017) 72. doi:10.3390/ph10030072.

[6.36] P. Zimmermann, M. Hirsch-hoffmann, L. Hennig, W. Gruissem, GENEVESTIGATOR . Arabidopsis Microarray Database and Analysis Toolbox 1 [w], 136 (2004) 2621–2632. doi:10.1104/pp.104.046367.1.

[6.37] C.-H. Yeong, M. Cheng, K.-H. Ng, Therapeutic radionuclides in nuclear medicine: current and future prospects., J. Zhejiang Univ. Sci. B. 15 (2014) 845–63. doi:10.1631/jzus.B1400131.

Conclusions

In the first part of this thesis project a new method for the production of carrier-free radionuclides was studied in order to make the production of radionuclides for medical use possible at the ISOL facility under construction at LNL-INFN.

Secondary targets for the ion beams deposition were produced. Two target materials were chosen, sodium chloride and activated carbon. The materials were transformed into solid discs thanks to powder compression, with the help of the binder PVA in the case of activated carbon and without any additive for sodium chloride. The discs were characterized and proved to have good mechanical and superficial properties. These substrates could be used for the deposition of stable accelerated yttrium, copper and iodine. The test-bench of the SPES project, named Front End (FE), was used for the production of stable beams. All three elements under test, yttrium, iodine and copper, could be ionized, collected on the secondary targets, and detected after dissolution, even if with difficult repeatability caused by instability of the FE. These results however represent a very positive starting point for the validation of the "ISOL" part of the ISOLPHARM project, making available secondary targets in which desired isotopes are collected.

In chapter 4 the chemical purification process for yttrium and strontium, developed to get rid of isobaric contaminants, was described. NaTi, an inorganic material could be synthetized and three types of NaTis were produced, depending on the temperatures of synthesis (100, 150 and 175 °C). The resin was tested using the cold elements, for this reason analytical methods for strontium (GF-AAS) and for yttrium (UV-Vis) were developed. The affinity of NaTi for strontium was very high at basic pH, but also yttrium was retained in the resin. Yttrium could be recovered from NaTi only at acidic pH (<4), when also strontium was released. For this reason, the separation of the two ions turned out to be more challenging. An evaluation of the behavior of the two ions in the pH range from 0 to 4 made it possible to find a condition where the two ions behaved differently (pH 2). Its use for the purification of ^{89}Sr from the stable contaminant ^{89}Y, considering the very low amount of ^{89}Y in the solution, was satisfactory with a reduction of >60% of the initial amount. NaTi as a resin for a ^{90}Sr/^{90}Y generator was also studied and a process developed. In the hypothesized system

it will be possible to elute pure ^{90}Y after ^{90}Sr decay. The weak point of the system is the loss of ^{90}Sr in the loading process that needs to be optimized.

In the second part of this thesis, two different strategies to improve TRT were studied: firstly, a set of serum protein binders were radiolabeled and characterized *in vitro* and *in vivo*, secondly a preliminary study for the combination therapy of TKIs with TRT was carried out.

The evaluation of three plasma protein-binding radioligand was described in chapter 5. It was demonstrated that PPB-01 had extraordinary binding properties to HSA while PPB-02, where a halogen was replaced by an ethynyl entity, had reduced plasma proteins binding affinity. The third entity PPB-03 was found to bind with high affinity to hTTR and has a very promising pharmacokinetic properties. Future studies in PD Dr. Cristina Müller's laboratory will be focused on the application of these binding entities in combination with clinically relevant targeting agents for diagnostic and therapeutic purposes in nuclear medicine.

Finally, two multi-tyrosine kinase inhibitors were tested alone and in combination with a therapeutic radiofolate, ^{177}Lu-cm10, on FR-positive cell lines. The compounds chosen for the project were imatinib, a clinically established inhibitor, and a novel compound G475, synthetized at the Department of Pharmaceutical and Pharmacological Sciences at the University of Padova. MTT assays proved that both compounds could induce cell death with different effectiveness and potency, with G475 being the most potent. The combination of the agents with ^{177}Lu-cm10 had a sum effect in inducing cell death. Further *in vitro* studies will be carried out to confirm these preliminary results and to study the mechanisms of interaction of the agents.